DISS. ETH NO. 23793

Assistive Robots for Minimally Invasive Ophthalmic Surgery

A dissertation submitted to

ETH ZURICH

for the degree of

Doctor of Sciences of ETH Zurich

(Dr. sc. ETH Zurich)

presented by

Franziska Ullrich

M.Sc. in Robotics, Systems and Control, ETH Zurich

born on March 7, 1987
Citizen of Germany

accepted on the recommendation of

Prof. Bradley J. Nelson, examiner,
Prof. Stephan Michels, co-examiner,
Prof. Christos Bergeles, co-examiner

2016

Keep your eyes on the stars,
and your feet on the ground.

Theodore Roosevelt

Acknowledgements

This dissertation cumulates the work and results of four years of doctoral studies at the Multi-Scale Robotics Laboratory (MSRL) at ETH Zurich. During this time I had the chance to deepen my knowledge in the field of robotics, but also became knowledgable in the medical field of ophthalmology. Many friends and colleagues showed great support and guidance during this time, without whom this work would not have been possible.

Foremost, I would like to express my sincere gratitude to my supervisor Prof. Bradley J. Nelson for giving me the chance to work and learn in his lab. Brad, thank you for many inspiring discussions, for motivating and challenging me. Your enthusiasm, creativity, patience, and guidance supported me in my research projects, but also encouraged me to grow my personality.

Special thanks go to Dr. Roel S. Pieters and Dr. Andrew J. Petruska for their friendship and their guidance and supervision throughout several projects. Roel, thanks for the many interesting and jovial discussions about computer vision and control in your office. Andrew, your thorough theoretical understanding and detailed explanations inspired me to continuously revise and extent my knowledge. Thank also goes to Prof. Christos Bergeles, whose doctoral work inspired me greatly and whose ideas and comments concerning my own work are greatly appreciated. I would like to express my gratitude to Prof. Stephan Michels and Prof. Matthias Becker from the Triemli Hospital Zurich, as well as Dr. Avraham Dishy from the Cantonal Hospital Aarau for advice and ideas in the field of ophthalmology. Special thank goes to Prof. Stephan Michels for his medical expertise as one my doctoral thesis co-supervisors. Much appreciation goes to Brigitte Geissmann and Kerstin Degen for cheerfully steering me through bureaucratic or personal matters. I would like to extent my gratitude to Erdem Siringil, who helped out with his expertise when I needed equipment and tools.

Many thanks go to the friends and colleagues at the MSRL for fruitful and energising discussions at the office, during lunch, or with a cup of coffee. Especially, I would like to thank Dr. Sandro Erni, Taylor Newton, Jan Burri, Erdem Siringil, Dr. Roel Pieters, Dr. Andrew Petruska, Samuel Charreyron, Dr. Simone Schürle, Dr. Dimitrios Felekis, Dr. Stefano Fusco, Dr. Famin Qiu, and Dr. Kathrin Peyer. These special friends have continuously guided and supported me during my research but also my personal life from the beginning to the end of my doctoral studies. My gratitude is extended to Dr. Salvador Pané, Dr. Famin Qiu, Marcus Hoop, and Hen-Wei Huang for fabrication and many interesting insights concerning materials. This work would not have been possible without the work of many Bachelor and Master students. Of the many motivated students, I would like to especially acknowledge Jonas Lussi, Kanika Dheman, Daniel Lehmann, Sean Lyttle, Tonci Novkovic, Christoph Ryan and Vasileios Chatzopoulos. Special thanks go to Dr. Dimitrios Felekis, Dr. Kathrin Peyer, Naveen Shamsudhin, Hen-Wei Huang, and Burak Zeydan for their support during teaching the *Introduction to Robotics and Mechatronics* course. Promoting our research to a non-academic audience was a pleasure I shared with Dr. Sandro Erni, Dr. Kathrin Peyer, and Jan Burri. My extended gratitude goes to Peter Guy for proof-reading and questioning many written pages about this work and for being a joyful and good friend.

Finally, but not least, I want to express my deepest gratitude to my family for their everlasting encouragement, emotional support, and love. Vati, thank you for teaching me about the world we live in and motivating me to stay curious. Mama, thank you for being a strong and independent role model. Katja, thanks for being a wonderful, understanding, and ever supporting sister. Magret, thank you for being a great and thoughtful friend. Omi, thank you for your big heart and for listening to all my stories. Opa, thanks for inspiring me to appreciate technology and become an engineer. Thanks also goes to my friends outside the lab, who have supported me during many exciting times. Huge thanks, love, and appreciation go to Christian Mathis who laughs with me when I am joyful and holds me up when I am worried. Knödi, your strong beliefs in me, your wise words, and your cheerful nature are invaluable to me.

Abstract

Age-related visual loss and ageing demographics account for a large impact on societal health costs on a global scale. Efficient ophthalmic surgeries must be precise, safe, and fast and thus, require the surgeon to be highly dexterous and experienced as the small forces applied to the delicate structures in the eye lie below the human force perception limit. To overcome these limitations current research focuses on robotic systems to assist in minimally invasive surgery due to their high precision, stability, and dexterity. Moreover, drug delivery to the posterior segment of the eye presents further challenges and limitations due to the quick systemic absorption of drugs. Thus, drug delivery to the posterior eye requires high dosages of medication, which is commonly delivered intravenously or by intravitreal administration.

This thesis explores several robot-assisted systems for minimally invasive ophthalmic surgery. It focuses on the development of several untethered and tethered systems that can provide treatment for ocular diseases, such as cataract, age-related macular degeneration, or vitreous floaters. The treatment methods can be divided into two categories, which consist of drug delivery applications and mechanical surgical interventions inside the eye. Furthermore, the presented robotic devices are either designed for treatment in the anterior or the posterior eye segment, and thus, require different design and actuation specifications. The first robotic platform consists of magnetically guided intravitreal microrobots of different shapes for targeted drug delivery or manipulation of vitreous floaters. The second system combines magnetic and mechanical actuation to control a flexible catheter with a customised diathermy tool for capsulorhexis, an essential step in cataract surgery. A robotic system is demonstrated that pivots around a single point for manipulation of tools inside the eye with minimum shear forces applied to the sclera during surgery. The fourth robotic system automatically injects medication into the vitreous of the eye for the

safe and efficient treatment of age-related macular degeneration. The systems presented in this thesis combine the advantages and safety of minimally invasive robotic surgery with the precision of magnetically guided surgical tools for ophthalmic surgery. All of the systems can be remotely controlled and monitored by a physician, while overcoming spatial constraints and facilitating physician-patient interaction during surgery.

Zusammenfassung

Die finanzielle Belastung des Gesundheitssystems durch Sehschwächen und Sehbehinderungen sind groß. Ophthalmologische Eingriffe müssen möglichst schnell, mit hoher Sicherheit und Präzision erfolgen. Da die bei Operationen am Auge wirksamen Kräfte oft kleiner als das menschliche Wahrnehmungslimit sind, muss der Chirurg viel Erfahrung und Fingerfertigkeit mitbringen. Mit Hilfe robotischer Hilfstechnologien können mögliche Probleme vermindert beziehungsweise sogar verhindert werden und erlauben es, sichere und hochpräzise Operationen durchzuführen. Weiterhin wird die Wirkstoffabgabe aufgrund der rapiden systemischen Absorption von Arzneimitteln erschwert. Daher erfordert die Medikamentenabgabe im hinteren Augensegment eine hohe Wirkstoffdosis, welche allgemein intravenös oder intravitreal verabreicht wird.

Das Ziel dieser Dissertation ist es, verschiedene robotische Systeme für die minimal invasive Augenchirurgie zu erkunden, und konzentriert sich auf die Entwicklung von medizinischen Robotern zur Behandlung von Augenkrankheiten, wie zum Beispiel Katarakt, altersbedingter Makuladegeneration oder Floater im Glaskörper. Die Behandlungsverfahren können in zwei Kategorien unterteilt werden, die der Arzneimittelabgabe und mechanische Eingriffe im Augeninneren. Weiterhin werden die hier vorgestellten Systeme entweder für die Behandlung in der vorderen oder der hinteren Augenkammer entwickelt und erfordern daher unterschiedliche Spezifikationen. Die erste vorgestellte Roboterplattform besteht aus magnetisch gesteuerten kabellosen Mikrorobotern zur gezielten Wirkstoffabgabe im Inneren des Auges und zur Manipulation von Floatern. Zur automatisierten Kapsulorhexis, einem essentiellen Schritt der Kataraktchirurgie, wurde ein magnetisch-mechanisch angetriebenes System mit flexiblem Körper und magnetischer Spitze entwickelt. Ein anderes Robotersystem rotiert um einen einzigen Punkt, um Werkzeuge im Auge zu bewegen und gleichzeitig die Scherkräfte, die auf die Lederhaut des Auges wirken, auf

ein Minimum reduziert. Das vierte hier vorgestellte System wurde zur automatisierten intravitrealen Injektion von Medikamenten entwickelt, um die Behandlung von altersbedingter Makuladegeneration effizient und sicher zu gestalten. Alle in dieser Dissertation vorgestellten Systeme vereinen die Vorteile und Sicherheit von minimal invasiven robotergestützten Operationen mit der Genauigkeit magnetisch gesteuerter Werkzeuge. Die dargestellten Roboter erlauben es, ophthalmische Operationen aus der Distanz fernzusteuern und zu überwachen.

Contents

List of Tables

List of Figures

Chapter 1

Introduction

Present-day surgical interventions can be broadly categorised into invasive, minimally invasive and non-invasive procedures dependent on the level of induced patient trauma. During invasive surgery typically skin and tissue are cut to allow the surgeon direct and full access to treat an organ. On the other extreme, non-invasive procedures are mainly diagnostic methods, which do not involve incisions into the patient's body. These methods allow the physician to examine the body externally and include radiology methods, such as Magnetic Resonance Imaging (MRI), Computer Tomography (CT), ultrasound, or X-ray radiography. Minimally invasive surgery lies between these types of surgery [1].

1.1 Medical Robotics

In contrast to open surgery, minimally invasive surgery has become the preferred method of surgery due to its many benefits for the patient. Smaller incision or instrument guidance through natural orifices can greatly reduce patient trauma and decrease recovery times leading to reduced health care costs [2]. Factors that increase the cost for a surgical intervention, such as post-surgical complications and scarring, can be reduced by minimally invasive methods. However, the nature of minimally invasive surgery utilising rigid tools inside small orifices can lead to ergonomically challenging manipulation of instruments and limit the surgeon's dexterity. To overcome these challenges, many surgical robots and assistive devices have been suggested. Medical robots are not simply machines, but are intelligent, interacting devices to support the surgeon during medical interventions. Robotic surgery allows the collection of qualitative information through sensors and provides feedback to the human

operator. The robotic device provides high stability and accuracy, and is thus ideal during repetitive or high precision surgical tasks. Many assistive systems are remotely controlled by a human surgeon and can be located in small or hazardous environments, *i.e.* inside an MRI scanner or while the patient is under X-ray examination. The advantages of robot-assisted surgery are summarised in the following:

- high accuracy and stability of operation

- potentially faster

- cheaper for high throughput surgery

- usable in narrow spaces or hazardous environments (*e.g.* MRI, X-ray)

- quantitative information through sensor feedback

- potentially remotely controlled

1.2 Goal of this Thesis

This thesis aims to explore several robot-assisted systems for minimally invasive ophthalmic surgery. As illustrated in Fig. 1.1, this work focuses on the development of several untethered and tethered systems that can provide treatment for ocular diseases, such as cataract, age-related macular degeneration, or vitreous floaters. The treatment methods can be divided into two categories, which consist of drug delivery applications and mechanical surgical interventions inside the eye. Furthermore, robotic devices are either designed for treatment in the anterior or the posterior eye segment, and thus, require different design and actuation specifications. The systems presented in this thesis combine the advantages of minimally invasive robotic surgery with the precision of magnetically guided surgical tools and the safety of minimally invasive devices for ophthalmic surgery. All of the presented systems can be remotely controlled and monitored by a physician, overcoming spatial constraints and facilitating physician-patient interaction during surgery.

	Anterior Eye	**Posterior Eye**
Untethered Robot		• Intravitreal Microrobot • Floater Removal
Tethered Robot	• Automated System for Capsulorhexis	• Remote Center of Rotation System • Automated Intravitreal Injection
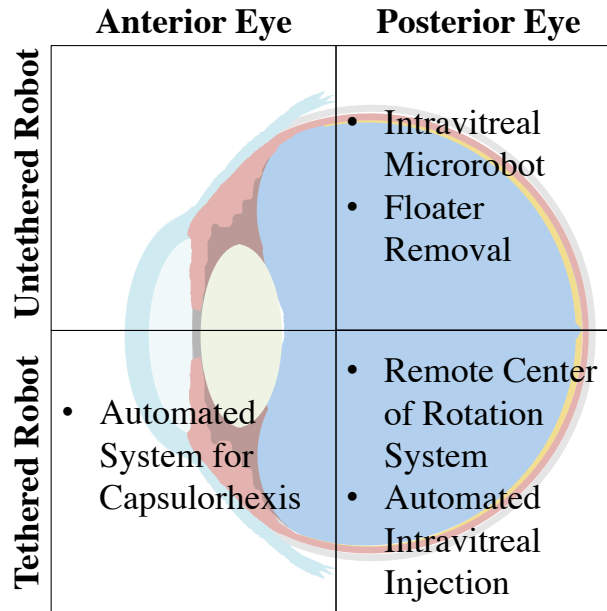
Figure 1.1: The individual projects embedded in this thesis aim to provide solutions for the treatment of diseases in the anterior and the posterior eye segment with untethered and tethered robots.

The first application utilises a wireless magnetically guided microrobot in the posterior eye for targeted drug delivery to the retina. A similar wireless device allows for mechanical ophthalmic applications, such as the removal of vitreous floaters.

A second application combines a tethered flexible tool for capsulorhexis in the anterior eye, for the surgical treatment of cataracts. A hybrid mechanic-magnetic actuation system is presented. Design specifications for the system are identified by mechanically characterising the required force to perforate the lens capsule using a micro-mechanical characterisation method.

A remote center of rotation system allows for precise positioning and orientating of a tethered tool for drug delivery and surgical interventions at the retina.

A tethered automated system is developed to provide direct drug delivery into the vitreous in the posterior eye segment through precise intravitreal in-

jections for the treatment of age-related macular degeneration or other chronic ocular diseases.

The focus of this thesis is on the development and evaluation of several tethered and untethered robotic systems for drug delivery and surgical interventions in the anterior or posterior eye segment. Utilising magnetic control of devices allows for actuating the tool tip rather than the end of the tool, resulting in increased dexterity and precision of an intervention.

1.3 Structure of the Thesis

Chapter 2 outlines the anatomy of the human eye and describes common ocular impairments. Additionally, several robotic devices for ophthalmic surgery are presented followed by an introduction to drug delivery to the eye. The theoretical background for magnetic manipulation of magnetised objects utilising an electromagnetic coil setup is outlined in Chapter 3.2. The benefits of magnetically manipulated minimally invasive tools during ophthalmic surgery are also outlined in this chapter. The following chapters outline the development of robotic systems for specific ophthalmic applications.

Chapter 4 presents the manipulability of magnetically guided wireless microrobots through *ex vivo* and *in vivo* experiments in porcine and lapine eyes. Floater removal in the vitreous humour is explored as a mechanical application of wireless intravitreal microrobots. The following chapters demonstrate the development of magnetically guided catheter systems for the anterior and the posterior eye segment. Chapter 5 outlines the development of an automated system for capsulorhexis utilising a magnetically guided flexible tool. The development of a remote center of rotation system for intraocular surgery that can be used in combination with an electromagnetic guidance system is presented in Chapter 6. Chapter 7 illustrates the development of an automated system for intravitreal injections for the efficient treatment of age-related macular degeneration. This thesis closes with a summary and conclusions in Chapter 8. The structure and flow of information in this thesis is illustrated in Fig. 1.2.

Chapter 2: Treatment of Ophthalmic Impairments

Chapter 3: Magnetic Manipulation for Minimally Invasive Surgery

Chapter 4: Untethered Microrobots for Ophthalmic Applications

Chapter 5 & 6: Tethered Robots for Ophthalmic Applications

Chapter 7: Automated Intravitreal Injection Robot

Chapter 8: Summary, Contributions, Conclusions
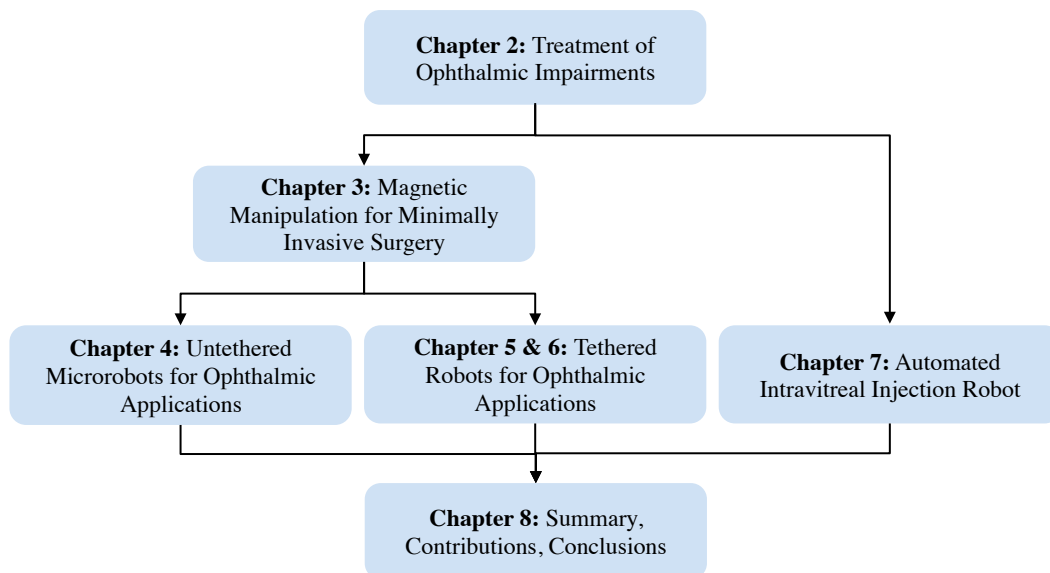
Figure 1.2: The structure and the flow of information of this thesis.

Chapter 2

Treatment of Ophthalmic Impairment

2.1 Anatomy of the Human Eye

The human eye is a multilayered organ that is highly protected from the outer environment on the anterior part and allows for controlled blood and solute exchange at the posterior side through the highly vascularised choroidal layer at the back of the eye, as illustrated in Fig. 2.1.
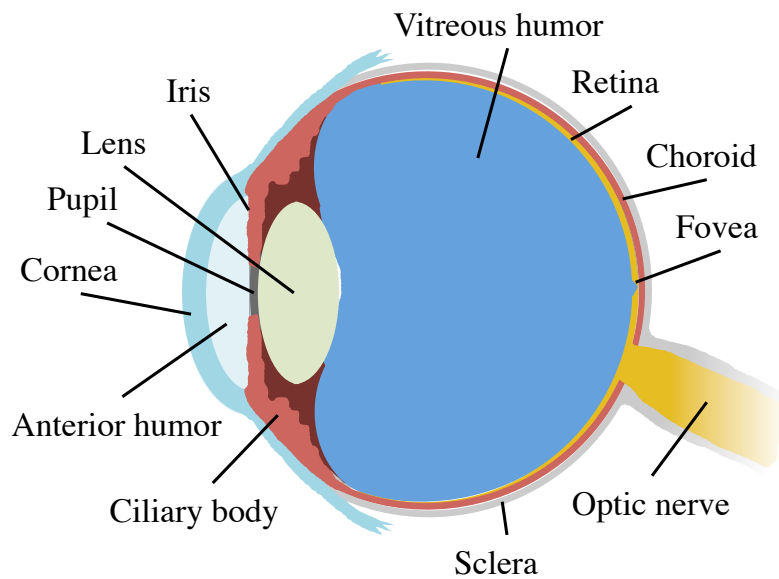
Figure 2.1: The anatomy of the human eye.

2.1.1 Cornea and Sclera

The human eye is protected by a dense, white, opaque, fibrous, connective tissue, called the sclera. It provides structural integrity for the globe and protects the eye's internal structures from physical injury [3]. The sclera is approximately spherical with a radius of curvature of about 12 mm [4]. This layer extends to the clear cornea at the front of the eye which covers one sixth of the total surface area of the eye globe [3]. This multilayer is transparent, avascular, and relatively dehydrated tissue. The cornea has an approximate radius of curvature of 8 mm [4] and forms the anterior chamber of the eye. The anterior chamber is filled with aqueous humour, a watery liquid. The outer layer that covers the sclera and episclera, called conjunctiva, is a thin mucous and highly vascularised membrane and forms a physical barrier to dirt or microbes.

2.1.2 Crystalline Lens and Iris

The biconvex crystalline lens is connected to the ciliary body by suspensory ligaments, called zonules, and can change its refractive power when the ciliary muscles contract, a process called accommodation. This process enables the eye to focus on objects at various distances. The lens consists of highly aligned collagen and is located behind the anterior chamber of the eye. The iris consists of muscles and thin connective tissue that extends from the ciliary body and is located anterior to the crystalline lens. Light is bundled and focused by the cornea and the lens, while the iris acts as an aperture to regulate the amount of light entering the eye. The crystalline lens is encapsulated by the lens capsule, a thin viscoelastic membrane. In human eyes the thickness of the anterior lens capsule increases with age [5]. It features a central thickness of approximately $25 - 30\,\mu m$ while the posterior lens capsule is $2 - 4\,\mu m$ thick [6] as illustrated in Fig. 2.2. The lens fibre cells are derived from the lens epithelial cells, which continue to divide and form new lens fibres throughout one's lifetime. This process may cause an ocular disease, called cataract, as described in Section 2.2.1.
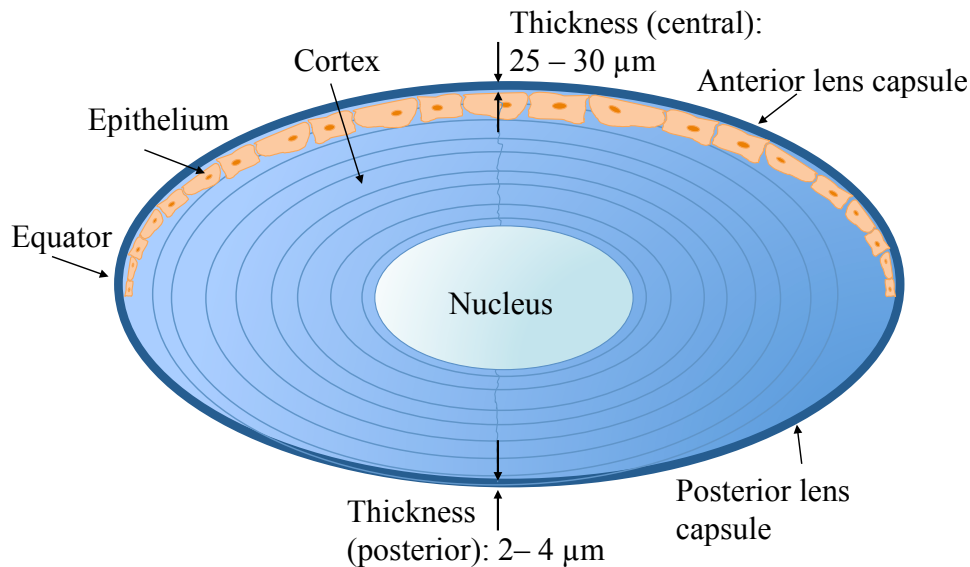
Figure 2.2: The crystalline lens consists of the lens capsule surrounding the lens cortex and nucleus. A layer of epithelial cells covers the anterior lens capsule. The lens capsule has a central thickness of $25 - 30\,\mu\text{m}$ anteriorly and $2 - 4\,\mu\text{m}$ posteriorly [6].

2.1.3   Vitreous Humor

The largest structure in the posterior eye chamber is the vitreous humour, a transparent and gelatinous body. It is located between the lens and the retina. The vitreous humour has a volume of approximately $4\,\text{mL}$ and is composed of 98% water and a fibrous network of collagen and hyaluronic acid [7], as illustrated in Fig. 2.3. The types of collagens found in the vitreous humour are mainly types II, V/XI, and IX [8]. With age, the vitreous humour changes its structure due to aggregation of collagen fibres [8], leading to liquefaction of the vitreous. Sebag [9] examined the rate of liquefaction of the human vitreous in relation to a patient's age. The results are summarised in Fig. 2.4. The role of the vitreous is not fully understood, but recent research suggests that it may play a role in the storage of nutrients [10] and exhibits more importance than previously assumed.
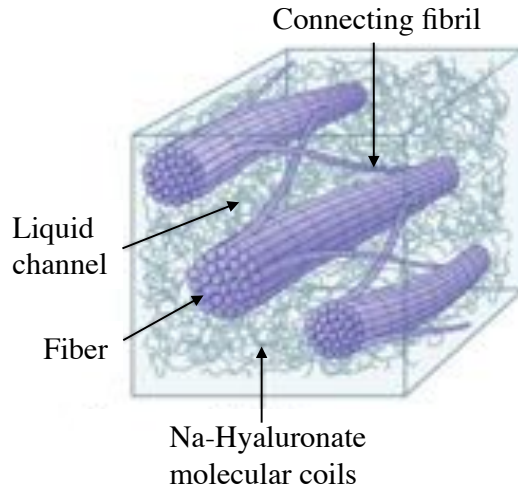
Figure 2.3: The ultrastructure of the vitreous humour, depicting the dissociation of hyaluronic acid molecules and collagen fibrils. Adapted from [3].
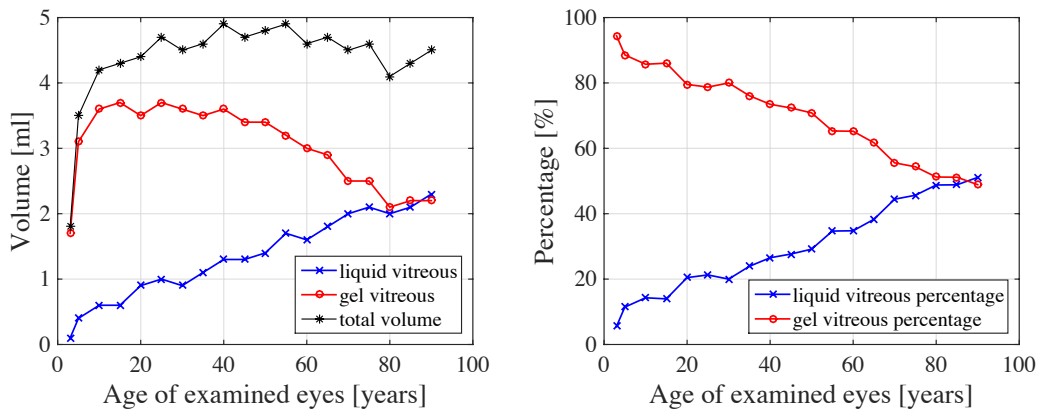
Figure 2.4: Liquefaction of the human vitreous humour as studied by Sebag [9].

2.1.4   Retina and Choroid

The retina is a light-sensitive tissue at the back of the eye, which is an extension of the central nervous system and is connected to the brain via the optic nerve [4]. The retina consists of photoreceptor cells (rod and cone cells), that in conjunction with other cells receive, pre-process and transmit light sig-

nals into the brain through the optic nerve. The cells allow for conscious light perception and vision including color differentiation, perception of depth, and motion. Oxygen is supplied to the inner retina by retinal vessels, while the outer retina is supplied by the choroidal layer. The choroid is a highly vascularised layer that extends from the posterior eye chamber to the ciliary body. It is responsible for oxygen supply, temperature control, and maintaining the eye's intraocular pressure.

2.2 Ocular Impairment and Treatment Strategies

In middle-income and industrialised countries four prevalent eye diseases have emerged that may severely reduce visual acuity or lead to total blindness of patients. The majority of world blindness is caused by cataract, a loss of transparency of the lens. The leading cause of visual deficiency in industrialised countries is age-related macular degeneration. This disease ranks third among global causes of visual impairment [11]. The list of priority eye diseases is completed with diabetic retinopathy, a disease caused by diabetes mellitus, and glaucoma, which is characterised by a damaged optic nerve. Figure 2.5 illustrates an image seen by a healthy person and the perceived image by a patient suffering from the aforementioned eye diseases.

2.2.1 Cataract

Cataracts account for 51% of world visual disability [11] and are often associated and increasing with age. In 2010, 17.11% of the U.S. population aged 40 years and older were affected by cataract [12]. A cataract is characterised by the gradual opacification of the crystalline lens that normally focuses incoming light rays on the retina. Normally, the lens fiber cells are highly aligned with their neighbouring cells. Disruption of this precise organisation of cells, or the aggregation or denaturation of proteins within them, as well as the accumulation of metabolic waste products, can destroy the lens' transparency and cause cataract [3]. During cataract surgery a corneal incision is made at the limbus to allow for insertion of a sharp pointed instrument (a capsulorhexis needle or

© National Eye Institute

       (d)   (e)

Figure 2.5: (a) Image perceived by a health person and the same image perceived by a patient suffering from (b) cataract, (c) age-related macular degeneration, (d) diabetic retinopathy, and (e) glaucoma (©National Eye Institute).

cystotome) into the aqueous anterior chamber of the eye. The instrument is placed over the center of the anterior capsule and pushed posteriorly to perforate the lens capsule [13]. After the anterior chamber has been filled with a viscous gel for anterior chamber stability, this procedure is followed by the opening of the lens capsule, and the removal of the cortex, nucleus and epinucleus, typically by phacoemulsication, irrigation, and aspiration. Subsequently, an artificial intraocular lens is inserted into the capsular bag.

2.2.2   Age-related Macular Degeneration

Neovascular age-related macular degeneration (AMD) is the primary cause of blindness in industrialised countries with a blindness prevalence of 8.7% [11]. This disease is characterised by uncontrolled vascularisation and degenerative lesions in the retina and causes loss of central vision. Since the approval of the first intravitreally applied drugs for the treatment of AMD [14, 15], intravitreal injection has become one of the most frequently performed surgical procedures in ophthalmology with more than 4 million injections worldwide in 2014. The demand for intravitreal therapy evolved dramatically over the past decade and is expected to increase further in the future [16]. Thus, the need for various intravitreally administered drugs, including vascular-endothelial-growth-factor (VEGF) inhibitors, is expected to increase, potentially raising health care costs.

2.2.3   Diabetic Retinopathy

Similar to AMD, diabetic retinopathy (DR) causes lesions in the retina due to vascular changes in the retinal circulation and can result in blindness. More than 75% of patients suffering from diabetes mellitus for more than 20 years are affected by some form of DR. It has been estimated that DR accounted for about 5% of world blindness in 2002 [11]. Due to increasing trend of diabetes prevalence throughout the world, more individuals are expected to suffer from diabetic retinopathy in the future. DR can be controlled by optimising glycaemic control and controlling for other cardiovascular risk factors including hyperlipidaemia and hypertension. DR may be treated with intraocular

injections or, in its later stage, by laser photocoagulation of the retina.

2.2.4   Glaucoma

Glaucoma is a group of diseases that is characterised as a progressive optic neuropathy, often due to raised intraocular pressure, resulting in damaging of the optic nerve, often due to increased intraocular eye pressure. The World Health Organisation estimates the number of blind people as a result of primary glaucoma to be 4.5 million worldwide [11]. Effective medical and surgical treatment is available to maintain sight if the disease is diagnosed in an early stage. The challenge is to effectively monitor a patient's eye pressure.

2.3   Robotic Systems for Ophthalmic Surgery

Efficient ophthalmic surgeries must be precise, safe, and fast and, thus, require the surgeon to be highly dexterous and experienced as the small forces applied to the structures in the eye are lower than the human force perception limit [17, 18]. To overcome these limitations various robotic platforms have been proposed as assistive tools for ophthalmic surgery. The first robot-assisted tele-operation (Lindbergh Operation) was performed by a surgical team located in New York, who performed a cholecystectomy on a patient in Strasbourg/France in 2001 [19]. As virtually all patient evaluation depends on optical and imaging devices, ophthalmology is well-suited for telemedicine applications [20].

2.3.1   Surgeon Extenders

Surgeon extenders are systems for robot-assisted surgery that are usually directly controlled by a human operator. These systems sense the haptic input from a surgeon and provide tremor-free, smooth motion on a pre-defined path of the surgical tool tip. Surgeon extenders are used similarly to conventional tools for ophthalmic surgery but allow for high precision.

A first-generation surgical robot was introduced at John Hopkins University in 1999 [21], the *Steady Hand Robot*. The second-generation platform was
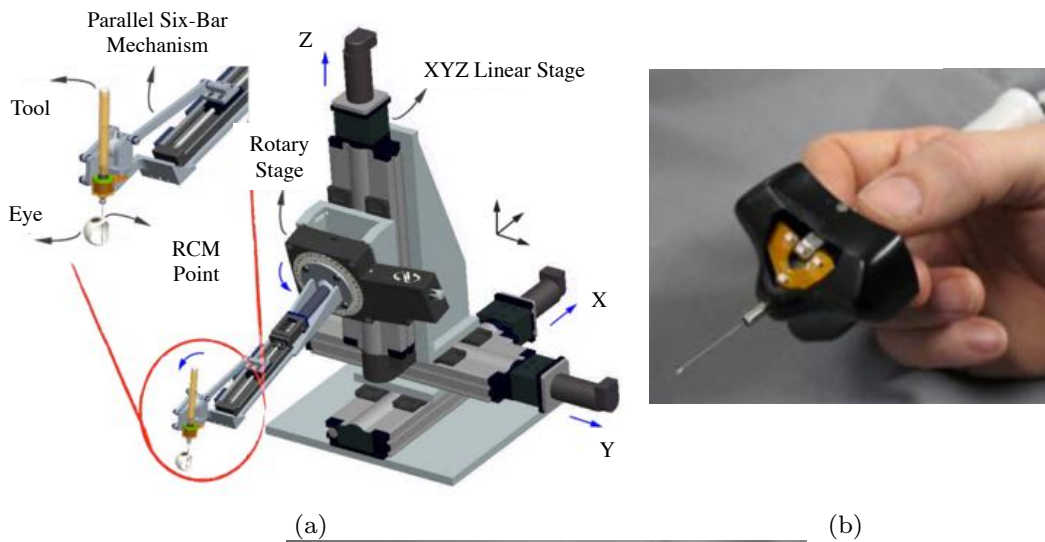
Figure 2.6: (a) The second-generation steady-hand robot, developed at John Hopkins University and (b) the handheld micromanipulator Micron, developed at Carnegie Mellon. Images taken from [26] and [22], respectively.

developed in 2010 [22] and is illustrated in Fig. 2.6(a). The system is directly controlled by the surgeon and senses the surgical forces during an ophthalmic intervention. This information is used to provide precise, tremor-free position control of a tool and force scaling. Preliminary experiments demonstrated the feasibility of stable robotic augmentation and force scaling of a surgeon's tactile input [23]. The system's precision was demonstrated through successful cannulation of veins on the chorioallantoic membrane of a chicken embryo with diameter of $80\,\mu m$ [24].

The micromanipulator *Micron* is a hand-held system that actively cancels the surgeon's hand tremor based on low-pass filtering and motion scaling [25, 26], shown in Fig. 2.6(b). The tip of the tool is actuated to counteract any involuntary hand motion of the surgeon. The system has been coupled with different assistive modes, such as snap-to-vein behaviour, by utilizing visual servo techniques [27]. Patterned photocoagulation has been demonstrated in a simulated scenario with the system [28].
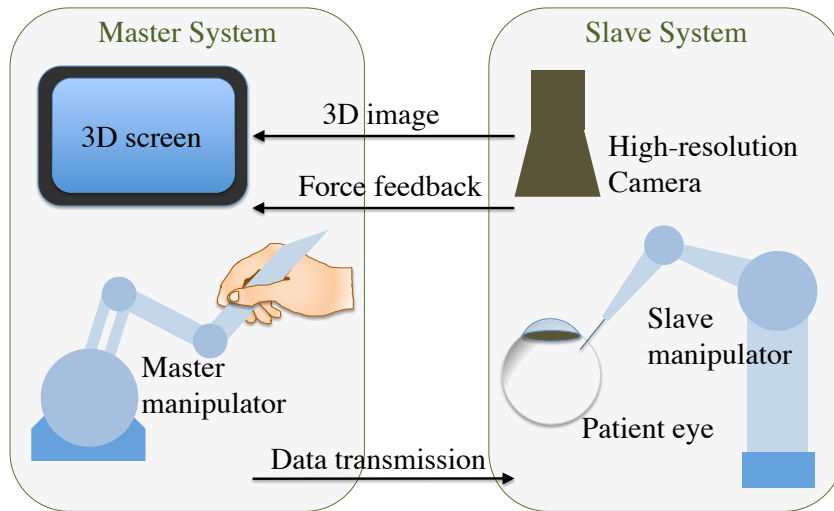
Figure 2.7: Overview of a typical master-slave robotic system for assistance in teleoperated ophthalmic surgery.

2.3.2   Master-Slave Systems

Most systems developed for teleophthalmology are so-called master-slave systems, consisting of a master manipulator and a slave robot. The remote ophthalmic surgeon guides the master manipulator with his trained hands, and control data are transmitted to the slave manipulator, which executes the surgery on the patient's eye by controlling the robot's end-effector accordingly. A high-definition camera detects the position of the tool inside the eye and images are transmitted back to the surgeon on a 3D-screen, as illustrated in Figure 2.7.

Several master-slave systems have been suggested for robot-assisted ophthalmic telesurgery. The da Vinci system [29, 30] (Intuitive Surgical, Sunnyvale, CA, US) has been used to close a full thickness corneal and scleral laceration on a porcine eye, but for intraocular surgery the system was unable to create a self-sealing wound in the sclera [30].

A robotic concept for ophthalmic microsurgery has been developed at Vanderbilt University that is driven by a haptic master device that tracks and transmits the surgeon's hand movement [31–34], as illustrated in Fig. 2.8(a).

The researchers reported that performance of the robot-assisted procedure was tested by peeling a membrane in an eye model and compared to traditional manual surgery by the same surgeon. The teleoperation of the robotic assistive device was easy to learn and took only one practice session without instruction. Results indicated that robotic assistance improved the success rate of the membrane peeling task by more than two times [34].

A parallel prototype robot for vitreoretinal surgery with high positioning accuracy and micrometer resolution has been developed at Tokyo University [35] and is shown in Fig. 2.8(b). The robot is designed to have a stable remote center of motion and is controlled by an operator, who sees the patient's eye through a high-definition 3D visualiser and moves it with a custom-made master manipulator [36]. The assistive device facilitates intuitive manipulation with motion scaling and tremor cancelling in real-time. The system was tested in an animal model and demonstrated improved accuracy compared to the manual procedure [37]. The parallel slave manipulator includes a mechanism that allows a local assistant to quickly switch the surgical instrument during the procedure [38].

Another robotic surgical platform based on a master-slave manipulator design for intraocular surgery has been developed at UCLA [39]. It is controlled through a master device with two shafts that are manipulated by the surgeon with both hands as if they were standard surgical instruments. The motion of the shafts is measured and transmitted to the slave manipulator during surgery. The system has been used to show the construction of a continuous capsulorhexis and lens cortex removal in an animal model.

In all aforementioned systems the ophthalmic surgeon is still responsible for decision-making and instrument guiding. The main attributes of these systems are summarised in the following.

- A tool is passed through the sclera, increasing shear forces at the point of incision. Manipulability and dexterity are reduced by this scleral interaction.
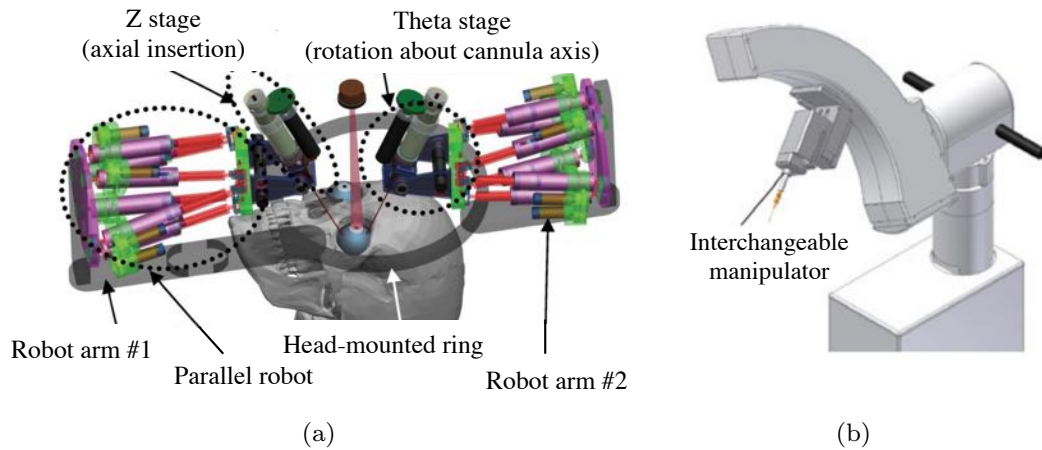
Figure 2.8: (a) The master-slave robot-assisted system developed at Vanderbilt University and (b) the parallel system for vitreoretinal surgery, developed at Tokyo University. Images taken from [31] and [38], respectively.

- Using these systems for ocular surgery still requires vitrectomy to allow movement of a tool without causing traction at the retina.

- All of the aforementioned systems enable position control of the tool but do not allow for direct force control. Thus, the delicate structures in the eye are at risk from a tool that is capable of inducing damage in the event of system failure or patient movement.

- The invasiveness of the robot assisted procedure is not necessarily reduced as the tools are of approximately the same size as those used in manual surgery.

2.4   Drug Administration to the Eye

The corneal and conjunctival epithelium forms a thick physical barrier that protects the eye from external threats and maintains homeostasis. This barrier must be penetrated if drugs are administered topically to the eye. Studies have shown that eye drops are rapidly lost from the ocular surface due to lachrymation and tear turnover [40], and typically less than 5% of topically applied
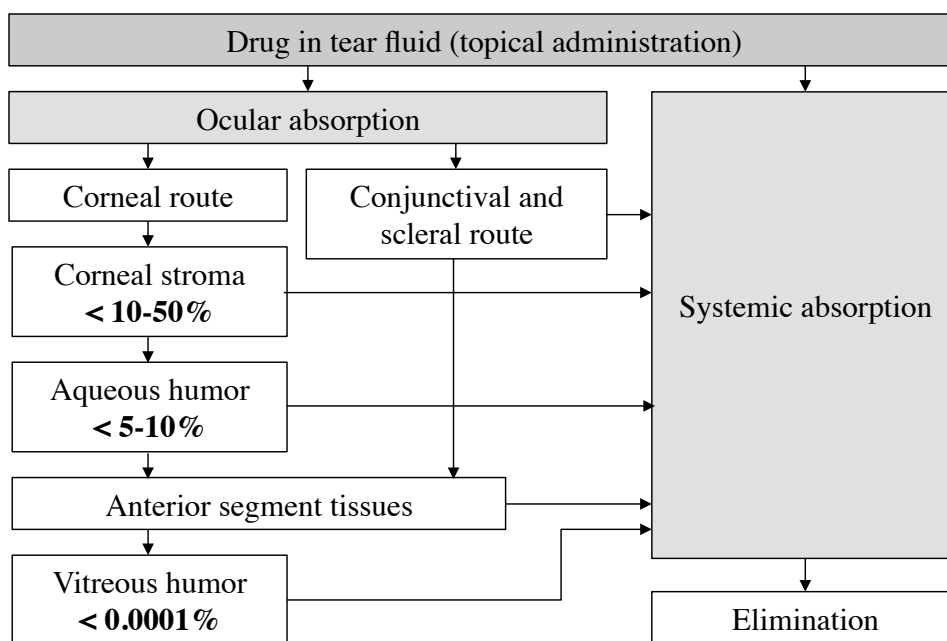
Figure 2.9: Pharmacokinetics of topically applied drugs to the phakic eye. Adapted from [3].

drugs permeate into the aqueous humour [41, 42]. Figure 2.9 summarises the pharmacokinetics of topical administration of drugs.

Several common drug delivery routes and clearance pathways are illustrated in Fig. 2.10. Due to the quick systemic absorption of drugs, drug delivery to the posterior segment of the eye, including the retina, vitreous and choroid, requires high dosages of medication. Medication is, therefore, commonly delivered intravenously or by intravitreal administration. In both cases the dosages are high and surrounding tissue may suffer from side effects. Additionally, frequent (up to every 4 weeks) intravitreal injections are invasive and can cause vitreous haemorrhages, retinal detachment, cataract, and endophthalmitis [43]. Thus, the development of long-term drug delivery systems for the posterior eye is of increasing interest. Intravitreal implants may be one solution to chronic drug administration as they can be loaded with a wide range of drugs and allow for single injection and long-term drug delivery to the posterior segment of the

eye. Intravitreal implants are generally injected into the vitreous or sutured to the sclera. Several nonbioerodible intravitreal implants have been developed and are tested in clinical studies. Iluvien^{TM} (pSivida, Watertown, MA, US) is a rod-shaped insert that fits into a 25 gauge (G) injection needle for the treatment of diabetic macular edema (DME) and has been designed to deliver a small amount of medication (0.2 g/day) over a 24- to 30-months period [44]. The NT-501 (Neurotech Pharmaceuticals, Cumberland, RI, US) consists of encapsulated human cells genetically modified to secret ciliary neurotrophic factor (CNTF) for the treatment of retinal degenerative diseases [45, 46]. It is surgically implanted into the vitreous through a scleral incision and anchored with a suture through a small titanium loop. The implant I-vation^{TM} (SurModics, Eden Prairie, MN, US) consists of a titanium helix coated with triamcinolone acetonide (TA) for the treatment of DME [46]. Ozurdex^{TM} (Allergan, Irvine, CA, US) and Durasert^{TM} (pSivida, Watertown, MA, US) are examples for bioerodible intravitreal inserts. Ozurdex^{TM} is used to treat DME or retinal vein occlusion (RVO) and is composed of a polymer (PLGA) to release incorporated dexamethasone over a duration of four to six weeks [46]. The Durasert^{TM} technology system is designed to be delivered to the subconjunctival space of the eye where it releases latanoprost for predetermined periods of time ranging from days to years [43]. However, not all of the aforementioned implants are approved for clinical use.

All of these intravitreal inserts lack the ability to move and, thus, are not specifically directed to a pathologic site in the eye. Furthermore, the removal of the nonbioerodible implants often requires a vitrectomy, adding to the risk of complications. To overcome these drawbacks, the utilisation of mobile and controllable microrobots has been suggested as a platform for targeted drug delivery to the posterior eye without the need for vitrectomy. Guiding intravitreal inserts to the diseased area allows for much slower release of drugs while providing an equivalent dosage of medication due to the nonlinear nature of Fick's law of diffusion.

(1)	Transcorneal route
(2)	Transconjunctival route
(3)	Intrastromal route
(4)	Intracameral route
(5)	Subconjunctival route
(6)	Intravitreal drug delivery
(7)	Sub-tenon route
(8)	Elimination across trabecular meshwork
(9)	Elimination across uvea
(10)	Elimination across blood-retinal barrier
(11)	Elimination across anterior hyaloid face
(12)	Elimination to systemic lymphatic or vascular circulation
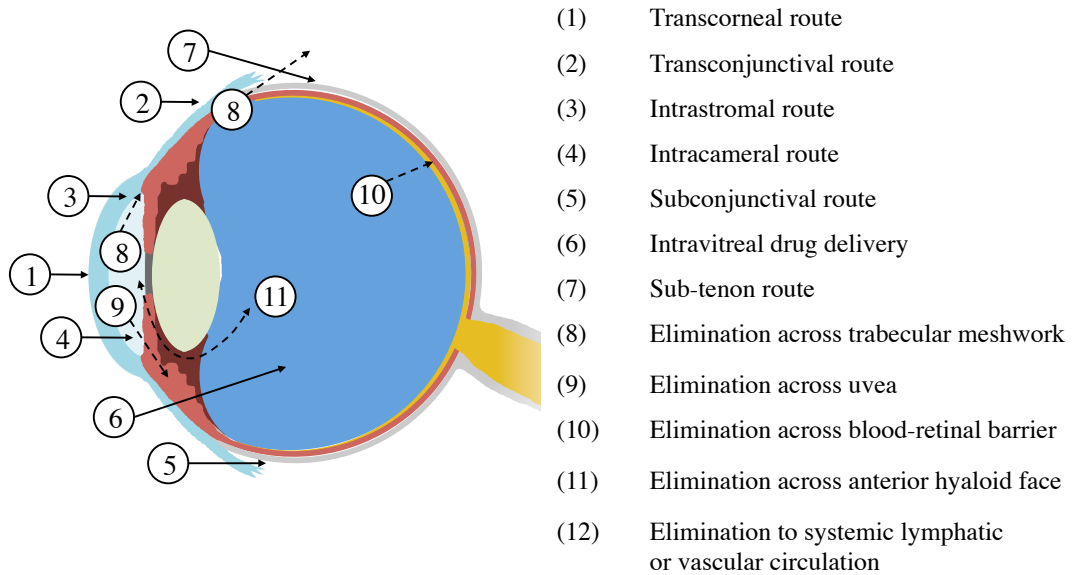
Figure 2.10: Drug delivery routes (solid arrows) and clearance pathways (dotted arrows) for common drug delivery. Adapted from [3].

Chapter 3

Magnetic Manipulation of Ophthalmic Microrobots

Microrobots are defined as miniature robots with a characteristic size of less than 1 mm. Due to their small size, attaching actuators and batteries is impractical and differentiates them from larger robotics. Therefore, microrobots are often powered by external stimuli, such as externally applied magnetic fields. This chapter introduces microrobotic systems, magnetic manipulation of microrobots, and the advantages of using microrobots for ophthalmic applications.

3.1 Microrobotic Systems

Magnetic microrobots show great potential for targeted drug delivery or minimally invasive surgery throughout the human body, as they can be guided wirelessly by external magnetic fields to a pathological site. Possible tasks for biomedical microrobots include targeted therapy, material removal, controllable structures, and telemetry [47]. Due to their small size, microrobotic diagnostic and therapeutic devices will render medical interventions less invasive and may enable new procedures. In order to function in the human body, microrobots must be equipped to swim through specific bodily fluids, and propulsion is often obstructed by small structures in those fluids, such as fibres or microparticles. Many areas in the body exist where microrobots could be employed, such as the blood stream, the central nervous system (brain and spine), or the urinary tract [47]. One benefit of utilising magnetic microrobots for minimally invasive medical applications is that different types of agents can be used according to the surrounding environment. In addition to ellipsoids [48], cylinders [49], or beads, also helical microswimmers [50–52] have been developed.

One organ with high potential for microrobotic surgery is the posterior eye [53], due to the limited accessibility of the eye, where the wireless microrobot must swim through vitreous humour. Microrobots offer an alternative approach for ophthalmic surgery to conventional manual eye surgery or ophthalmic robotic surgery, as described in Chapter 2. Due to the small size of an intraocular microrobot, retinal traction is mitigated, potentially without the need for a vitrectomy. The first wirelessly controlled intraocular microrobot was proposed by Yesin et al. [54] and was visually tracked through the pupil of the eye. An intraocular diagnostic microrobot was proposed that is able to measure oxygen concentration inside the eye based on luminescence quenching [55]. Surface coatings can enhance the biocompatibility and functionality of intraocular microdevices [56, 57]. Figure 3.1 shows several examples of elliptical and cylindrical microrobots developed for intraocular drug delivery and surgery.

3.2   Magnetic Manipulation

Magnetic manipulation systems generate magnetic fields and gradients to guide magnetised objects with high precision and force feedback. Magnetic fields and gradients can be generated by two basic principles: permanent magnets or electromagnets. While permanent magnets exhibit a large field strength to volume ratio, electromagnets can be controlled and simply switched off [59]. Thus, for medical applications, electromagnets are beneficial in terms of controllability and safety.

3.2.1   Magnetic Manipulation for Ophthalmic Application

Microrobotic tools for sutureless ophthalmic surgery are rapidly gaining interest as *in vivo* diagnostic and therapeutic devices [60, 61]. The first electromagnetic system for ophthalmic surgery was developed in 1877 [62]. A metallic particle was successfully removed from the eye using the system during surgery in 1879. The electromagnetic system is illustrated in Fig. 3.2(a). In 1974 Charles D.

(b)

Figure 3.1: (a) An elliptical intraocular microrobot, before and after assembly, and on a chick chorioallantoic membrane (CAM). (b) A cylindrical intraocular microrobot, shown with different surface coatings and inside a living rabbit eye. The images were adapted from [47, 54] and [58], respectively.

Kelman, better known for the development of phacoemulsification, first introduced the idea of the *phaco fly*, a wireless magnetic device that is slowly rotated in the capsular fornices to disrupt the cortex during cataract surgery [63]. For

(a)   (b)
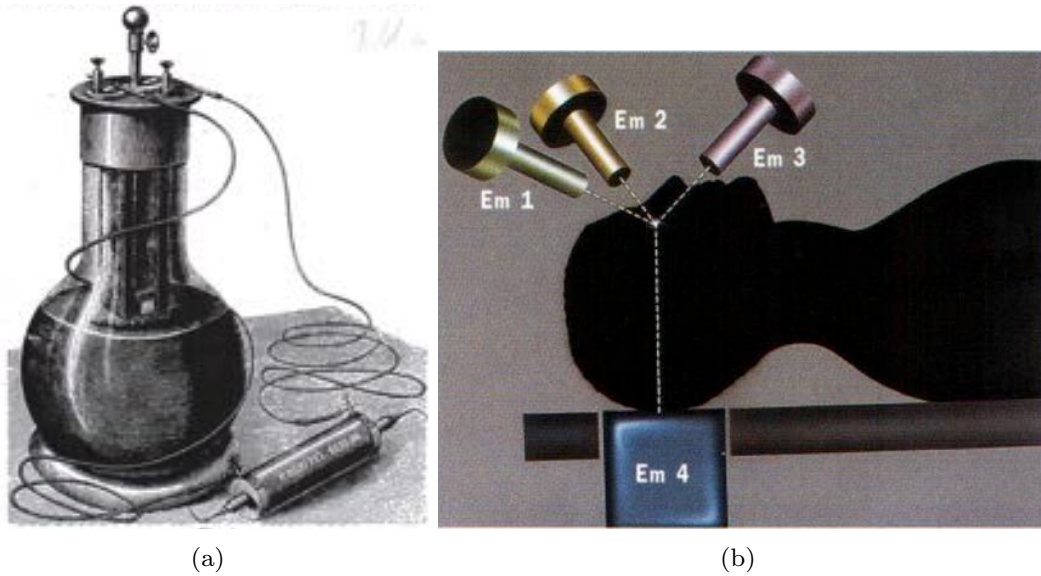
Figure 3.2: (a) The first electromagnetic system for the extraction of metallic particles from the eye designed in 1877. (b) The electromagnetic manipulation system designed by Kelman in 1974. Images are taken from [62] and [63], respectively.

this. Kelman used an electromagnetic manipulation system consisting of four electromagnets positioned around the head, as illustrated in Fig. 3.2(b). Intravitreal injection of a silicone magnetic fluid that incorporates ferromagnetic nanoparticles was suggested as a tamponading agent to alleviate retinal detachments and other types of retinopathy [64, 65]. During *in vitro* experiments the ferromagnetic fluid was injected into a model eye placed in a magnetic field, so that the nanoparticles interstitially diffused toward the magnetic source. Recent work shows the actuation of a single-hinged microswimmer, the *microscallop*, that can swim through non-Newtonian media [66]. Propulsion of the structure was achieved in hyaluronic acid, one of the components of the vitreous humour, and thus shows potential for drug delivery in the eye, although the work did not consider the heterogeneous collagen fibre network as an obstacle.

Recent emerging technologies have paved the way for magnetically guided tools for minimally invasive surgery. These tools allow for more flexible robotic in-

creased stability and precision, and minimise the risk of perforation of tissue [67–69]. Typically, magnetically guided surgical systems are comprised of a tethered magnetic tool, such as a flexible catheter, in an externally applied magnetic field. During medical procedures magnetic tools can be precisely positioned by systems utilising permanent magnets [70] or electromagnets [71], which generate controlled magnetic fields and magnetic field gradients. Moreover, magnetically guided untethered microrobots have been proposed as surgical tools and as platforms for targeted drug delivery in ophthalmic application [49]. In 2010 Kummer et al. proposed an electromagnetic system for guidance of wireless microrobots inside the vitreous humour in the eye, called OctoMag [72]. The system consists of eight electromagnets with soft-magnetic cores in a hemispherical arrangement with a central workspace of $20 \times 20 \times 20$ mm, which approximately fits a human eye. A computer controls the amount of current in each coil and, thus, monitors the generated magnetic fields and gradients that are generated. The system, shown in Fig. 3.3, applies magnetic fields up to 40 mT and magnetic gradients up to 1 T/m to a magnetic device in the central workspace. The workspace is observed through an ophthalmic microscope equipped with a CCD camera and a wide field enhanced BIOM lens for wide-angle imaging of the retina. Figure 3.4 illustrates the fast decay of magnetic field with increasing distance from the central workspace. At a distance of 300 mm from the central workspace, which is approximately the distance between the eye and heart, the magnetic fields have decreased to approximately 5% of the applied field magnitude. The system provides high precision in medical procedures in a minimally invasive manner and allows for force feedback below the human force perception threshold. The OctoMag is teleoperated, potentially allowing surgeons to operate on patients remotely.

3.2.2   Governing Equations

The magnetic flux density $\mathbf{B}$ in [T] is derived by $\mathbf{B} = \mu_0 \mathbf{H}$, where the permeability of vacuum is given by $\mu_0 = 4\pi \times 10^{-7}$ Tm/A. When an external

(a)   (b)
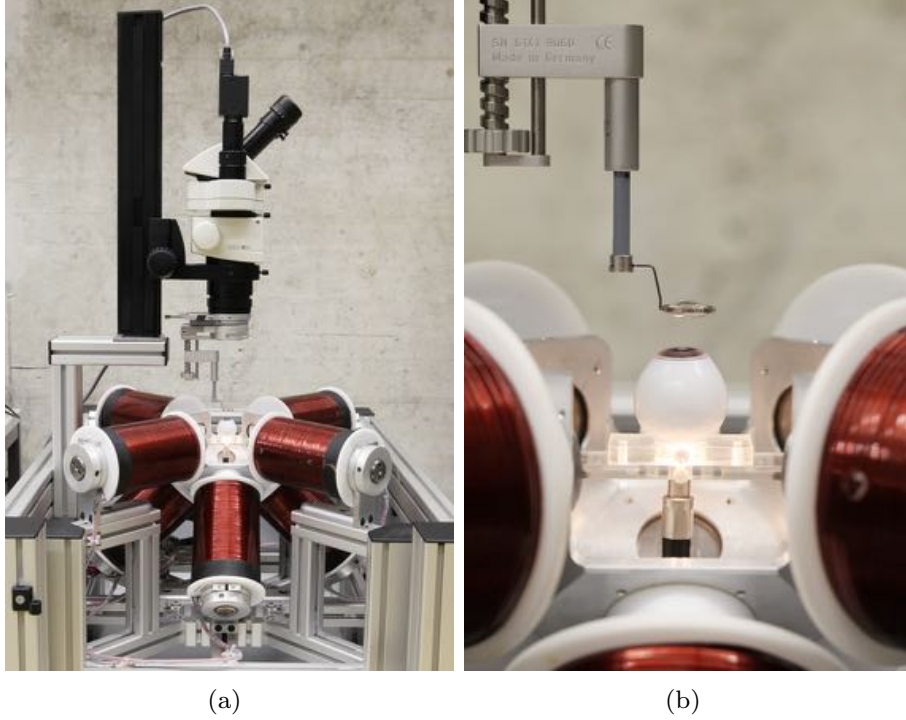
Figure 3.3: (a) Electromagnetic manipulation system, OctoMag, for 3D control of tethered or untethered intravitreal microrobots. The workspace is observed with an ophthalmic microscope equipped with a charge coupled device camera and a wide-angle BIOM lens. (b) A magnification of the OctoMag workspace with an eye phantom.

magnetic field is generated, the magnetic torque per volume

$$\mathbf{T} = \mathbf{M} \times \mathbf{B} \tag{3.1}$$

in $[\mathrm{N/m^2}]$ aligns a magnetic microrobotic device inside the central workspace with the applied field $\mathbf{B}$. As no electric current flows through the workspace occupied by the device, $\nabla \times \mathbf{B} = 0$, and

$$\mathbf{F} = (\nabla \cdot \mathbf{B})^T \mathbf{M} = \begin{bmatrix} \frac{\partial \mathbf{B}}{\partial x} & \frac{\partial \mathbf{B}}{\partial y} & \frac{\partial \mathbf{B}}{\partial z} \end{bmatrix}^T \mathbf{M} \tag{3.2}$$
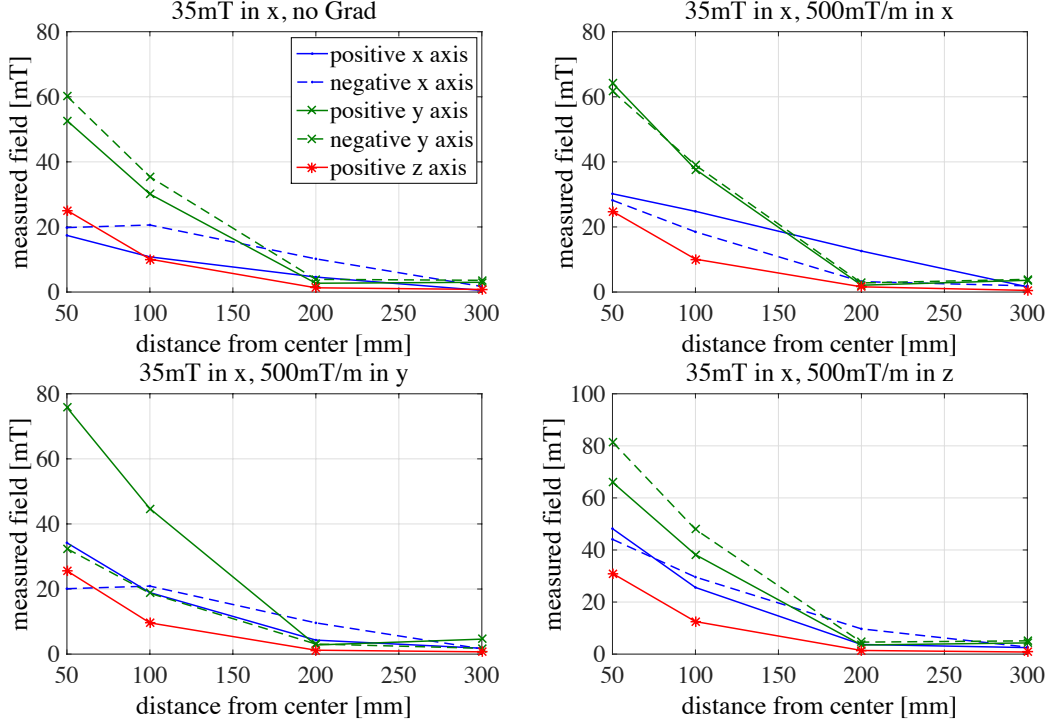
Figure 3.4: Magnetic field decrease with increasing distance from the central workspace of the magnetic manipulation system OctoMag.

the magnetic force per volume in $[\mathrm{N/m^3}]$ can be written as

$$\mathbf{F} = (\mathbf{M} \cdot \nabla)\mathbf{B}. \tag{3.3}$$

The OctoMag consists of eight electromagnets that each create a magnetic field, which can be precomputed. The magnetic field at a point $\mathbf{P}$ in the workspace due to activating a single electromagnet e is given as

$$\mathbf{B}_e(\mathbf{P}) = \tilde{\mathbf{B}}_{\mathbf{e}}(\mathbf{P})i_e, \tag{3.4}$$

where $\tilde{\mathbf{B}}_{\mathbf{e}}$ is the unit contribution and i_e is the current in coil e, respectively. By imposing the fields generated by all electromagnets at a point $\mathbf{P}$ in the

workspace the field at this point is derived as

$$\mathbf{B}(\mathbf{P}) = \sum_{e=1}^{8} \tilde{\mathbf{B}}_e(\mathbf{P}) i_e = \mathcal{B}(\mathbf{P}) I \tag{3.5}$$

where vector I holds the currents in each coil and $\mathcal{B}(\mathbf{P})$ is a 3×8 unit field contribution matrix that can be analytically calculated online or interpolated from precomputed or measured points. Magnetic force and torque applied to the catheter tip can be expressed as

$$\begin{bmatrix} \mathbf{T} \\ \mathbf{F} \end{bmatrix} = \begin{bmatrix} Sk(\hat{\mathbf{M}})\mathcal{B}(\mathbf{P}) \\ \hat{\mathbf{M}}^T \frac{\partial \mathcal{B}}{\partial x}(\mathbf{P}) \\ \hat{\mathbf{M}}^T \frac{\partial \mathcal{B}}{\partial y}(\mathbf{P}) \\ \hat{\mathbf{M}}^T \frac{\partial \mathcal{B}}{\partial z}(\mathbf{P}) \end{bmatrix} \begin{bmatrix} i_1 \\ \vdots \\ i_8 \end{bmatrix} = \mathcal{A}(\hat{\mathbf{M}}, \mathbf{P}) I \tag{3.6}$$

where the eight electromagnet currents are mapped to magnetic force and torque through the 6×8 actuation matrix $\mathcal{A}(\hat{\mathbf{M}}, \mathbf{P})$ and $Sk(\hat{\mathbf{M}})$ is the skew-symmetric matrix form of $\hat{\mathbf{M}}$. To remove any dependencies on the magnetic properties of the catheter tip material the magnetisation $\mathbf{M}$ is normalised with respect to the volume magnetisation of the material in $[\text{Am}^2]$ and written as $\hat{\mathbf{M}}$. For a desired torque/force vector to manipulate the magnetic microrobot, the required currents in the electromagnets can be found by using the pseudoinverse of $\mathcal{A}$

$$I = \mathcal{A}(\hat{\mathbf{M}}, \mathbf{P})^{\dagger} \begin{bmatrix} \mathbf{T_{des}} \\ \mathbf{F_{des}} \end{bmatrix} \tag{3.7}$$

A detailed mathematical model describing the OctoMag can be found in [72]. Figure 3.5 visualises the reaction of an untethered and a tethered magnetic device to the change of orientation of the magnetic field (magnetic torque) and the magnetic field gradient (magnetic force). An untethered microdevice rotates with the orientation change of an externally applied magnetic field while it undergoes translational movement due to a changing magnetic field gradient. However, a tethered magnetic device bends due to both, a changing field rotation and the changing gradient of an orthogonal magnetic field.
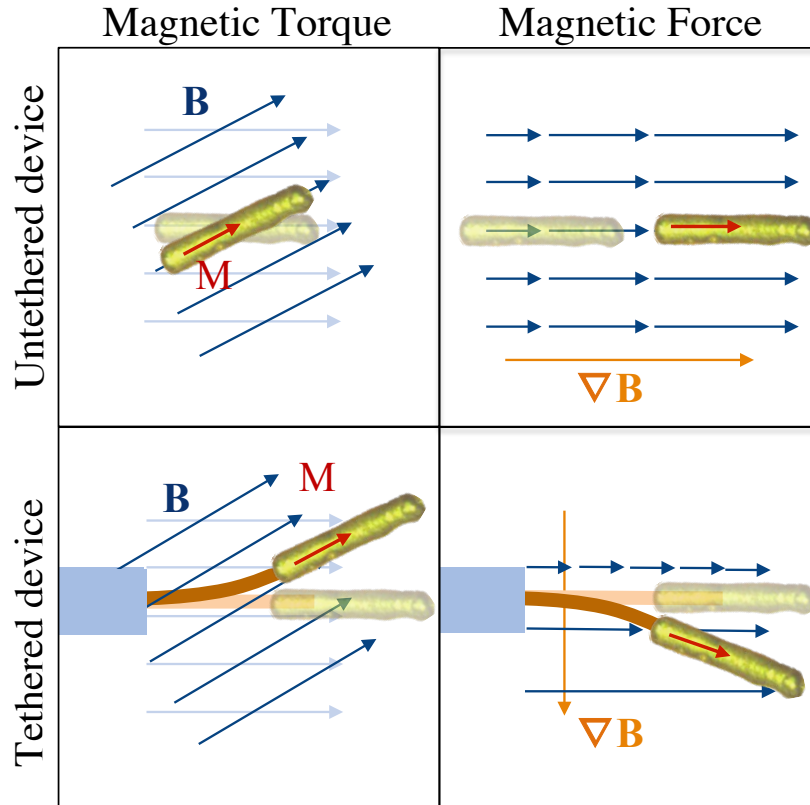
Figure 3.5: A tethered or untethered magnetic device's reaction to change of magnetic field orientation (magnetic torque) and gradient of the magnetic field (magnetic force).

3.3   Patient Safety

Utilising magnetic fields and gradients for surgery has gained increasing interest in the medical community due to patient safety considerations. Several electrically assisted methods to optimise drug delivery have been suggested, such as ultrasound, electroporation or photodynamic therapy, whereas magnetic fields have been shown to penetrate deeply into human tissue while being very safe. The high degree of patient safety in magnetic fields arises from the small value of magnetic susceptibility of biological tissue. To limit magnetic forces generated by implants or other ferromagnetic objects inside the body, the

exposure limit that has been suggested by the ICNIRP (International Commission on Non-Ionising Radiation Protection) is 400 mT for quasi-static magnetic fields (<1 Hz) [73]. Peak exposure limits are much higher for occupational exposure ($2 - 8$ T), if the work environment is controlled.

The magnetic manipulation system, OctoMag, used for medical procedures in the eye, generates magnetic fields up to 40 mT, which is about one hundredth of the fields generated in a conventional magnetic resonance imaging (MRI) scanner and 200 times lower than the maximum suggested safe magnetic field strength for an adult human. Moreover, the magnetic fields in the OctoMag decrease rapidly with increasing distance from the central workspace, as illustrated in Fig. 3.4. Minimally invasive microrobots for intraocular drug delivery or surgery have been proposed that have a cylindrical shape with an outer diameter of 285 μm and fit into a 23 G injection needle for a single injection into the patients eye without suture [74]. The microrobots are rendered non-toxic by using biocompatible bulk materials and/or polymer or metal-based coatings. Smaller incisions in the eye attribute for faster recovery, less scarring and fewer complications during procedures and lead to improved patient safety.

3.4   Teleoperated Surgery

The first robot-assisted surgical procedure that was carried out from a distance, i.e. telesurgery, was reported in 2001 by Marescaux et al. [75]. Teleoperated robot-assisted microsurgery can decrease the fatigue an ophthalmic surgeon experiences after several hours of surgery. Furthermore, the use of teleoperated systems reduces the personnel and infrastructure required in an operating theatre, potentially lowering the cost of healthcare. Patients, as well as doctors, benefit from the ability to perform surgical procedures from a distance, which enables specialist surgeons to provide help to patients living in remote areas with limited access to healthcare without having to travel, thus, overcoming geographical constraints.

Like most magnetic manipulation systems, the OctoMag can be teleop-

erated via a computer. The graphical user interface allows the ophthalmic surgeon to choose the mode of input. The doctor chooses between manual control, which implies steering an intravitreal microrobot with a joystick, and automated control, where the integrated controller moves the microrobot on a predefined path. All surgical data are processed automatically and can be stored for future use. Furthermore, a surgeon's movement and technique can be recorded for teaching less-experienced surgeons or the system itself.

3.5   High Precision Control

Currently, no commercially available intravitreal insert used for drug delivery to the posterior eye has the ability to be directed to the pathological site and target it directly without affecting healthy surrounding tissue. Furthermore, the removal of many non-bioerodible inserts requires a vitrectomy thus adding further risk of complications. Using magnetically controlled microrobots to deliver drugs to a targeted site inside the eye shows great potential to decrease the required dosage while maintaining the same concentration of medication at the diseased area due to the nonlinear nature of Fick's law of diffusion, which states that the concentration is highest closest to the source, as illustrated qualitatively in Fig. 3.6. By magnetically guiding a drug-loaded microrobot to a pathological site directly, the precision of drug delivery can be increased dramatically, thus, effecting healthy tissue less.

Furthermore, the trend in surgical ophthalmology is towards minimally invasive procedures and smaller instruments. Controllable intravitreal microrobotic tools allow for future sutureless ocular surgery. The small size of these tools can gain access to small organs and structures in the body and allows for better accuracy of surgical procedures. The precision of an ocular microrobot that is magnetically controlled inside the vitreous humour depends mainly on the camera resolution and the magnification of the ophthalmic microscope. The magnetic actuation system places no constraints on the precise positioning of the ophthalmic microrobot.
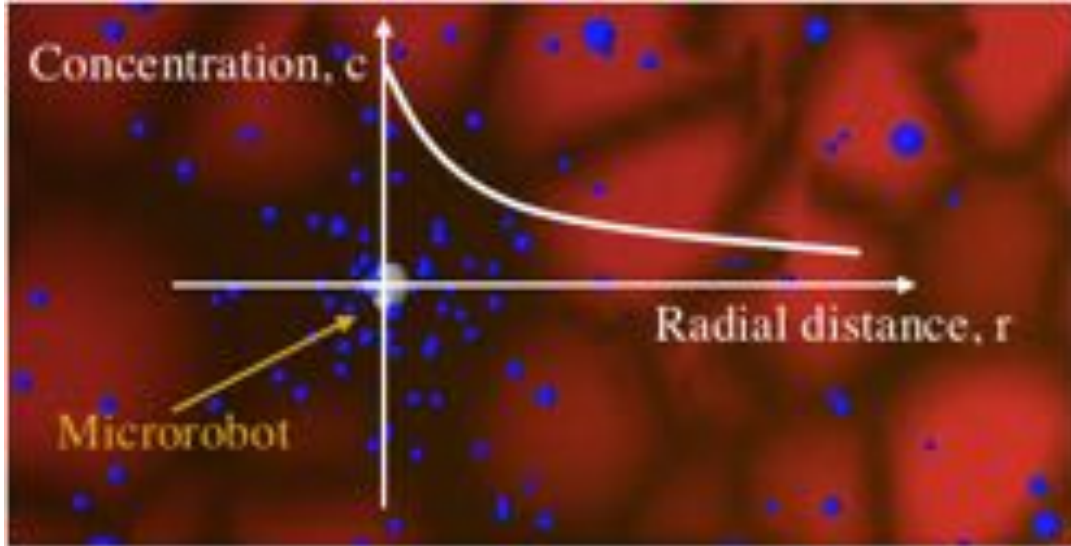
Figure 3.6: Qualitative visualisation of Fick's law of diffusion. The drug concentration, c, is highest at the source (in this case a microrobot) and decreases with the radial distance, r.

3.6 Force Feedback

Studies have shown that roughly 75% of all forces applied during ophthalmic procedures are 7.5 mN in magnitude or lower. Less than 20% of these forces could be felt by a surgeon [17] and, therefore, lie below the human force perception threshold. Hence, in many cases ophthalmic surgeons are not able to feel interactions between a tool and the delicate tissues in the eye and, therefore, require significant levels of training, dexterity and experience. An electromagnetic manipulation system, such as the OctoMag, allows for direct force and torque feedback from the applied magnetic fields and gradients if the magnetisation of the microrobotic tool is known. The force F in [N] and the torque T in [Nm] that an untethered microrobot applies to surrounding tissue can be derived as in Equation 3.6. Restriction of the applied forces and torques by an upper threshold minimises the risk of damaging the delicate tissues in the eye, thus, increasing patient safety.

Chapter 4

Wireless Microrobots for Ophthalmic Applications

Several intravitreal inserts have been suggested for targeted treatment of retinal diseases, as outlined in Section 2.4. These ocular inserts lack the ability to move and, therefore, cannot be safely directed to a pathologic site within the eye. Additionally, the removal of some of these devices requires a vitrectomy, which bears risks of complications. The addition of mobility to intravitreal devices to guide them to the diseased area will allow much slower release drug delivery, while providing an equivalent dosage to the pathology due to the nonlinear nature of Ficks law of diffusion. This chapter summarises the manoeuvrability of wireless cylindrical intravitreal microrobots through *ex vivo* and *in vivo* experiments [74], investigates swimming characteristics of helical microrobots in fibrous vitreous phantoms [76], and demonstrates possible applications, such as the removal of vitreous floaters.

Animal studies described in this chapter have been planned and performed in cooperation with Christos Bergeles, Sandro Erni, Juho Pokki, and Olgac Ergeneman from the Multi-Scale Robotics Lab, as well as Simon Pot, Bernhard Spiess, and Katja Nuss from the Animal Hospital Zurich. *Ex vivo* experiments were performed in porcine cadaver eyes with the support of Sandro Erni. Swimming experiments with helical microrobots were conducted by Alexandra Wood throughout her Semesterthesis and structures were fabricated by Famin Qiu and Tianyun Huang. The removal of vitreous floaters using microrobots was investigated in cooperation with Fabian Schwab throughout his Semesterthesis, while removal of a microrobot from the eye was demonstrated in Gabriel Jae Park's Bachelorthesis.

<div align="center">(a)   (b)</div>
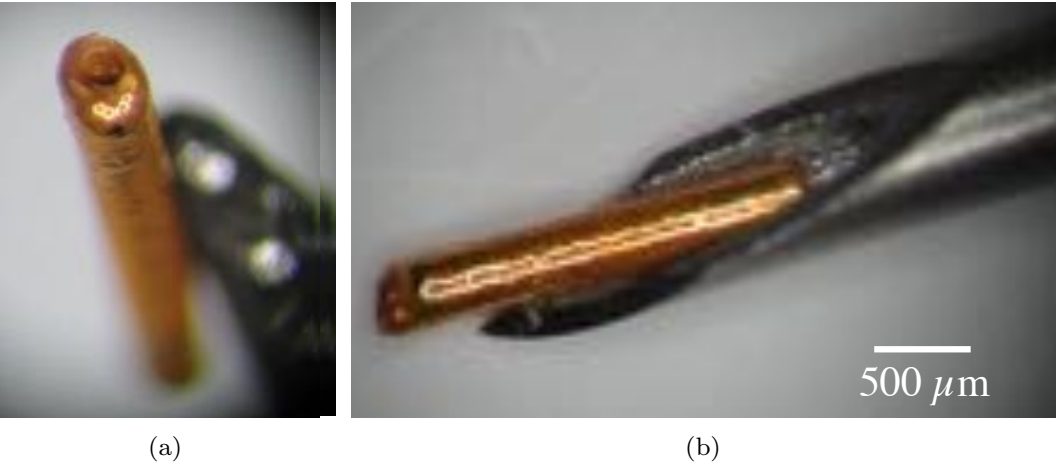
Figure 4.1: (a) Cylindrical intravitreal microrobot for *in vivo* experiments outer diameter of 285 μm, inner diameter of 125 μm, and length of 1800 μm. (b) Intravitreal microrobot inside a 23 gauge injection needle for sutureless injection.

4.1   Wireless Microrobots

Figure 4.1 shows a microrobot, which is injected into the posterior section of the eye through the *pars plana* region of the sclera. The microrobot is wirelessly controlled and can be removed by a magnetic tool. The soft magnetic microrobot has the shape of a hollow cylinder with outer diameter of 285 μm and inner diameter of 125 μm; its length is 1800 μm. The outer diameter is chosen such that the microrobot fits a 23 G needle, as shown in Fig. 4.1(b). Its shape was designed to include a drug reservoir for targeted drug therapy. The cylindrical microrobot was fabricated by electroforming cobalt-nickel (CoNi) on an aluminium wire [49] and is rendered nontoxic using polypyrrole or inert metallic coatings, which have been tested for cell viability [77]. Customised fabrication methods allow for high flexibility in diameter, length, and magnetic volume of the microdevice [77, 78].

4.2   Intravitreal Microrobot Mobility Experiments

The manoeuvrability of intraocular microrobots as potential tools for microsurgery is investigated to understand robot mobility in the posterior eye seg-

ment in vitreous humour as well as after replacement of the vitreous with different media *ex vivo* and *in vivo*.

For *in vivo* experiments, protocols concerning animal housing, treatment, and monitoring were approved by the Swiss Veterinary Office according to the Swiss decree on animal protection [79] and adhere to the ARVO Statement for the Use of Animals in Ophthalmic and Vision Research. This study was undertaken in cooperation with ophthalmologists from the University Hospital Bern and the Veterinary Hospital Zurich.

4.2.1 *Ex vivo* Studies in Porcine Eyes

It has been suggested that the viscoelastic behaviour of the central vitreous region of a pig closely resembles that of the central vitreous region of a human eye in terms of rheological parameters [80]. The same study reports that the anterior and posterior regions of the porcine vitreous resemble a dense gel, whereas the human vitreous has a thinner and in some cases aqueous consistency. Similarly, it has been observed that human vitreous undergoes liquefaction with increasing age [9]. It can be concluded that, with respect to the properties of the vitreous humour, porcine eyes act as a stiff model of the human eye. In order to account for the rapid loss of hyaluronic acid of the vitreous upon removal from the eye globe and to sustain the intraocular pressure, microrobotic mobility experiments are conducted inside the eye globe without destroying the natural structure of the eye. *Ex vivo* experiments in porcine cadaver eyes are performed less than three hours *post mortem*.

4.2.2 *In vivo* Studies in Lapine Eyes

In order to evaluate the ability of intravitreal microrobots to move in the living eye, *in vivo* mobility experiments were conducted in rabbits. Due to their characteristic bright red eyes, the New Zealand white rabbit breed (9-month-old females) was chosen for this study. Experiments are undertaken in five individual rabbit eyes, three of which are vitrectomised. One eye is subsequently filled with balanced salt solution (BSS) and two with silicone oil (viscosity

(a)   (b)
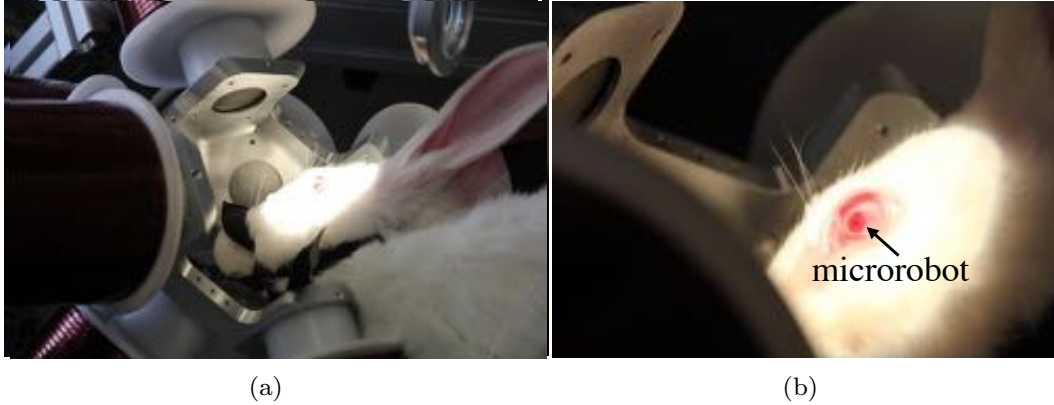
Figure 4.2: (a) Anaesthetised rabbit placed with the studied eye centrally in the OctoMag workspace. (b) Intravitreal microrobot inside *in vivo* lapine eye.

$1000 \, \text{mm}^2/\text{s}$ at $25 \, °\text{C}$). The rabbit is anaesthetised and its head is placed inside the workspace of the OctoMag, such that the eye is located in its centre, as illustrated in Fig 4.2.

4.2.3   Mobility Experiments

A microrobot is injected into the central vitreous humour of the porcine or lapine eyes with a syringe equipped with a 23 G needle. After insertion of the microrobot, the eye is placed centrally in the workspace of the OctoMag for experimentation and observed through a microscope. After experimentation the microdevice is removed from the vitreous cavity using a magnetic tool, outlined in Section 4.5.

4.2.3.1   Motion Tracking

The microscope equipped with a camera (Pointgrey, BC, Canada) takes consecutive images of the inside of the eye globe with a frequency of $15 \, \text{Hz}$. In order to track the microrobot movement a script is written in MATLAB, which returns the robot orientation and position in every image. Due to minor movement of the rabbit eye during *in vivo* experiments, noise occurs and the microrobot position data must be filtered using a moving average filter with window size

of 10 data points for further analysis.

4.2.3.2   Rotational Mobility

The intraocular microrobot is rotated in the plane, normal to the line of vision in the posterior region of the eye. The rotation of the microrobot is caused by the rotation of the applied magnetic field, which is generated by the OctoMag. The microrobot rotational mobility is examined in lapine vitreous, BSS, and silicone oil *in vivo* and in porcine vitreous *ex vivo*. In order to evaluate the rotational mobility of an untethered intraocular microrobot and its response to magnetic field strength, the field magnitude is set to 10, 20, 30, and 40 mT, whereas the field's rotational frequency is held constant at 1 Hz and the intraocular microrobot mobility is recorded. In a second series of experiments, the rotation of an intraocular microrobot is investigated at constant field magnitude, whereas the field rotation frequency is set to 0.05, 0.1, 0.5, 1, and 2 Hz. For experiments in vitreous and silicone oil the field magnitude is held constant at 30 mT. It is set to a lower field magnitude (10 mT) for experiments in BSS due to an unstable response of the microrobot in BSS at higher field strengths.

Results

As a result of the rotating magnetic field, the intraocular microrobot follows the field with a time delay. Figure 4.3(a) indicates the angle of rotation of the magnetic field, α_{field}, and the angle of rotation of the microrobot, α_{robot}. The response of the robot to a 10 mT field rotating counter clockwise with frequency of 0.5 Hz is illustrated in Fig. 4.3(b). A black arrow indicates the orientation of the magnetic field.

Figure 4.4 graphs the angle of rotation of an applied magnetic field at various field magnitudes, rotating at 1 Hz, and the rotation of a microrobot inside the eye over time, where T is the period of rotation in seconds ($T = 1$ s). Figure 4.4(a) illustrates microrobot rotation in lapine vitreous (*in vivo*), subfigures 4.4(b) and 4.4(c) show the microrobot movement in silicone oil and BSS (*in*
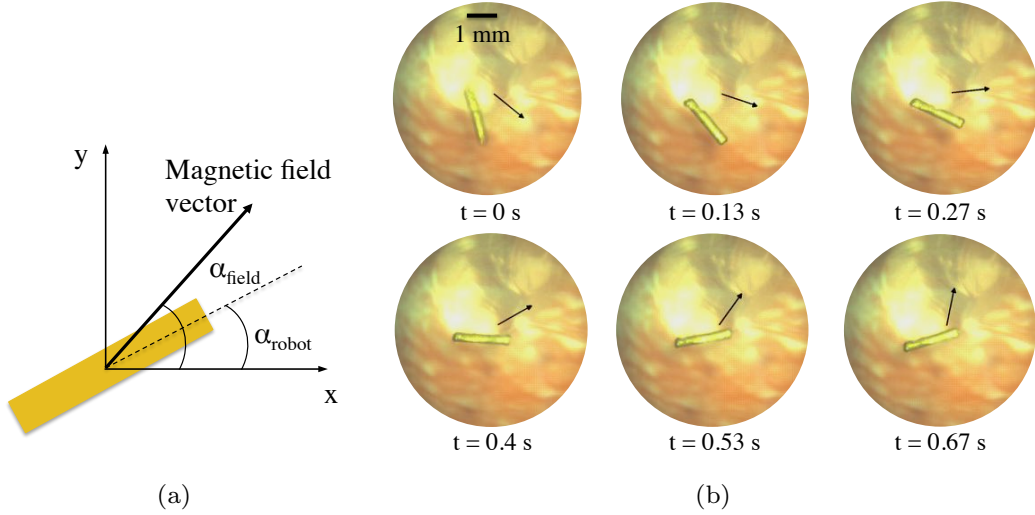
Figure 4.3: (a) Inertial coordinate frame, where the x-y plane is perpendicular to the line of vision. (b) A gold-coated intravitreal microrobot inside the vitreous of a live rabbit. As the applied magnetic field (black arrow) rotates counter clockwise, the microrobot follows with a time delay.

vivo), respectively. Figure 4.4(d) shows the rotational motion of the microrobot in porcine vitreous (*ex vivo*). It is observed that the measured angles of rotation show almost no change for different field magnitudes in all four surrounding media. The time delay of the microrobot rotation compared to the field rotation is similar for all recorded field magnitudes at constant frequency in each medium. Therefore, it is concluded that the magnitude of the rotating magnetic field has no influence on the time delay of the microrobot. Unlike in vitreous, the microrobot shows very unstable movement in BSS at 40 mT (not plotted). This instability of the microrobot can be explained with an increasing magnetic drift inside the OctoMag workspace due to the increasing field strength. Furthermore, the viscosity of BSS is much lower than that of vitreous, thus, less damping of the movement is observed and instabilities are less controllable. In porcine vitreous the microrobot movement is hindered at field strength of 10 mT (not plotted), presumably due to collagen fibres inside the vitreous.
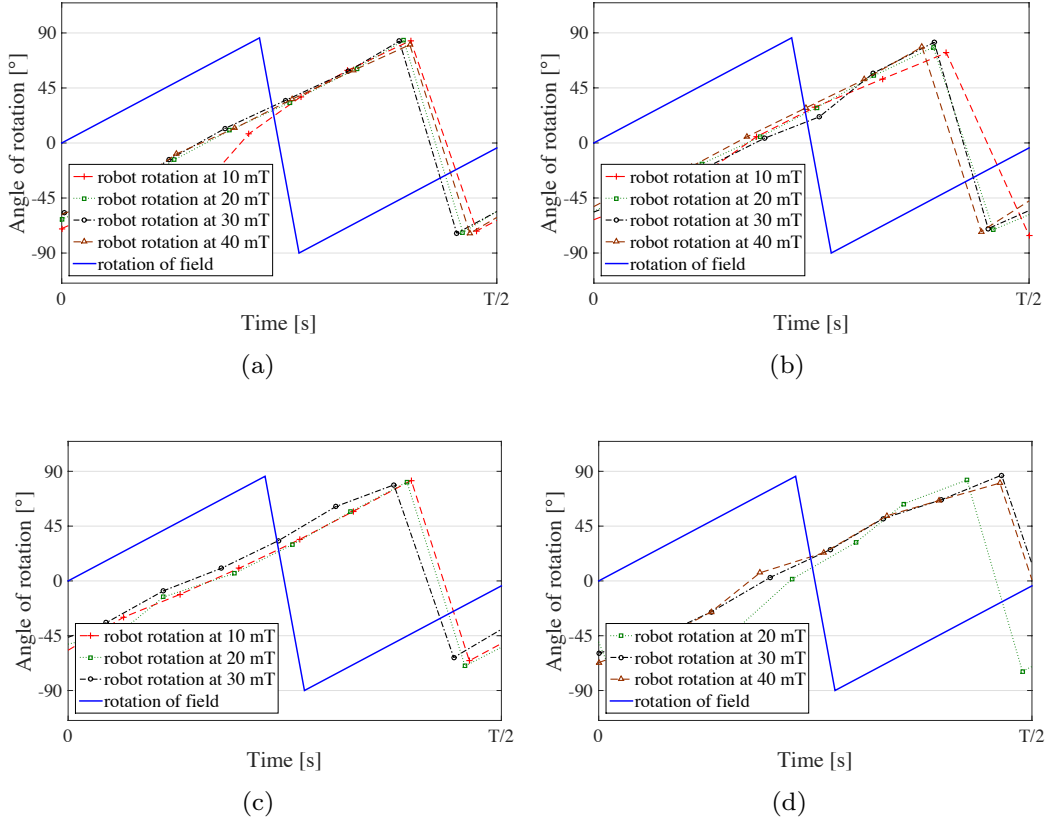
Figure 4.4: Angle of rotation of the applied magnetic field (rotation frequency 1 Hz) and the microrobot (a) in lapine vitreous (*in vivo*), (b) inside the lapine eye in silicone oil (*in vivo*), (c) inside the lapine eye in BSS (*in vivo*), (d) porcine vitreous (*ex vivo*) at field magnitudes 10, 20, 30, 40 mT.

Figure 4.5 illustrates the angle of rotation of the rotating magnetic field and the intraocular microrobot surrounded by the various media. The rotation is plotted against time, where T is the period of rotation at a corresponding frequency. It is observed, that the relative time delay between the field angle of rotation and the microrobot rotation increases with decreasing period T, and thus increasing field frequency. It is concluded that the time delay between robot rotation and the rotating magnetic field corresponds to rotational field frequency. Furthermore, it is observed that the time delay between angle of rotation of the field and the microrobot is generally larger in vitreous (lapine
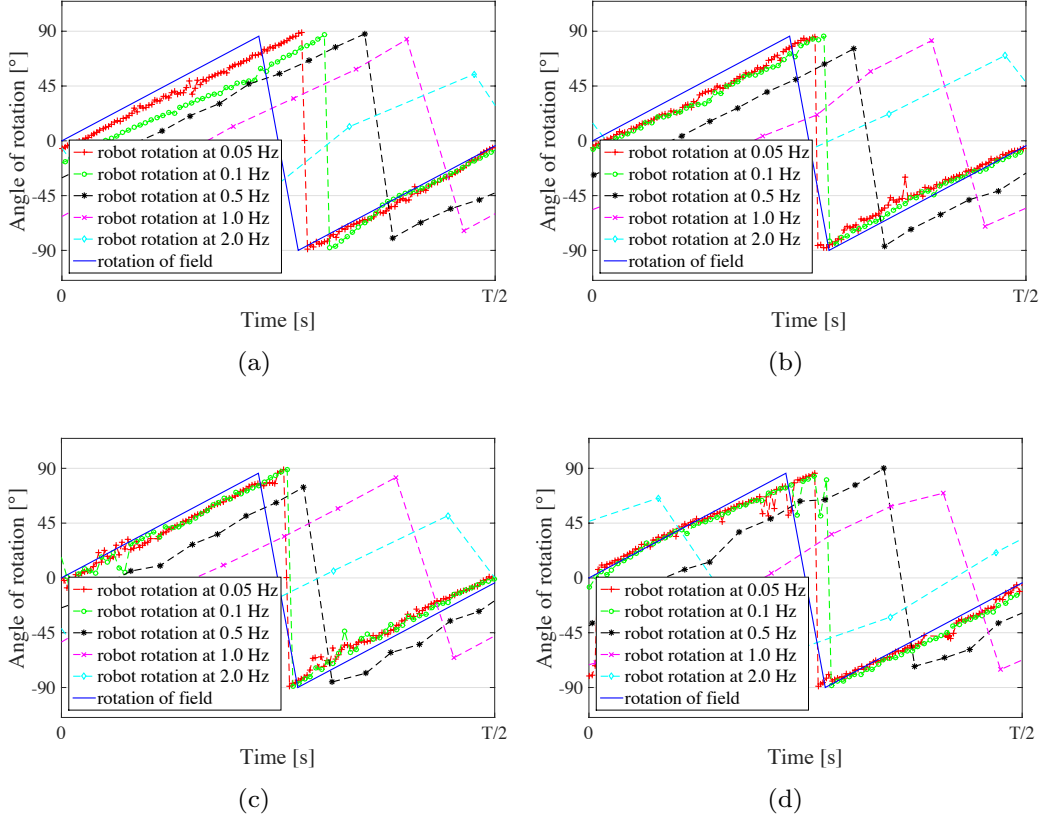
Figure 4.5: Angle of rotation of the applied magnetic field at frequencies 0.05, 0.1, 0.5, 1, 2 Hz and the microrobot (a) in lapine vitreous (*in vivo*, 30 mT), (b) inside the lapine eye in silicone oil (*in vivo*, 30 mT), (c) inside the lapine eye in BSS (*in vivo*, 10 mT), (d) porcine vitreous (*ex vivo*, 30 mT).

and porcine) than in BSS and silicone oil. This observation is attributed to the presence of elastic collagen fibres in the vitreous.

As suggested in the literature, vitreous is not only a viscous fluid but also has elastic properties [81], which are observed in some experiments described in this chapter. Figure 4.6 shows the corresponding plots for such a case, where the microrobot is unable to accomplish a full rotation due to being caught in collagen fibres. The figure shows an applied magnetic field rotating at a frequency of 0.5 Hz with a magnitude of 30 mT. When the angle between the
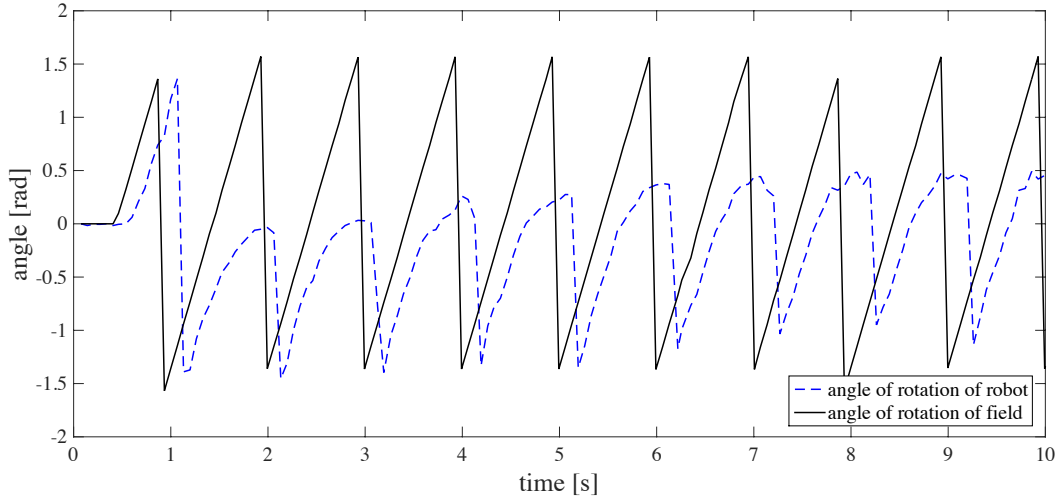
Figure 4.6: Angle of rotation of the applied magnetic field (10 mT) and the microrobot in lapine vitreous (*in vivo*) at field rotation frequency 0.5 Hz.

magnetic field and the microrobot becomes larger than 90°, the microrobot quickly aligns with the field and, subsequently, starts following the field with a delay until it pauses again. Using a microscope, thin collagen fibre bundles were observed that are attached to the intravitreal microrobot. Therefore, it is concluded, that the insert is entangled in the elastic fibres, which constrain the microrobot mobility in vitreous.

In order to compare the mobility of an intraocular microrobot in different media, Figure 4.7 summarises the correlation between the relative time delay of a microrobot in lapine and porcine vitreous, BSS and silicone oil, and the rotation of the magnetic field. The relative delay, defined by the time delay normalised by the period of rotation, is plotted against the period and its frequency in the surrounding media. The figure illustrates that relative time delay decreases with decreasing frequency and thus, increasing period T.

4.2.3.3   Translational Mobility

In order to examine the translational mobility of the microrobot inside the eye globe, a magnetic gradient is applied. The magnetic field gradient is increased
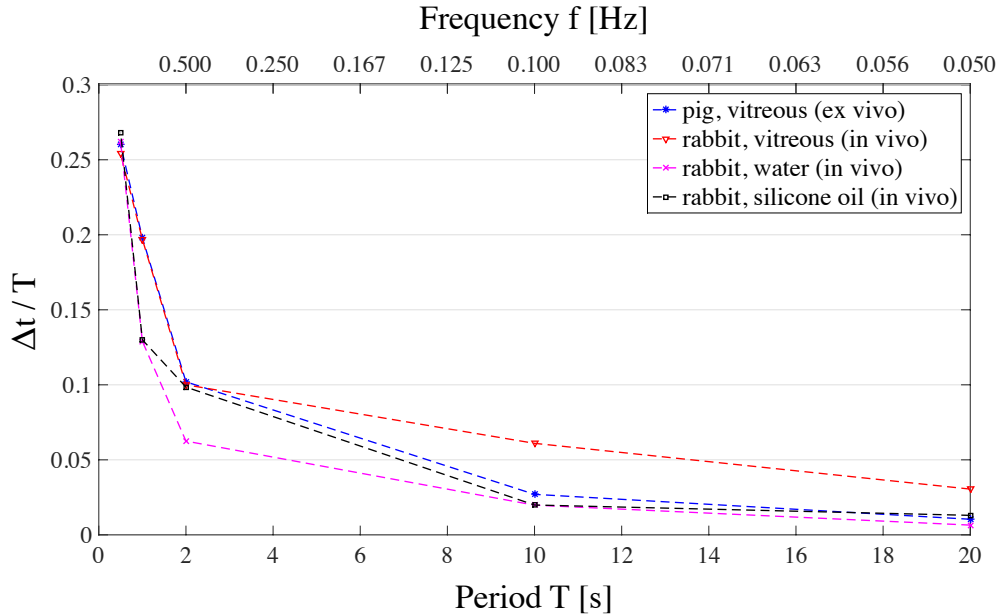
Figure 4.7: Ratio between the time delay of the microdevice to the field rotation and the period of the field rotation T, plotted against the period of the field rotation in seconds.

from 0 to $500\,\mathrm{mT/m}$, resulting in translational movement of the intraocular microrobot, whereas the field magnitude and orientation are held constant for each experiment. Experiments are undertaken for magnetic field magnitudes of 10, 20, 30, and 40 mT. Furthermore, the translational mobility of the microdevice in porcine and lapine vitreous is compared.

Results

The force resulting in the translation of the intraocular microrobot is caused by an applied magnetic field gradient generated by the OctoMag. Figure 4.8 shows four consecutive images of a wireless microrobot inside the vitrectomised rabbit eye, surrounded by BSS. A magnetic field gradient is applied along the horizontal direction causing the microrobot to translate along this axis. Figure 4.9(a) illustrates translational movement of a microrobot in lapine vitreous. The solid red line shows the position of the microrobot as a result of an increasing gra-

44
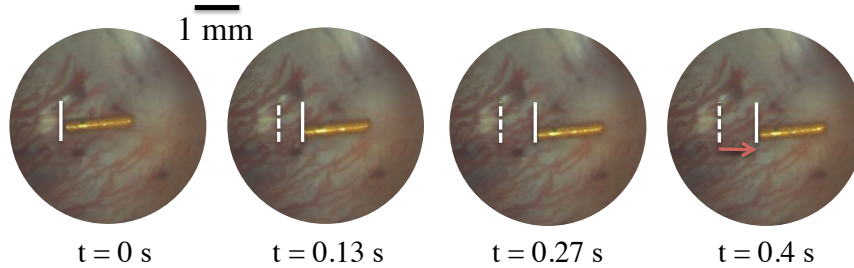
Figure 4.8: Microrobot inside the vitrectomised rabbit eye surrounded by BSS. A magnetic field gradient causes the microrobot to translate.

dient along the axis of robot orientation at constant field magnitude (20 mT). A general increase of translation due to increasing field gradient is observed. However, the translation of the microrobot in vitreous is less than 0.2 mm for a magnetic gradient that increases piecewise from 0 to 500 mT/m over 20 s. It is assumed that collagen fibre bundles that attach to the microrobot in vitreous cause the lack of translational movement. The interaction between the microrobot and collagen fibre bundles can be modelled as a mass-spring system. Figure 4.9(b) shows the response of a microrobot that is entangled in a collagen fibre bundle within lapine vitreous. Magnetic gradients between 0 and 300 mT/m are applied at a constant field magnitude of 30 mT. It is shown that the applied force is proportional to microrobot displacement. Thus, collagen fibre bundles show the behaviour of a linear spring.

Figure 4.10(a) illustrates the behaviour of the microrobot in BSS inside the living rabbit eye. The solid red line shows the position of the microrobot within the eye, whereas the green dashed line indicates the increasing field gradient. Similar to *in vivo* experiments in vitreous, the general trend shows increasing translation for increasing magnetic field gradients. The translation of the microrobot in BSS is an order of magnitude larger than in lapine vitreous with a maximum of 4 mm. As stated before, BSS is less viscous than vitreous, thus, allowing for better mobility of the microrobot. Furthermore, no collagen fibres are present in BSS in that the microrobot can entangle. However, due to the low
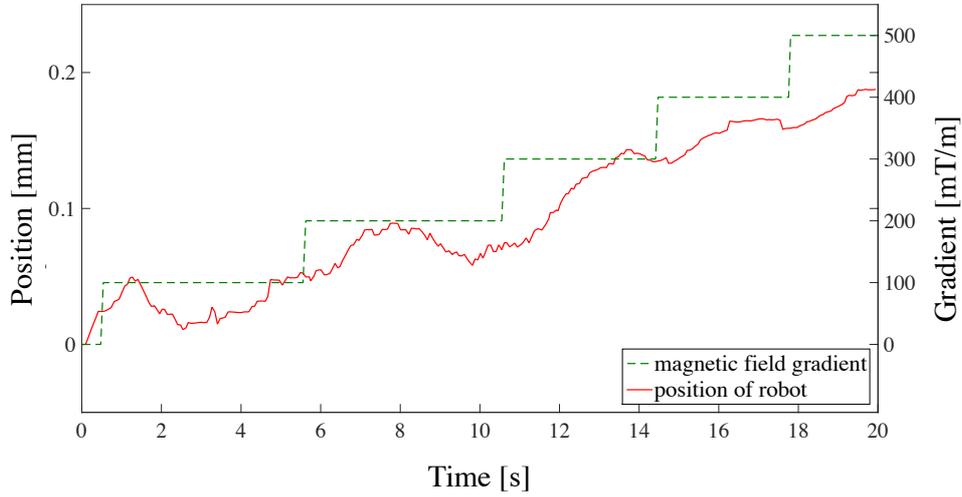
(a)
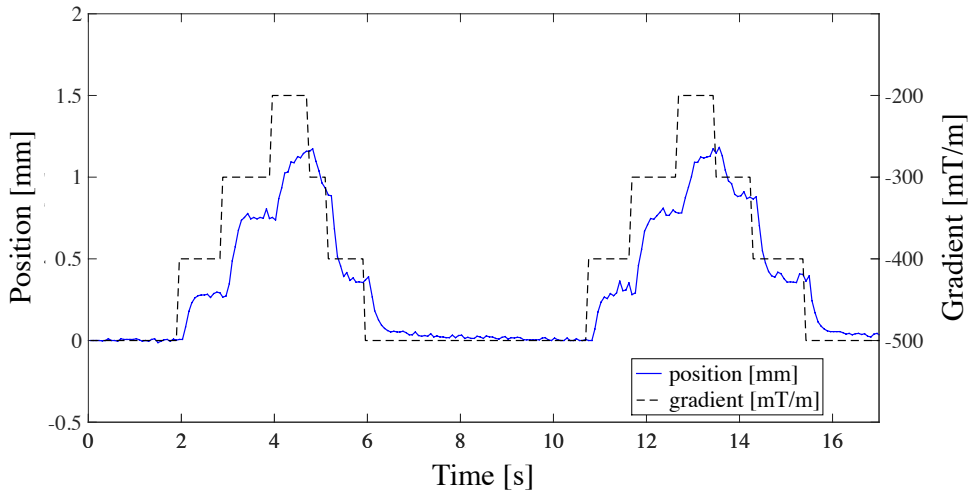
(b)

Figure 4.9: (a) Translation of intravitreal microdevice due to magnetic field gradient at a constant field of 20 mT in lapine vitreous. (b) Translational movement of intravitreal microrobot that is entangled in collagen fibre bundle at 30 mT. The applied magnetic gradient is directly proportional to the displacement of the microrobot. The microrobot that is attached to a collagen fibre bundle can be modelled as a spring-mass system.

viscosity of BSS, the microrobot sinks to the retina instead of floating within the central eye. When applying a magnetic field gradient, the microrobot sticks to the retina until a critical gradient is applied that generates a force, which is large enough to overcome friction. The black arrow in Fig. 4.10(a) indicates a characteristic stick-slip friction behaviour of the microdevice in BSS, which is further investigated in Appendix A. During *in vivo* experiments the device starts to translate at this critical field gradient (420 mT/m), as illustrated in the figure.

Figure 4.10(b) illustrates the microrobot response to various gradients at a constant field magnitude (20 mT) in porcine vitreous. It is observed, that an increasing field gradient results in an increased translation of the microrobot. Furthermore, a typical viscoelastic behaviour of the vitreous is observed. By applying a constant gradient, a constant force is exerted on the device. However, the translational movement of the microdevice shows a delayed creep response to the force input. At a field magnitude of 20 mT the maximum translation of the robot is measured to be 3.2 mm in porcine vitreous. The resulting maximal translational displacements of an intraocular microrobot in porcine vitreous as a result of changing field gradients are summarised in Table 4.1. The table shows that the translational displacement increases with increasing magnetic gradient, as well as increasing field magnitude. However, the gradient generally has a larger influence on the translational behaviour of the intravitreal microdevice.

When comparing results from the *in vivo* experiments in lapine vitreous with those from *ex vivo* experiments in porcine vitreous, it is observed that translational displacement of the intravitreal microdevice is approximately one order of magnitude larger in porcine vitreous. This behaviour may be due to species specific variations of the vitreous structure or due to *post mortem* liquefaction of the vitreous in the porcine eyes. Furthermore, none of the rabbit eyes under observation showed immediate inflammation during the experiments or upon removal of the microrobot.
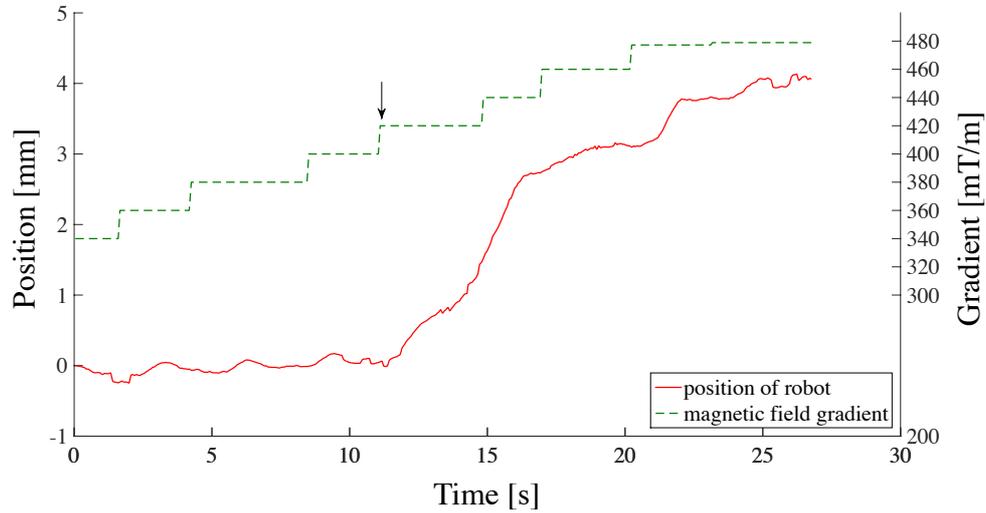
(a)
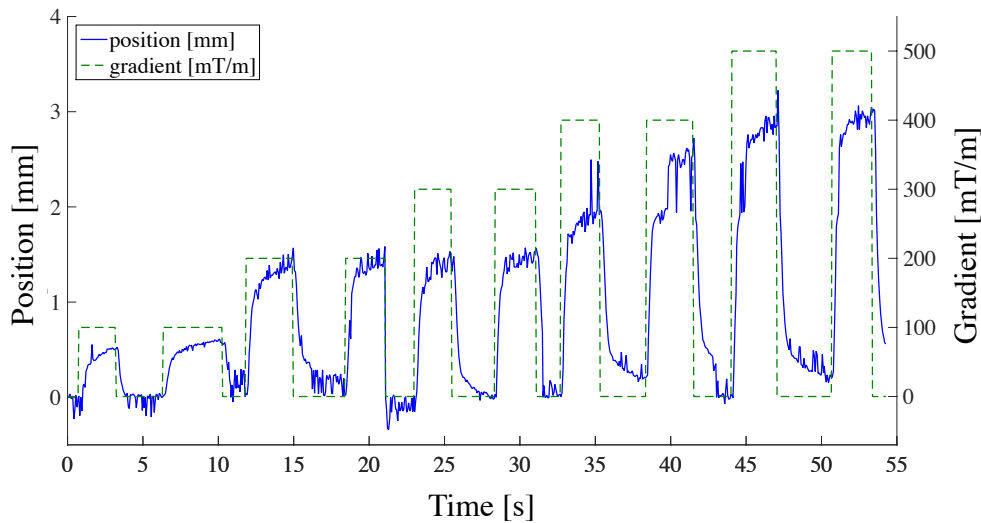
(b)

Figure 4.10: (a) Translation of microdevice due to magnetic field gradient at a constant field of 30 mT in BSS inside the vitrectomised lapine eye (*in vivo*); the critical gradient is indicated by the *black arrow*. (b) Translation of intravitreal microdevice due to magnetic field gradient at a constant field of 20 mT in porcine vitreous (*ex vivo*).

Table 4.1: Maximal translational displacement in mm due to magnetic gradient [mT/m] at constant field magnitude [mT] in porcine vitreous (*ex vivo*)

| Field Magnitude [mT]	Gradient [mT/m]				
	100	**200**	**300**	**400**	**500**
10	0.2	0.6	1.1	1.4	1.7
20	0.5	1.6	1.5	2.7	3.2
30	1.1	1.5	2.4	3.0	3.0
40	1.3	2.2	2.4	-	-

4.3   Helical Microrobots for Ophthalmic Applications

When a cylindrical microrobot is inside a magnetic field gradient, it is subject to translation along the gradient. However, experiments (Section 4.2.3.3) have shown that inside vitreous humour the microdevice gets entangled in collagen fibre bundles and, thus, translational motion is hindered. Increasing the magnetic volume could increase the magnetic force, potentially overcoming the forces applied by the fibres in the vitreous. To do this, the size of the microrobot needs to be increased, rendering it more invasive. A different solution to enhanced translational movement through the vitreous is by changing the microrobot's shape, and thus, its type of propulsion. This section focuses on the exploration of helical microstructures for movement through the fibrous structure of the vitreous humour.

4.3.1   Helical Microrobot in Fibrous Environments

Magnetic helical microrobots, powered by external rotating magnetic fields, were first presented by Bell et al. in 2007 [82] and further characterised by Zhang et al. and Peyer et al. [50–52]. These helical swimmers are inspired by the corkscrew motion of bacteria flagella, such as *Escherichia coli* or *Borrelia burgdorferi*. They can perform 3D navigation in various liquids under low-strength rotating magnetic fields (<10 mT). Recent results have shown that they can be used for single-cell targeted drug delivery *in vitro* [83–85] and can be wirelessly actuated *in vivo* [86]. Resistive-force theory (RFT) of flagellar

propulsion is commonly used for hydrodynamic analysis of swimming flagella and was originally proposed by Gray and Hancock [87, 88]. The theory was first applied to flagellated bacteria [89], predicting a decrease in swimming velocity with increasing viscosity of the environment. However, the flow field created by a helical swimmer in a viscoelastic medium is described by a complex and highly nonlinear system. Many parameters influence the flow field, such as additional polymeric stresses created by the flow field, the response of the flow field to the polymeric stresses, and the interaction of solvent and polymeric forces with the helix [90]. Berg and Turner have shown that helically shaped bacteria, such as *Leptospira* or *Escherichia coli*, can exploit the fibre structures inside a viscoelastic fluid and swim more rapidly in methylcellulose than in nonviscoelastic solutions. The higher swimming efficiency is due to the fibre network exerting forces normal to a segment of the helix and the helical organism can *push* itself forward, increasing the effective pitch of the helical motion [91]. These bacteria are small enough to swim through the empty spaces of a structured fibre network and thus, feel the microscopic viscosity of the solvent rather than the macroscopic viscosity of the solution. Magariyama and Kudo derived a model based on RFT to explain the increased swimming velocity of helices in fibrous environments. The model suggests that the fibre network forms a virtual tube around the thin-filament of the bacterium and allows it to enhance propulsion in the tube resulting in movement that is similar to corkscrew motion in solid matter without slippage [92]. However, the model assumes that the thickness of the filament is smaller than the space between the fibres in the network. Leshansky proposes a model that assumes sparsely distributed spherical particles instead of fibres in the fluid. The model suggests an increasing effective pitch of the helical swimmer due to the particles in the fluid without restrictions on filament thickness [93].

Many research efforts have experimentally confirmed the mathematical models of increased propulsion efficiency with increasing viscoelasticity. Liu et al. [94] studied the force-free swimming speed of a rotating helix in viscoelastic Boger fluid and conclude that swimming speed can decrease or increase as a

function of the geometry of the swimming waveform and the Deborah number, which characterises the fluidity of the surrounding solution. A numerical study of helical swimming in an Oldroyd-B fluid model has shown that beyond a critical pitch angle of the helix with different filament sizes a range of Deborah numbers can be found for which swimming speed is higher than in a nonviscoelastic Newtonian fluid [90]. The increase of swimming velocity due to increased fibre concentration in a medium is explained mathematically due to boundary conditions at the structure-fluid interface by Fu et al. [95]. For a sparse fibre network, the helical swimmer does not exert force directly on the network. Instead forces are mediated through the solvent and network traction vanishes. In a dense fibre network, the swimmer is in direct contact with the fibres, causing stress in the network. Schamel et al. succeeded in propelling magnetically actuated nano-sized swimmers through a fibrous hyaluronan solution [96]. The proposed nanoscrew has a length of 400 nm and displays enhanced propulsion velocities in fibrous solutions, while it cannot swim in pure water due to Brownian motion.

4.3.2   Helical Microrobots in Vitreous Model

Most experimental studies focus on the swimming speed of real biological structures, thus generalisation of the results are limited due to variability and complexity of individual swimmers. However, theoretical explanations of the swimming behaviour of helical structures assume idealised models. Here, the swimming behaviour of magnetically actuated helical microswimmers is investigated in solutions with various collagen fibre concentrations as a model for the vitreous humour.

4.3.2.1   Helical Microrobot for Experimentation

The geometry of the helical microrobot is inspired by the helical tail of bacteria, such as *Escherichia coli* or *Borrelia burgdorferi*. The size and shape are determined by several parameters, namely the helical angle θ, the total length of the helical swimmer, and the geometry of the filament, as illustrated
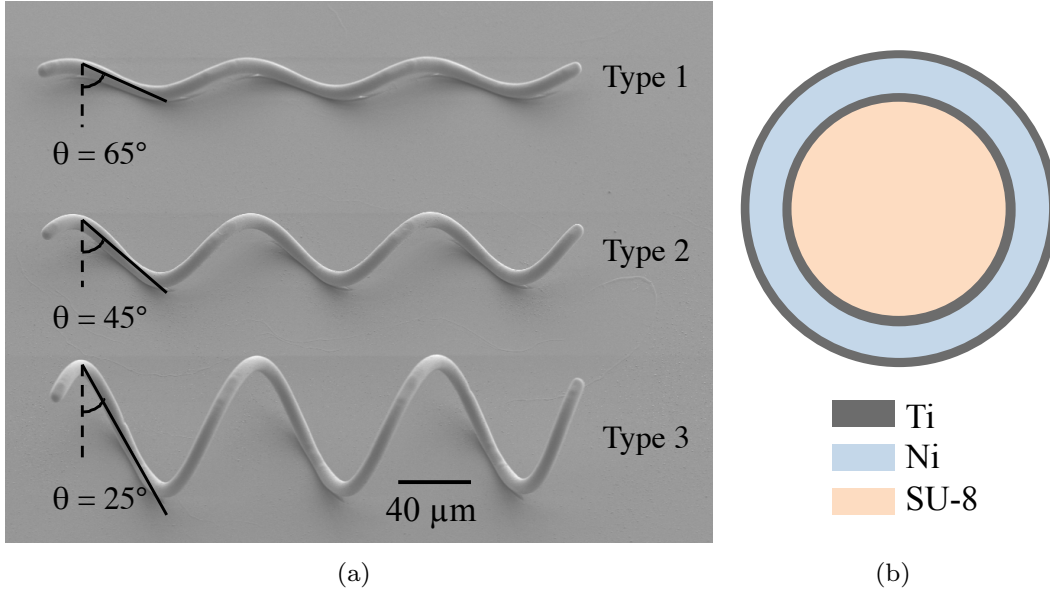
Figure 4.11: (a) Scanning electron microscope image of three types of helical microrobots with helical angles of 65°, 45° and 25°. All three types have a length of 280 μm. In this study, type 2 is utilised for all experiments. (Image courtesy of Famin Qiu) (b) Cross-section of a helical microrobot showing layers of Ti, Ni and SU-8.

in Fig. 4.11(a). The helical microrobots consist of a helical body made from SU-8 polymer and a nickel (Ni) and titanium (Ti) bilayer around the body, as depicted in Fig. 4.11(b). The movement of the helical microrobot is controlled by external rotating magnetic fields. As the uniform magnetic field rotates, thus applying a magnetic torque τ, the device is rotated about its helical axis. The forward motion of the helical structure is caused by the non-reciprocal corkscrew motion in a low Reynolds number regime. The maximum rotational speed of the device, or step-out frequency ω_{max}, depends on the applied magnetic torque τ_{max}, as in

$$\omega_{max} = \frac{a}{ac - b^2} \cdot \tau_{max}, \tag{4.1}$$

where a, b and c correspond to geometrical coefficients of the helical structure [97]. At its step-out frequency, the helical structure is no longer able to

follow the rotation of the field and slows down. The maximum velocity u_{max} depends on the step-out frequency as described by

$$u_{max} = -\frac{b}{a} \cdot \omega_{max} = \frac{b}{b^2 - ac} \cdot \tau_{max}. \tag{4.2}$$

For Newtonian fluids the velocity u_{max} is independent of the viscosity, whereas the fibres in a fibrous solution can change the drag on the helical structure in an inhomogeneous way. This can lead to different apparent viscosities in the coefficients a, b and c [92, 98].

4.3.2.2 Vitreous Model Preparation

To model the helical swimmer contact with vitreous humour, gelatine that consists of several types of collagen was used [99, 100]. Six aqueous solutions of gelatine with different concentrations (350, 502, 974, 1578 and 2480 µg/mL) were prepared to investigate the helical microrobot's swimming behaviour. Control solutions with pure deionised water (noted as 0 µg/mL gelatine) were also used for experiments. The gelatine solutions were left to stabilise at room temperature and swimming experiments were conducted between two and 24 hours after solution preparation. Viscosity and temperature measurements were performed both before and after every experiment session. Viscosity was measured using a viscometer (custom-made by Rheonics, Switzerland) and temperature was measured using a thermocouple.

4.3.2.3 Electromagnetic Setup

The helical microrobots were actuated by uniform rotating magnetic fields that were generated by a Helmholtz coil setup consisting of three orthogonal coil pairs (Fig. 4.12). The system creates a rotating magnetic field $\mathbf{B}$ and induces a torque $\mathbf{T}$ that acts to align the microrobot's magnetisation $\mathbf{M}$ with the magnetic field as in

$$\mathbf{T} = v \cdot \mathbf{M} \times \mathbf{B} \tag{4.3}$$

(a)   (b)
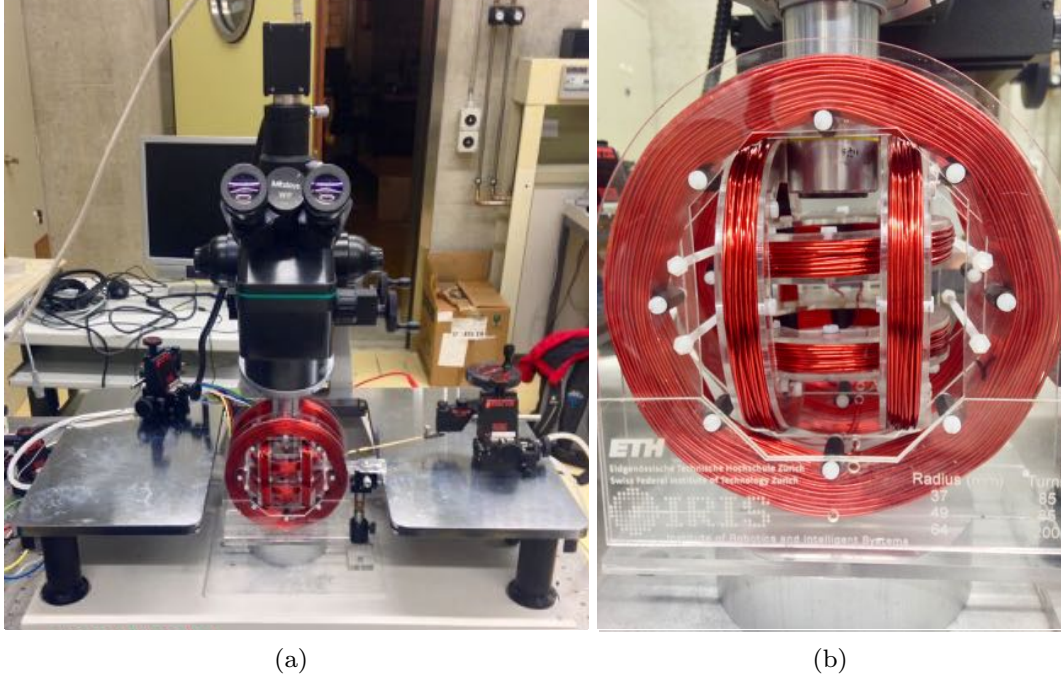
Figure 4.12: (a) Electromagnetic hardware setup for manipulation of helical microrobots, including (b) three Helmholtz coil pairs and a microscope and camera for observation of the workspace.

where v is the magnetic volume of the microrobot. The magnetic fields were controlled by a custom software and the movement of the helical swimmer was recorded with a camera through a microscope (Fig. 4.12).

4.3.2.4   Experimental Procedure

Prior to experimentation the wafer, which contains the fabricated helical structures, was cleaned thoroughly by first emerging it in acetone and then placing it in an ultrasonic bath for 5 min. This cleaning process was repeated with isopropyl alcohol and deionised water. For experimentation the fabrication wafer was placed in a container that was filled with the gelatine solution and then placed in the central workspace of the electromagnetic system. A manually controlled tungsten tip was used to transfer a helical swimmer from the fabrication wafer to the swimming area where it was submerged in the gela-

Table 4.2: Viscosity measurements of the various gelatine solutions pre and post the experimental procedure at 24 °C.

Concentration	pre (Pas)	post (Pas)
0 μg/mL	1.000	1.000
350 μg/mL	1.016	1.018
502 μg/mL	1.022	1.005
974 μg/mL	1.081	1.090
1578 μg/mL	1.102	1.130
2480 μg/mL	1.130	1.147

tine solution. The helical swimmer was moved by incrementally increasing the rotation frequency of the rotating magnetic field. Images of the motion and corresponding field strengths and rotational frequencies were recorded for post-processing. During post-analysis a MATLAB program tracks the swimmer on the recorded images and allows for the analysis of forward and drift velocities of a swimmer.

4.3.3   Experimental Results and their Implications

The viscosity and temperature of each gelatine solution are measured before and after the experimental procedure. All measured temperatures are 24 °C. Table 4.2 summarises the results for viscosity measurements for various collagen fibre concentrations.

The forward velocity of each helical structure is measured and plotted against the corresponding rotational frequency of the magnetic field. The magnetic field strength and collagen concentration are reported for each sample. An example plot is shown in Fig.4.13. The figure shows three velocity measurements, executed with three different helical structures actuated in water with a magnetic field strength of 3 mT. The mean and standard deviation of the forward velocities are calculated at each measured frequency. The region, labelled A on the plot, shows a gradual increase of the structure's forward velocity with increasing rotational frequency until the step-out frequency is reached at point B, where a large drop of the forward velocities is recorded (labelled C).
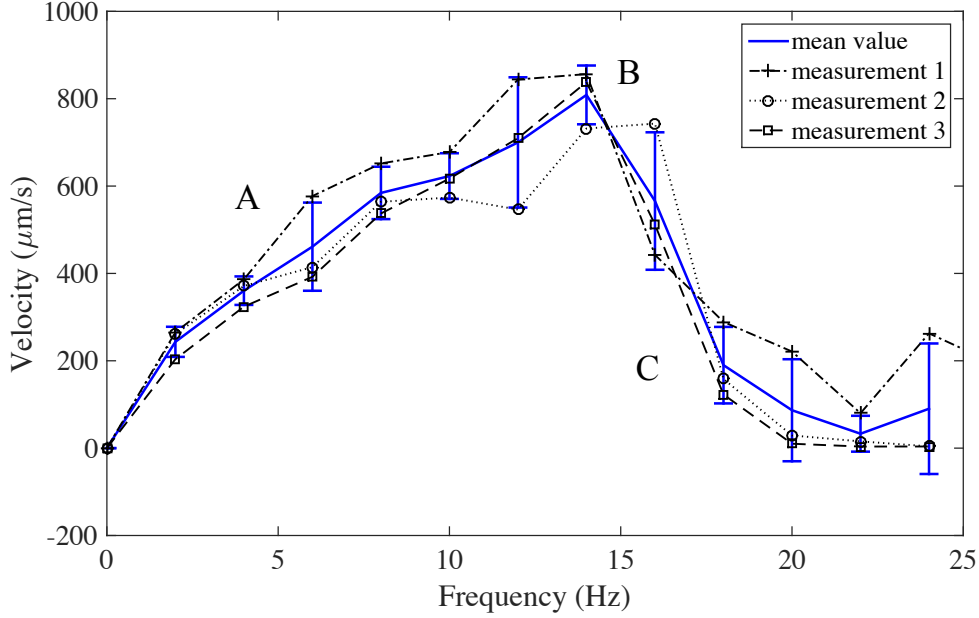
Figure 4.13: Measured velocity of helical swimmer measured at various frequencies of the rotational magnetic field at magnetic field strength of 3 mT in water.

Figure 4.14 illustrates the mean measured forward velocity at various frequencies of the rotating magnetic field with a magnitude of 9 mT for helical swimmers actuated in different gelatine concentrations. The maximum forward velocities are measured and plotted against gelatine concentration for magnetic field strengths of 3, 6 and 9 mT in Fig. 4.15. The average maximum velocities of measured helical structures in various concentrated gelatine solutions are summarised in Table 4.3 for the three magnetic field strengths. The corresponding step-out frequencies are summarised in Table 4.4.

As described in Equations 4.1 and 4.2, it is observed that maximum velocity and step-out frequency positively correlate with increasing magnitude of the external rotating magnetic field, due to increasing magnetic torques. Viscosity measurements before and after experiments (Table 4.2) show a slight
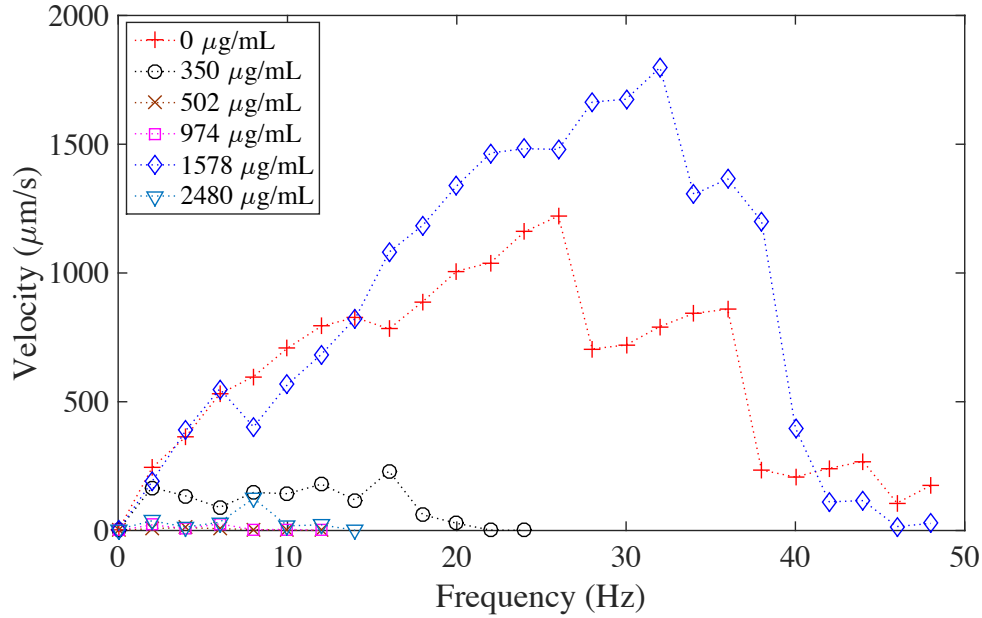
Figure 4.14: Mean maximum velocities, measured at magnetic field strength of 9 mT and various gelatine concentrations.

increase in macroscopic viscosity of the solutions. Presumably, gelation continues during the experimental process, but the measured increase is negligible.

Results suggest that it becomes more difficult for the helical structures to move in fibrous media compared to pure water as the maximum velocity and step-out frequency decrease. The structures swim freely in a solution with collagen fibre concentration of 0 µg/mL (pure water) and performance quickly declines after introduction of collagen fibres to the solution. A performance peak is observed for helical swimmers in a gelatine solution with a concentration of 1578 µg/mL for all measured magnetic field magnitudes. The most notable performance peak occurs at 9 mT where the measured maximum velocity is similar to that in water. If collagen fibre concentration is increased further, performance drops and the helical microrobot's movement becomes essentially zero.
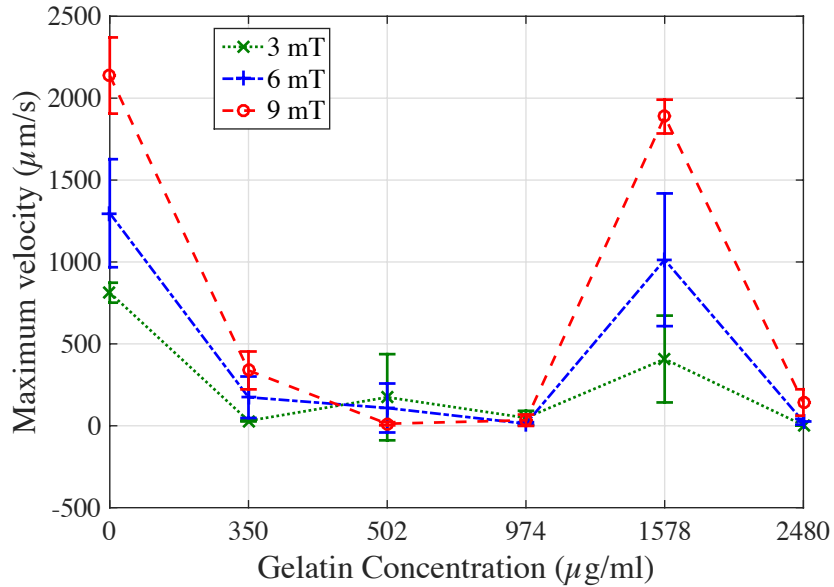
Figure 4.15: Mean and standard deviation of measured maximum velocities of helical swimmers in various gelatine concentrations and with magnetic field strengths of 3, 6 and 9 mT.

The enhanced swimming performance of the helical microrobot at gelatine concentration of 1578 µg/mL is illustrated in Fig 4.14. These findings corresponds to the experimental evidence of increased swimming speed of bacteria in fibrous environments observed by Berg and Turner [91]. Our observations are also in agreement with the mathematical model of Magariyama et al. [92] that describes increased swimming efficiency in fibrous fluids. Concluding, an optimal shape may exist for the helical microdevice to efficiently swim through a fibrous environment, such as the vitreous humour.

4.4 Floater Removal using Magnetic Microrobots

Intravitreal microrobots have been suggested for targeted drug delivery but can also be applied as tools during mechanical interventions inside the eye. One possible application for intravitreal microrobots is the mechanical removal of vitreous floaters from the posterior eye.

Table 4.3: Average maximum swimming velocities, measured at different magnetic field strengths and various gelatine concentrations.

Concentration	3 mT	6 mT	9 mT
0 µg/mL	812.5 µm/s	1297.6 µm/s	2138.2 µm/s
350 µg/mL	30.1 µm/s	174.1 µm/s	337.9 µm/s
502 µg/mL	174.2 µm/s	108.6 µm/s	12.5 µm/s
974 µg/mL	48.4 µm/s	12.7 µm/s	33.8 µm/s
1578 µg/mL	407.5 µm/s	1013.4 µm/s	1887.6 µm/s
2480 µg/mL	3.3 µm/s	24.6 µm/s	142.1 µm/s

Table 4.4: Average step-out frequencies, measured at different magnetic field strengths and various gelatine concentrations.

Concentration	3 mT	6 mT	9 mT
0 µg/mL	14 Hz	22 Hz	26 Hz
350 µg/mL	2 Hz	4 Hz	16 Hz
502 µg/mL	2 Hz	4 Hz	4 Hz
974 µg/mL	2 Hz	2 Hz	6 Hz
1578 µg/mL	14 Hz	16 Hz	32 Hz
2480 µg/mL	8 Hz	10 Hz	8 Hz

4.4.1   Vitreous Floaters

A common event occurring in the vitreous is posterior vitreous detachment (PVD) due to the liquefaction of vitreous humour and the destabilisation of collagen fibrils, both related to ageing. In combination with rotational eye movement, this destabilisation of the collagen network causes a collapse of the vitreous body, resulting in floating collagen fibrils, so called vitreous floaters [101]. They can obstruct the field of view by casting a shadow on the retina. Vitreous floaters are a condition considered benign by ophthalmic surgeons, but can cause psychological distress, such as fear, depression, or anxiety, in some patients [102]. Conventional treatment of floaters requires education of patients. Tsai et al. [102] reported the "off-label" treatment of vitreous floaters using a yttrium aluminum garnet (YAG) laser, but no clinically relevant conclusions about the effectiveness of laser treatment for vitreous floaters can be drawn

from this study [101]. Another study even reported worsening of the condition after laser treatment [103]. Risk from laser treatment arises due to the vitreous floater being in motion during treatment, making focusing difficult. Vitrectomy has been described as a surgical treatment for vitreous floaters but is associated with several risks, which might be unacceptable for patients and surgeons.

4.4.2   Model for Floaters

Several types of vitreous floaters have been identified [104]. The Weiss ring, also known as Martegiani ring, is a large ring-shaped floater that is caused by PVD. Diffuse floaters are cloud-like floaters and are caused by the natural ageing process. Fibrous strand floaters are thin, dense floaters that can appear as dots or string-like cobwebs. They are more prominent in young people and result from clumping collagen fibres in the vitreous.

Due to the variety of floaters occurring in patients' eyes, two models for vitreous floaters are developed in this work. The cubic floater model represents large floaters and allows for the analysis of the carrying capacity of a magnetic microrobot for floater removal. The fibrous floater model represents thin and fibre-like floaters with different shapes, such as a long string or a ring. Both floater models are produced from gelatine. Gelatine is a biopolymer derived from natural collagen and mainly consist of collagen types I, II, and III, while 75% of collagens in the vitreous are of type II.

4.4.2.1   Cubic Floater Model

To model large and dense vitreous floaters, 4 g of dry gelatine (Type A, Sigma-Aldrich, USA) was mixed with 40 mL of deionised water. The solution was heated to 60° and stirred for 20 minutes while maintaining the temperature. The solution was placed in the refrigerator for 3 hours and left to stabilise at room temperature for 45 minutes. Subsequently, the gelatine was cut into cubes with side length of 3 to 4 mm. The gelatine cubes are shown in Fig. 4.16(a).
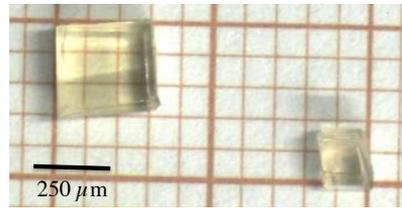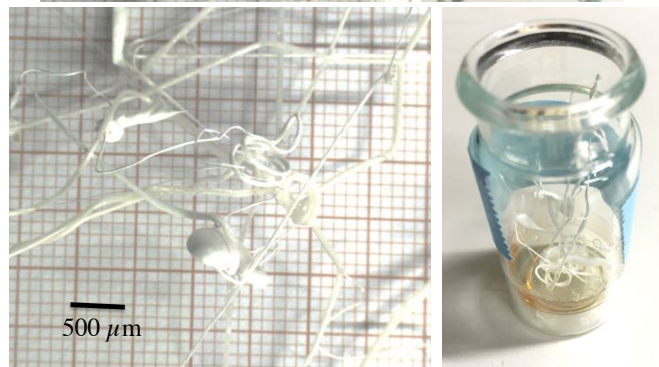
(b)

Figure 4.16: (a) Gelatine model of large and dense vitreous floater. (b) Wet spun gelatine model of fibrous vitreous floaters.

4.4.2.2   Fibrous Floater Model

To model fibrous vitreous floaters, dry gelatine (10 wt%) was mixed with 2-propanol (50 wt%) and deionised water (40 wt%) and tempered at 50° for 1 hour and repeatedly shaken by hand as described by Stoessel et al. [105, 106]. The addition of the organic solvent 2-propanol to the heated gelatine solution causes phase separation. Thus, the protein precipitates and can subsequently be decanted and wet spun into continuous gelatine fibres, as depicted in Fig. 4.16(b).

4.4.3   Microrobot for Removal of Floaters

A wireless magnetic microrobot was designed, which consists of a permanent cylindrical magnet (BJA Magnetics, USA) with diameter of 300 µm attached to the tip of a small brass hook (Tiemco 518, size 32), as illustrated in Fig. 4.17.
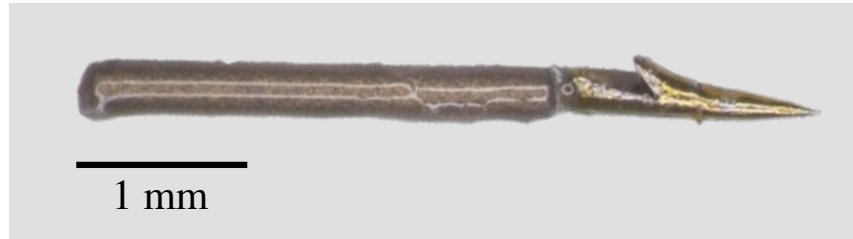
Figure 4.17: Magnetic microrobot for floater removal consisting of a permanent cylindrical magnet and a hook.

The total length of the microrobot is approximately $3\,\mathrm{mm}$, but may be reduced in future designs.

4.4.4   Floater Manipulation and Removal

In a first experiment, a cubic model floater was submerged in silicone oil (Wacker Chemie AG, Germany, viscosity $1000\,\mathrm{mPas}$ at $25°$) in a plastic container and placed in the central workspace of the magnetic manipulation system OctoMag (Section 3.2). To understand the load capabilities of the proposed microrobot, the floater model was moved and manipulated with the magnetically controlled microrobot. The volume of the dense model floater was determined as approximately $43\,\mathrm{mm}^3$. The large model floater could easily be manipulated by the magnetic microrobot.

A second experiment was executed to demonstrate manipulation and removal of fibrous floaters from the eye. For this, up to three fibrous floater models were submerged in silicone oil (viscosity $1000\,\mathrm{mPas}$ at $25°$) inside a small plastic container. The magnetic microrobot was guided to the floater model by manual manipulation of the OctoMag system with a 3D space mouse or using visual servoeing. As shown in Fig. 4.18, the microrobot was used to approach and catch a fibrous floater with its hook. The floater then was manipulated towards a trocar, through which an injection needle was inserted to remove the floater from the plastic container.
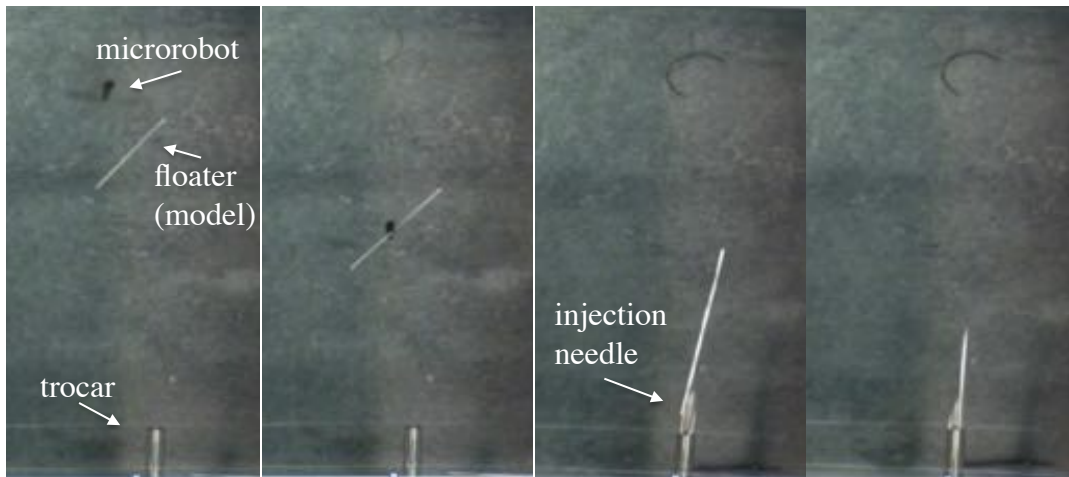
Figure 4.18: A magnetic microrobot approaches, catches vitreous floater, and moves it towards an injection needle for floater removal.
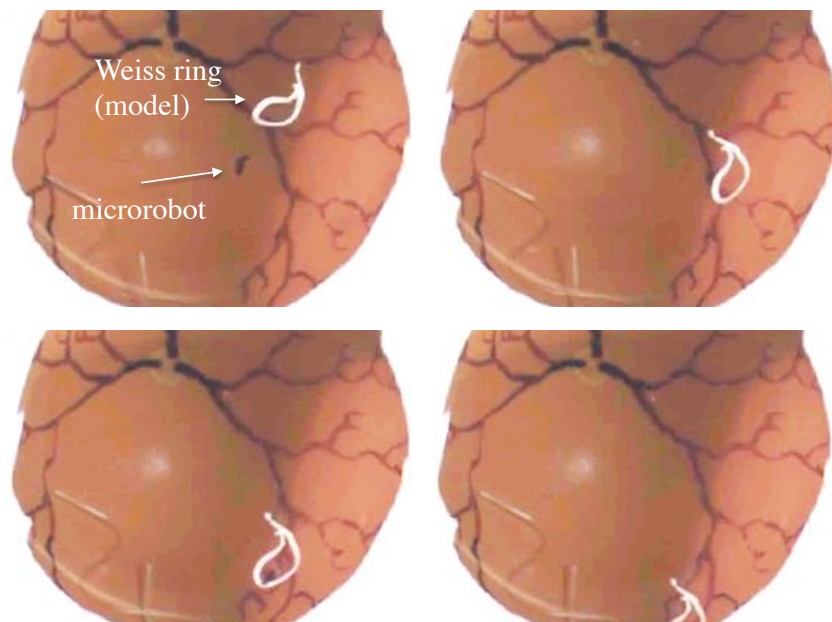
Figure 4.19: Manipulation of a Weiss ring (model floater) using a magnetic microrobot. The microrobot approaches the Weiss ring, catches it, and moves it to the side of the eye phantom.

Figure 4.19 shows a microrobot approaching a Weiss ring floater model inside silicone oil (viscosity $1000\,\mathrm{mPas}$ at $25°$) in an eye phantom. The microrobot captures the floater with its brass hook and subsequently manipulates the Weiss ring model floater out of the field-of-view and towards the eye model edge.

4.5   Retraction of Wireless Microrobots

After injection of an intravitreal microrobot and successful manipulation inside the vitreous, the microdevice must be retracted from the eye. For this, a customised retraction tool was designed, fabricated and tested in cadaver porcine eyes. The retracting mechanism is manufactured from a standard syringe with an attached 23 G injection needle. The size of the needle is the same as that used for injection, such that the same channel in the sclera can be used for injection and retraction of the microrobot. A wire with a small attached permanent magnet (BJA Magnetics, USA) is inserted into the needle and attached to the plunger, such that the magnetic tip of the wire can be moved in and out of the injection needle. The magnet at the tip of the wire attracts the microrobot if a low magnetic field is applied that also orients the device. Subsequently, the microrobot can be pulled into the needle and removed from the eye. The removal of an intraocular microrobot and the customised retraction tool are illustrated in Fig. 4.20. A full retraction sequence during experiments in *ex vivo* porcine eyes is demonstrated in Fig. 4.20(c). Experiments show that microrobots can be removed in a controllable and minimally invasive manner, potentially avoiding a vitrectomy, and, thus, making ophthalmic surgical interventions accessible to a larger set of ophthalmic surgeons and more acceptable to patients.

4.6   Conclusion

This chapter demonstrates the general feasibility of controlling the movement of a wireless microdevice inside the eye. The microrobot can be injected into the vitreous cavity, filled with vitreous, silicone oil, or balanced salt solution,

and can be magnetically controlled during *in vivo* and *ex vivo* experiments. Rotational as well as translational mobility of a cylindrical device have been explored through experiments. While the microrobot demonstrated good rotational controllability, it can get caught in bundles of collagen fibres during translation due to the viscoelastic behaviour of the vitreous humour.

To counter the problem of microrobot translation inside the vitreous humour, a magnetic microdevice was designed that exhibits a helical shape. Several studies have suggested that a helical object's swimming speed can be enhanced by the presence of fibres in the surrounding medium. In this chapter, the forward swimming speed of a helically shaped microrobot was evaluated in solutions with different collagen fibre concentrations. A performance peak was observed, suggesting that an optimal relationship exists between the shape of the microdevice and the surrounding fibrous medium.

For future purposes the microrobot can be microfabricated with specific designs. The size as well as the shape of the microrobot can be adjusted to the task. For slow release targeted drug delivery the microrobot features a drug reservoir, whereas mechanical components, such as needles or hooks, are attached for mechanical applications. The microrobot dimensions are only restricted by the inner diameter of a 23 G needle, which is used for sutureless injection through the *pars plana* region of the sclera into the eye. A possible application of wireless intraocular microrobots is the removal of vitreous floaters from the eye. A magnetic device has been designed and fabricated and was used to demonstrate floater removal. The electromagnetic control system, OctoMag, allows for precise control of the microrobot in 3D by generation of an oriented magnetic field and gradient. The risk of ophthalmic surgery can potentially be reduced to a minimum with the assistance of minimally invasive microrobots. As the microrobot can be injected into the eye, steered and removed from the vitreous cavity by a surgeon, this technology potentially offers the possibility to assist in minimally invasive ophthalmic treatments.
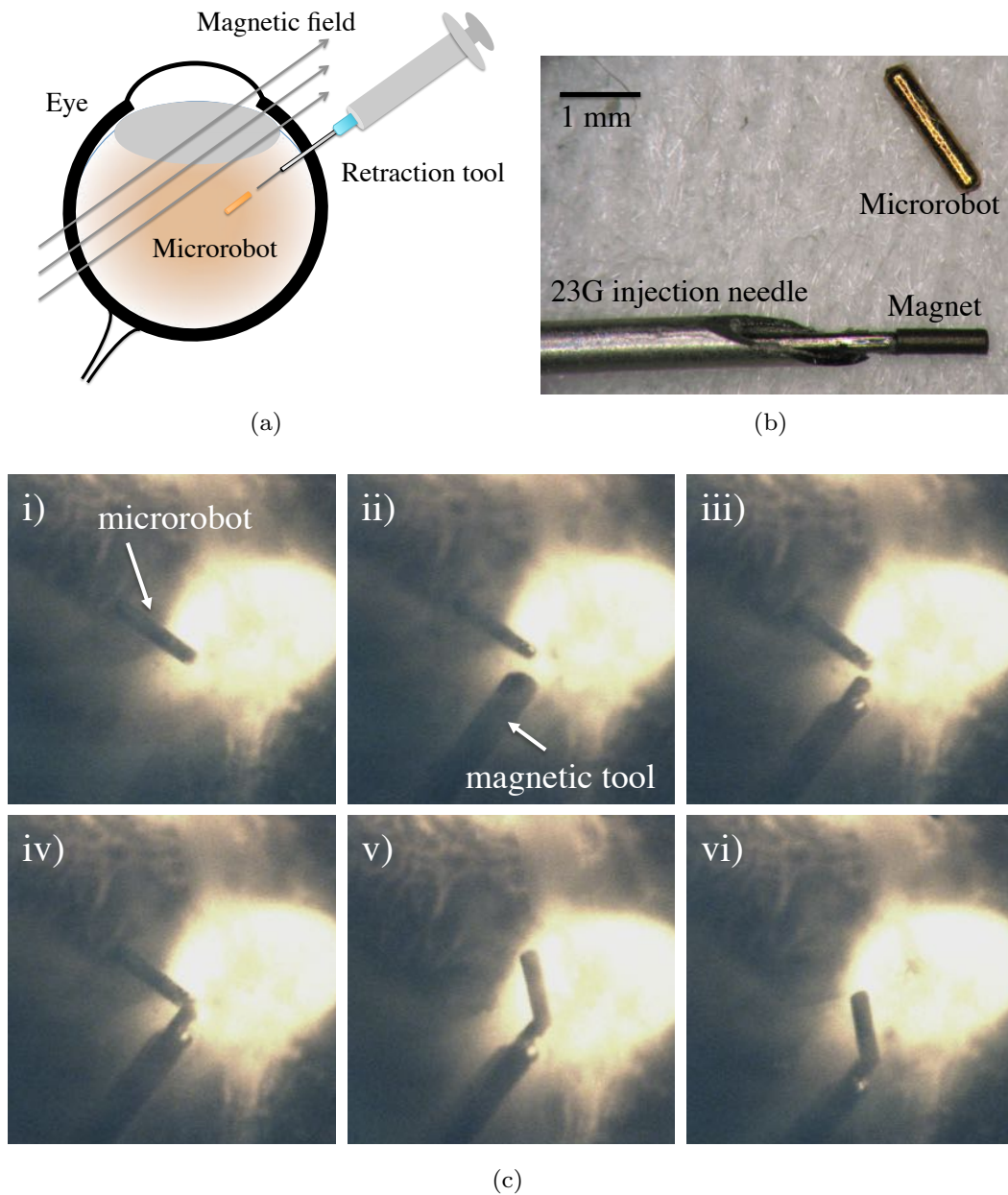
Figure 4.20: (a) Strategy for removal of an intravitreal microrobot from the eye. (b) Removal of intravitreal microrobot using a customized magnetic tool. (c) Retraction sequence during *ex vivo* experiments in porcine eyes. (i) The intravitreal microrobot attaches to (ii-iv) the magnetic tip of the customized magnetic tool and (v-vi) is pulled into the needle and out of the eye.

Chapter 5

Magnetic-Mechanical Actuation System for Capsulorhexis

This chapter characterises the forces required to perforate the anterior lens capsule during capsulorhexis [107] and presents a hybrid magnetic-mechanical manipulation system for automated capsulorhexis [108] utilising a flexible catheter with a custom diathermy tool for thermal cutting. Vision and encoder based closed loop control is implemented to guide the tip on a predefined path. A continuous motion with high repeatability and accuracy is achieved and thermal cutting of an *ex vivo* porcine anterior lens capsule is demonstrated.

The development of the initial prototype for a hybrid mechanical-magnetic actuation system for a flexible tool was supported by Simone Schürle and advised by Roel Pieters. Motion control and design of the diathermy tip was developed in collaboration with Vasileios Chatzopoulos and Jonas Lussi during their Mastertheses. Additionally, experiments to determine lens puncture forces were executed by Jonas Lussi during his Semesterthesis and advised by Dimitrios Felekis and Andrew Petruska. Medical advisers throughout this project were Stephan Michels and Avraham Dishy.

5.1 Capsulorhexis

Cataracts are the leading cause of blindness and account for 51% of world visual disability [11]. During cataract surgery a corneal incision is made at the limbus to allow for insertion of a sharp pointed instrument (a capsulorhexis needle or cystotome) into the aqueous anterior chamber of the eye, which previously has been filled with a viscous gel for anterior chamber stability. The instrument
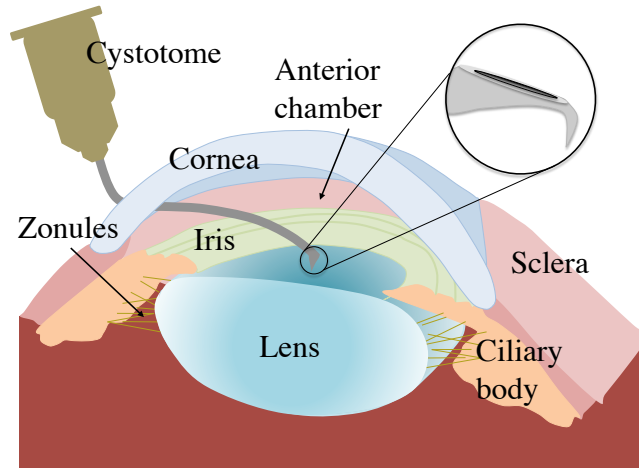
Figure 5.1: During capsulotomy, the cystotome is inserted into the anterior chamber of the eye at the limbus. After rotating, its tip points towards the lens. By applying a posteriorly directed force, the lens capsule is perforated [13].

tip is placed over the centre of the anterior capsule and pushed posteriorly to perforate the lens capsule [13], as illustrated in Fig. 5.1. This procedure is followed by the opening of the lens capsule, a process called capsulorhexis (Fig. 5.2). Subsequently, the lens cortex, nucleus, and epinucleus are removed and an artificial intraocular lens (IOL) is inserted into the capsular bag. An essential step of capsulorhexis is the initial perforation of the anterior lens capsule with a sharp tip instrument, a procedure called anterior capsulotomy.

The size, shape and location of the opening in the anterior lens capsule are crucial. No tears should occur in the lens capsule during or after surgery as it could prevent implanting the IOL in the capsular bag [13]. It has been shown that posterior capsular opacification (PCO) can be prevented by opening the anterior lens capsule circularly in the centre of the lens with a diameter between 5 mm and 7 mm, so that the anterior lens capsule can overlap with the IOL optic surface and stabilise it [109, 110]. The ideal capsulorhexis edge should be continuous to allow for highest strength [13] and has been suggested to overlap with the IOL optics by 0.5 mm [111]. Achieving an intact, centrally located, and perfectly circular capsulorhexis is crucial to the safety and best outcome of
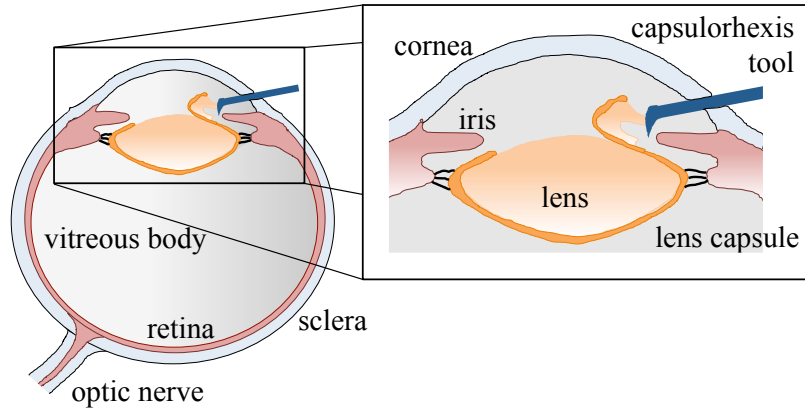
Figure 5.2: The basic anatomy of the human eye and a more detailed view of the anterior section of the eye. Capsulorhexis is one of the key steps in cataract surgery and describes the process of creating a circular hole in the lens capsule.

cataract surgery. This surgery requires high precision and is technically difficult to learn as the delicate structures of the anterior eye are under constant risk of damage due to the rigid instruments used by the ophthalmologist and a lack of precision arising from the limits of human force perception [17, 18].

5.2   Perforation Forces of the Anterior Lens Capsule

To understand the perforation force required for capsulotomy, a micro-mechanical characterisation method was developed to measure lens perforation forces on an intact porcine lens capsule using highly localised positioning and high-resolution force sensing methodology. This allows for the investigation of the mechanical behaviour of the anterior lens capsule during the surgical procedure and to understand specifications for the development of assistive tools for cataract surgery.

5.2.1   Mechanical Characterisation Method

Porcine eyes have been suggested as a conservative model for capsulotomy in human eyes due to a similar anatomical structure [112–114]. The porcine anterior lens capsule has a thickness of approximately $50 - 66\,\mu\mathrm{m}$ [115] and,

69

thus, is thicker than the human anterior capsule. Capsulorhexis is a procedure that is usually done on eyes with cataracts and, therefore, hardened lenses.

5.2.1.1 Experimental Setup

The experimental indentation system is shown in Fig. 5.3 and consists of a commercially available capacitive micro-electric-mechanical (MEMS) force sensor (FT-S100000, FemtoTools GmbH) that is mounted to a linear cartesian positioner with three degrees of freedom (DoF), which are moved by piezoelectric stepping actuators (SLC-2040, SmarAct GmbH) with a scanning range of 26 mm. The MEMS force sensor can resolve forces to $5\,\mu N$ ($1\,\sigma$ at $10\,Hz$) over a range of $\pm 100\,mN$. The sensor signal is an analog voltage, which is mapped to indentation force F using the calibration parameters provided by the manufacturer. To be in close proximity to the real surgical procedure, a parabolically shaped needle was chosen for this study. Three force sensors were used during several sets of experiments. Each force sensor was assigned a different needle diameter (200, 250, and $300\,\mu m$), that are equivalent to 33, 31, and 30 gauge medical needles. Figure 5.4 shows scanning electron microscope (SEM) images of the needle tips. The radii of the needle tips were measured visually from the SEM images to be 1.5, 2.25, and $3\,\mu m$, respectively. The 3-DoF positioner uses piezoelectric linear actuators and optical position encoders to provide a $26 \times 26 \times 26\,mm^3$ workspace with a positioning accuracy of $50\,nm$. The experimental system is controlled with a custom application in LabVIEW that allows automated control of tasks, data logging, and enables the user to set various parameters such as indentation speed and a maximum applied force value. The setup allows the indentation process to be monitored with a standard inverted light microscope.

5.2.1.2 Specimen Preparation

Porcine eyes were obtained from a municipal abattoir on the same day as the experiments and were stored in iced water. Prior to experimentation the eye was cut open at the limbus to carefully extract the lens and visually examined
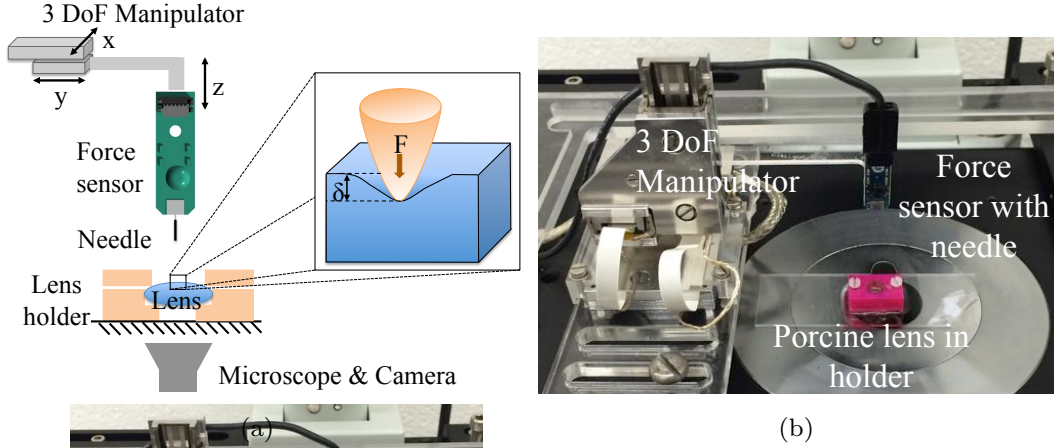
Figure 5.3: (a) The experimental system consists of a capacitive force sensor that is positioned in x, y, z-positions by a cartesian manipulator. A sharp tip needle is attached to the tip of the sensor. The needle exerts a force F on the lens material. The indentation depth is δ. (b) The actual experimental system including the 3-DoF manipulator, force sensor with needle, and a porcine lens in a polymer holder.

for damage. The lens was then transferred to a customised 3D-printed lens holder that was designed to fit the asymmetric lens shape described in [116]. The porcine lens was placed with its anterior side up and covered with a drop of silicone oil with kinematic viscosity of $350\,\mathrm{mm^2/s}$ to prevent drying and hardening. Subsequently, a 3D-printed ring was placed on top of the lens to constrain lateral movement during measurements.

5.2.1.3 Mechanical Testing Procedure

A total of 84 porcine anterior lenses were perforated and the indentation-force relationship was recorded. All experiments were done on lenses four to ten hours *post mortem* and at room temperature. Two studies were performed to investigate the perforation forces of the intact anterior lens capsule during perforation with a sharp tip instrument. The first study (*needle-size study*) investigates the influence of needle diameter on the perforation force while maintaining constant indentation speed. Three needles with diameters $d_{ind} = 200$,
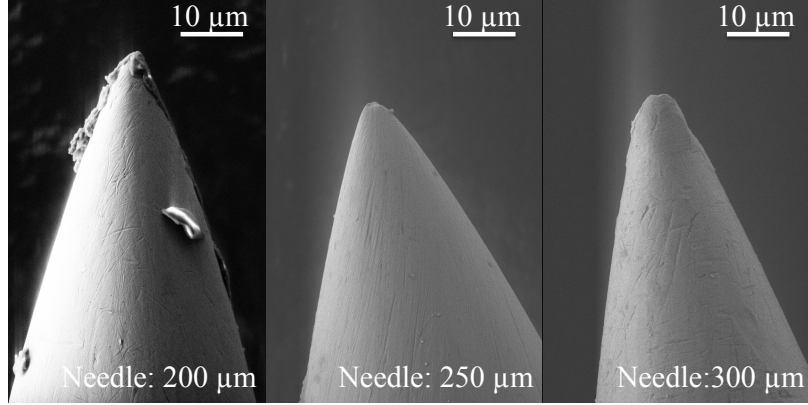
Figure 5.4: SEM images of sharp needle tips. The needle diameters are 200, 250, and 300 μm with tip radii 1.5, 2.25, and 3 μm, respectively.

Table 5.1: Number of experiments for each needle size on experimentation days 1 to 4.

d_{ind} [μm]	day 1	day 2	day 3	day 4
200	15	10	-	-
250	-	15	14	-
300	-	-	8	22

250, and 300 μm are used to perforate the lens capsule at an indentation speed of $v_{ind} = 8.55 \pm 0.09$ μm/s. Experiments were performed on four different days. The number of measurements are summarised for each needle size in Table 5.1. The second study (*needle-speed study*) examined the dependence of perforation forces on the speed of indentation by indenting at various speeds $v_{ind} = 8.57 \pm 0.02$, 32.38 ± 1.41, and 70.35 ± 9.91 μm/s, respectively, using a needle with diameter 300 μm.

During the first step of the experimental procedure the 3-DoF manipulator was used to position the MEMS force sensor with the attached needle above the centre of the lens sample by visual observation. After aligning the needle tip with the centre of the lens, the automated system moved the needle towards
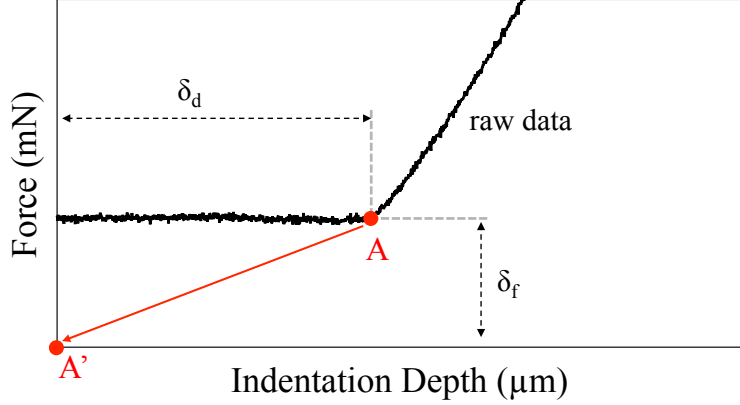
Figure 5.5: The raw data is preprocessed by shifting point A by $(\delta_d,\ \delta_f)$, such that point A is located at the origin A' for each measurement.

the lens in order to identify the contact point between the sensing tip and the lens using a force of $80\,\mu N$. Contact was established and the point was defined as the zero indentation of the lens. Following the contact phase was the measurement phase with the sensor indenting the lens capsule with speed v_{ind}. The indentation depth and the measured forces were recored continuously until the procedure was stopped after visual confirmation of perforation of the lens capsule.

5.2.1.4   Data Preprocessing

After force-indentation data had been recorded for each lens capsule perforation experiment, the raw data were preprocessed, as illustrated in Fig. 5.5. Due to the approach of the force sensor, the shape difference between lenses, and a force offset due to adhesion, the raw data are shifted by an offset (δ_d, δ_f). To compare data during further analysis, raw data were preprocessed, such that the origin of the measured data A is coincident with a global origin A', where force and indentation depth are defined as zero for all measurements.

5.2.1.5   Statistical Analysis

All perforation force and indentation data acquired during the *needle-size study* were separated into six groups according to needle diameter and day of experimentation (Table 5.1) to account for day-to-day variation in the eyes. A one-way analysis of variance (ANOVA) was performed to break the total variation in the measured perforation forces into the variation among group means and that due to differences within the groups [117]. The F-statistic was used to assess the difference among group means. Subsequently, the single group means were compared utilising contrasts, keeping either needle diameter or experimentation day constant. As sample sizes of each group are relatively small, for all statistical analysis statistical significance was gauged at a critical p-value of $p = 0.003$ ensuring a large confidence interval. The perforation force and indentation data acquired during the *needle-speed study* were divided into three groups according to indentation speed v_{ind}. To test the null hypothesis in the one-way ANOVA, which states that all means are equal, the critical F-statistic was calculated with a p-value of $p = 0.003$.

5.2.1.6   Model Identification

To evaluate the correlation between all measured indentation forces and indentation depths and to identify a bio-mechanical model for lens perforation, a nonlinear curve fitting algorithm was used in MATLAB (`lsqcurvefit`). This nonlinear least-square solver finds coefficients that minimise the residuals between a given function and the measured data. The optimisation is stopped when the relative sum of squares is changing by less than a given tolerance of 10^{-6}.

5.2.2   Results

Figure 5.6 illustrates a force-indentation graph showing the shifted data after preprocessing. Labelled *A* in the figure, the measured force increases nonlinearly with increasing indentation depth when indenting the lens capsule with a sharp needle. The elastic lens capsule stretches until the applied indentation
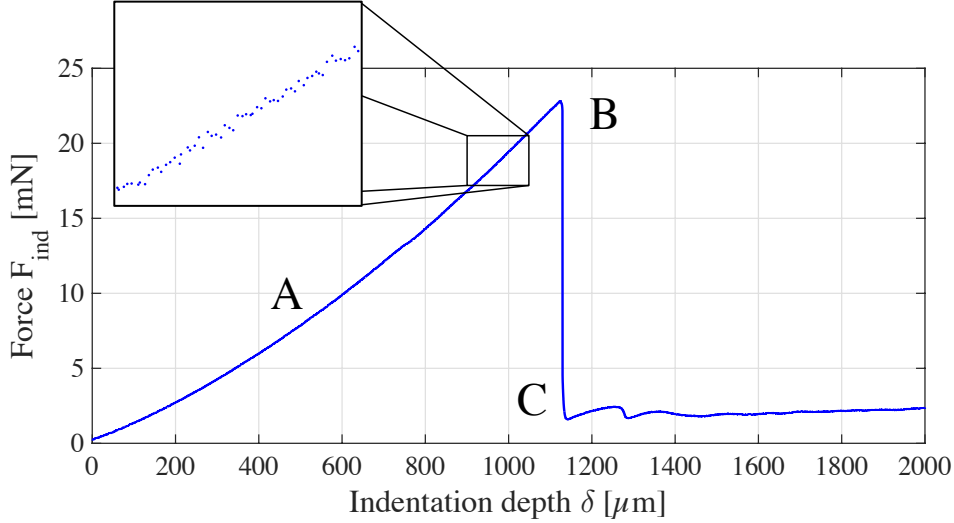
Figure 5.6: Force-indentation graph for a typical measurement after prepro-
cessing. The measured indentation force increases with increasing indentation
depth, A, until it reaches a maximum at B, the perforation force, puncturing
the lens capsule.

force causes perforation of the lens capsule at point B in the figure. After
perforation of the lens capsule the measured force decreases rapidly (point C)
as the needle further indents the lens cortex material. During further analysis
the maximum perforation force in relation to needle diameter and indentation
speed is investigated.

5.2.2.1   Needle-Size Studies

The perforation forces and indentation depths are identified for each measure-
ment in each group, which are separated by needle diameter and the day when
the experiments took place. The distribution of measured perforation forces
are plotted according to needle diameter and experimentation day in Fig. 5.7
and summarised in Table 5.2. All measurements are conducted at an average
indentation speed of $v_{ind} = 8.55 \pm 0.09$ µm/s. As the critical F-value (3.96,
$p = 0.003$) is smaller than the calculated F-statistic (11.34), the means of the
single groups show a statistically significant difference. The contrasts analysis
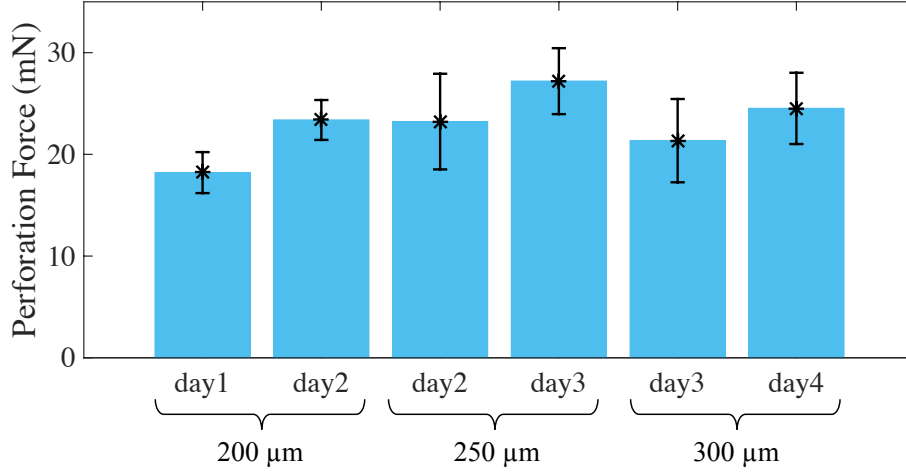
Figure 5.7: Mean value and standard deviations of measured perforation force for each group.

Table 5.2: Mean and standard deviation of perforation forces in [mN] with various needle diameters with constant indentation speed $v_{ind} = 8.55 \pm 0.09\,\mu\text{m/s}$.

d_{ind}	day1	day2	day3	day4
200 µm	18.21 ± 2.02	23.38 ± 1.96	-	-
250 µm	-	23.22 ± 4.70	27.20 ± 3.24	-
300 µm	-	-	21.35 ± 4.09	24.52 ± 3.50

indicates that 200 µm-needle perforation forces are smaller than those measured with a needle with diameter of 250 µm within a confidence interval of $\pm$ 2.89 mN. However, no significant difference of the perforation forces was found between needles with 250 and 300 µm. Furthermore, no statistically significant difference was found between perforation forces on the first and second day of experimentation with the same needle.
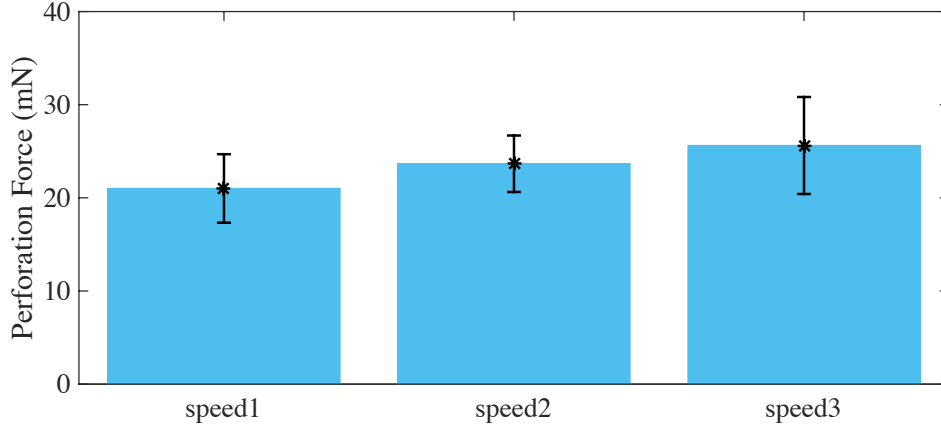
Figure 5.8: Mean value and standard deviations of measured perforation force for each indentation speed v_{ind}.

Table 5.3: Mean and standard deviation of perforation forces with various indentation speeds with constant needle diameter of $300\,\mu$m and number of experiments.

v_{ind}	perforation force	n
8.57 ± 0.02 µm/s	23.42 ± 2.37 mN	9
32.38 ± 1.41 µm/s	23.33 ± 3.02 mN	9
70.35 ± 9.91 µm/s	26.83 ± 5.94 mN	7

5.2.2.2   Needle-Speed Studies

The mean and standard deviation of perforation forces when indenting the anterior lens capsule with different indentation speeds v_{ind} are shown in the bar graph in Fig. 5.8 and summarised in Table 5.3. The analysis of variance suggests that there is no statistically significant difference between the mean perforation forces in this study.

5.2.2.3   Nonlinear Curve Fitting

In a first approach the well accepted Sneddon model for indentation of elastic material [118, 119] is fitted to the measured force-indentation data. This model assumes a polynomial relationship between force F and indentation depth δ of the form

$$F = C \cdot \delta^{1.5}. \tag{5.1}$$

Analysis shows that this model fits well for small indentation, but deviates from the measurement for larger loads with a minimal R^2-value of 0.9669. An exponential fit of the form

$$F = a \cdot (e^{\gamma \delta} - 1). \tag{5.2}$$

fits the entire dataset with a minimal resulting R^2-value of 0.9864. The optimal a and γ are recorded for each measurement and the means and standard deviations are summarised in Table 5.4.

Utilising normal probability plots for the perforation forces and indentation at perforation for each measurement it was validated that both, perforation force and indentation, follow a normal distribution. Thus, a multi-variant normal distribution of puncturing a porcine anterior lens capsule at a given force and indentation depth can be found. All measured perforation forces and corresponding indentation depths are plotted in Fig. 5.9. The multi-variant probability of perforation is illustrated with coloured contours. The solid line represents the mean of the exponential fits for all measurements in the form of

Table 5.4: Mean and standard deviation of parameters a and γ for the exponential curve fit in the form of $F = a \cdot (e^{\gamma \delta} - 1)$.

	mean	std. dev.
a [mN]	13.13	6.46
γ [μm^{-1}]	$8.06 \cdot 10^{-4}$	$1.49 \cdot 10^{-4}$
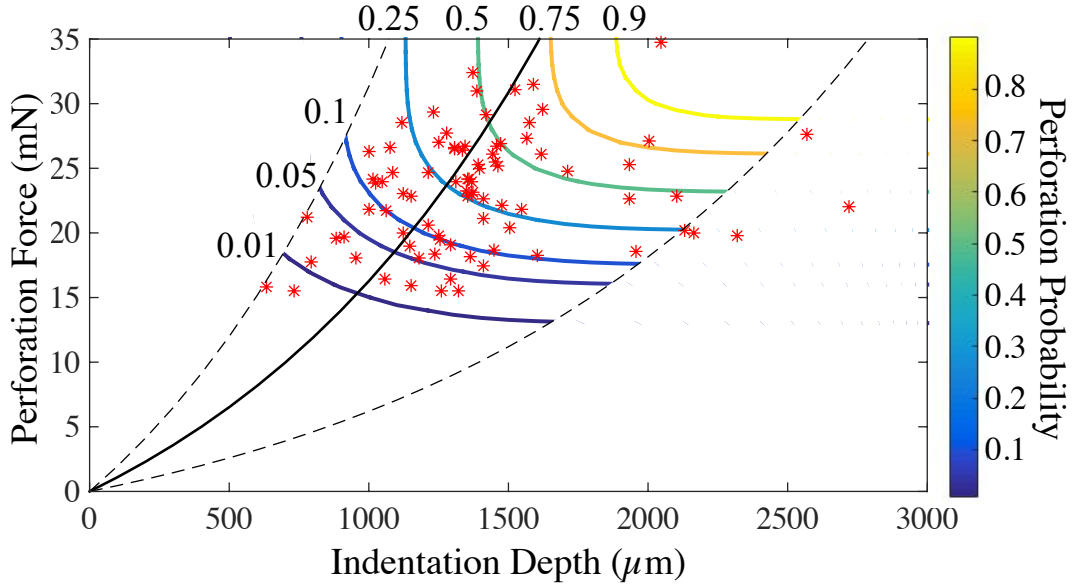
Figure 5.9: Measured perforation forces at corresponding indentation depths (red asterisks). The contours illustrate the multi-variant probability of perforation. The mean of the exponential fits in the form of Equation 5.2 is plotted (solid line) and is bounded by one standard deviation (dashed lines).

Equation 5.2 and the dashed lines represent a 1σ variation in the curve.

The data acquired during the studies in this chapter are of particular interest for surgeons performing manual capsulotomy and researchers developing robotic devices that assist in cataract surgery. As the proposed method is similar to the manual procedure of penetrating the lens capsule during capsulorhexis with a sharp tip needle or cystotome, measured forces are comparable to those occurring during surgery. The porcine lens capsule is thicker and acts as a conservative model for the human lens capsule, as suggested from qualitative surgical experience [114]. Thus, the measured forces in this study provide an upper estimate of the perforation force occurring during capsulotomy and potentially assist in the development of force controlled tools for cataract surgery. The question remains how the obtained results relate to the perforation forces of a human lens capsule. As the testing method has been verified with porcine

lenses, the same method could be used to test a smaller subset of human lenses to analyse if the porcine model is indeed conservative.

As expected, it was found that the penetration force for the $200\,\mu$m-needle is lower than for the $250\,\mu$m-needle at a p-value of $p = 0.003$. But due to either variation in the specimens tested day-to-day or dulling of the needle tip, it cannot be stated with confidence a relationship between the $250\,\mu$m-needle and $300\,\mu$m-needle. Generally, average perforation forces measured on intact porcine anterior lens capsules differ from one day to another, suggesting variation between individual eyes. These variations might be caused by the pig breed, prior nutrition, or exposure to UV light. In this study, a statistically significant difference between penetration forces due to a variation in indentation speed was not observed. For low indentation speeds the lens capsule material can be considered purely elastic, ignoring any viscous effects. To analyse full viscoelastic behaviour of the lens material, measurements could be repeated with larger indentation speeds.

This section shows that the measured force-indentation curves are best presented by an exponential fit in the form of Equation 5.2. The exponential correlation between indentation force and depth is indicative for a strain hardening material, which is not surprising since many biological tissues exhibit strain hardening material properties [120].

The intact lens is extracted from the porcine cadaver eye and placed in a lens holder to restrict lateral motion of the specimen. By placing the lens in its holder, no pre-strain is purposely created. In the living eye the lens is elastically suspended from the zonular fibres, which slightly pre-strain the capsular bag. Experiments were done on porcine lenses with an intact capsular bag, but outside of the eye and, thus, ignoring the effect that zonular fibres may have on the measured perforation forces. However, *in vivo* pre-straining of the lens would decrease the required force for perforation of the lens capsule, thus, rendering our model more conservative. In eyes with pseudoexfoliation

syndrome (PEX), the zonular fibres tend to be more elastic and the lens may retreat during capsulotomy. Thus, indentation depth during penetrating the lens capsule may be influenced to some extent, resulting in the alteration of the relationship shown in Fig. 5.9.

5.3 Experimental System for Automated Capsulorhexis

A system for automated minimally invasive capsulorhexis is proposed, which consists of a flexible catheter with an end-effector. The catheter is controlled by a hybrid magnetic-mechanical actuation system to circumscribe a circular path with known dimensions inside the aqueous chamber of the eye. The catheter is guided with a hybrid magnetic-mechanical actuation system consisting of a mechanical catheter advancer (MCA) that controls the longitudinal motion of the tip while the lateral movement is controlled by the electromagnetic manipulation system, the OctoMag, described in Chapter 3.2.

The end-effector is used to cut the lens capsule, such that a well-defined capsulorhexis is created. As previously suggested (Section 5.2), forces for lens capsule penetration are in the range of 15 to 35 mN and, thus, are too large to be applied by a fully magnetically controlled tool as size constraints apply. Therefore, a diathermy tool for thermal cutting of the lens capsule has been developed and is described in Section 5.3.2.

5.3.1 Mechanical Catheter Advancer

The mechanical catheter advancer (MCA), as illustrated in Fig. 5.10, consists of two powered modules, an inner and an outer module. The inner module is responsible for longitudinal advancement of a catheter, while the outer module rotates the catheter around its long axis. To reach into the OctoMag workspace, the MCA is fixed on a platform and located on the supporting frame of the magnetic manipulation system. Each DoF is actuated by a stepper motor (SPG1518M0504-50, Nanotec Electronic GmbH, Germany) with a resolution of $0.36°$ or 1000 steps per revolution. In the inner module, a worm drive unit with

gear ratio 1:30 transmits the motor rotation via a timing belt to the catheter
advancing rollers. A mechanism was developed with two passive spring-loaded
rollers mounted opposite the active rollers to provide sufficient axial friction.
An optical quadrature incremental encoder (HEDS-9100, Avago Technologies
Inc., USA) is fixed on the rotated axis to estimate the position of the catheter
advancer. The encoder resolution is 500 pulses per revolution. By detecting
the edges of the pulse signals, the resolution can be increased fourfold. The
advancement of the catheter a_c in the axial direction is computed as

$$a_c = c_{enc} \cdot \frac{2\pi \cdot r_{adv}}{CPR_{enc}} \qquad (5.3)$$

where c_{enc} are the measured encoder pulses, r_{adv} is the radius of the advancing
roller, and CPR_{enc} are the counts per revolution of the encoder.

The outer module is used to rotate the inner module and thus rotates the
catheter around its longitudinal axis. A worm drive with a higher gear ratio
(1:60) connects the second stepper motor to the rotational axis. The same
optical encoder is attached to estimate the rotation of the inner module. A
slip ring allows to transfer electrical signals to an embedded microcontroller
(Arduino).
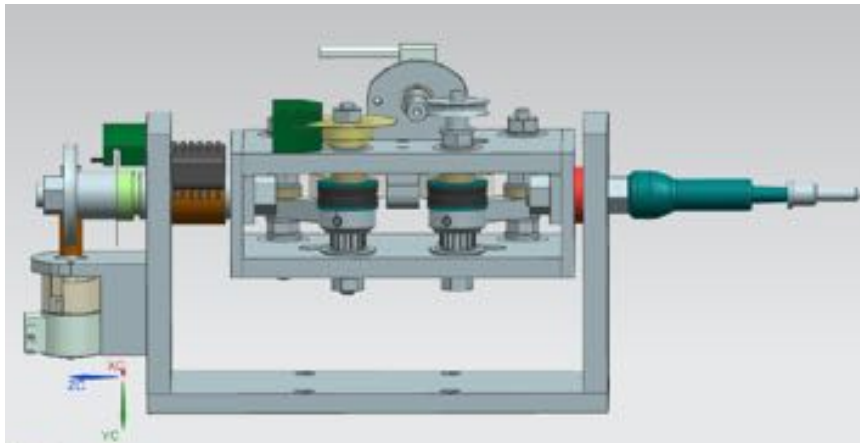
Figure 5.10: CAD design of mechanical catheter advancer with two degrees of
freedom.
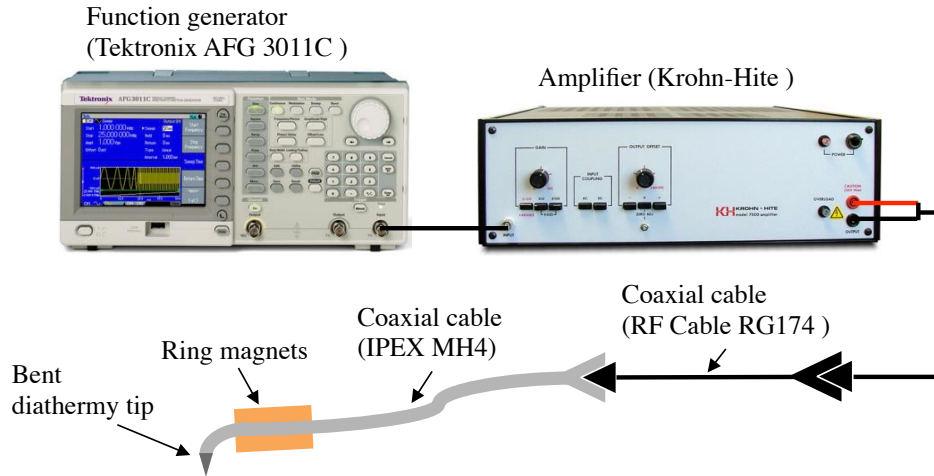
Figure 5.11: Customised diathermy tool for thermally cutting the lens capsule during capsulorhexis.

5.3.2   Diathermy Tool for Lens Tissue Cutting

The most commonly used method to open the anterior lens capsule during cataract surgery is a procedure called continuous curvilinear capsulorhexis (CCC). Endodiathermy, an alternative method to CCC, was first described in 1984 [121]. It involves coagulation and thermal cutting of the lens capsule with a small probe using high-frequency (HF) currents of $500\,\mathrm{kHz}$. Endodiathermy uses HF alternating currents to directly heat the tissue to approximately $160\,^{\circ}\mathrm{C}$ and, thus, thermally cut the lens capsule material [122]. Bipolar diathermy requires a power output of 4.5 to $9\,\mathrm{W}$. The prior insertion of a viscoelastic fluid into the anterior eye segment improves the flow of the HF current and increases visualisation of the capsulotomy edge [123]. The capsulotomy method was evaluated in clinical studies [124] and no statistically significant changes in the anatomical structures were found, except the cornea quality was found to be better after HF diathermy capsulotomy compared to CCC. Additional advantages of endodiathermy for creating an opening in the lens capsule have been identified as the ease to learn and execute this type of capsulotomy, the defined shape and size, the smooth edge of the opening, and the controlled conditions (*i.e.* no radial tearing of capsule) [122, 124]. A rigid endodiathermy probe for

capsulotomy is commercially available from Oertli Instrumente AG [125].

A customised HF current probe is developed and attached to the magnetic catheter for automated capsulorhexis with hybrid magnetic-mechanical actuation. A schematic of the developed system is illustrated in Fig. 5.11. A function generator (AFG 3011C, Tektronix Inc., USA) is used to generate alternating HF current signals with frequencies up to 10 MHz and a maximal peak-to-peak voltage of 20 V. For experiments, frequencies between 250 and 900 kHz were chosen and two signal generation modes were used. The continuous mode emits a generated sine or pulse waveform signal continuously in time, while the burst mode allows the user to switch the produced signal on and off for a fixed amount of cycles. The signal from the generator is amplified with a wide band power amplifier (Model 7500, Krohn-Hite Corporation, USA). In the design, the alternating current (AC) signal travels through a coaxial cable (IPEX MH4, Taoglas, Ireland) with a diameter of 0.8 mm to the bent diathermy tip, which heats the capsule tissue while the catheter is moved along a predefined path. Five ring shaped permanent magnets (grade N50) with a total magnetic volume of $47.12 \, \text{mm}^3$ are attached behind the diathermy tip, as seen in Fig. 5.11, to render the catheter magnetic for lateral control of the end-effector with the OctoMag. The diathermy tip is fabricated from the coaxial cable, where the inner conductor extents from the outer conductor, and the two conductors are separated by an insulation layer. Subsequently, the diathermy tip is electroplated with a thin layer of gold to prevent wear of the tip. Figure 5.12 illustrates the tip of the diathermy tool.

5.4   Closed Loop Control

During capsulorhexis a catheter is guided along a predefined elliptical trajectory with axis lengths a and b, as illustrated in Fig. 5.13(a). The catheter with total length L and bending stiffness EI enters the eye through a trocar and is anchored at the *anchor point* ($s = 0$), as seen in the figure. During control, the error e between a desired point on the trajectory (r_x^d, r_y^d) and the tracked catheter tip (x_{cat}, y_{cat}) is minimised.

(a)

(b)
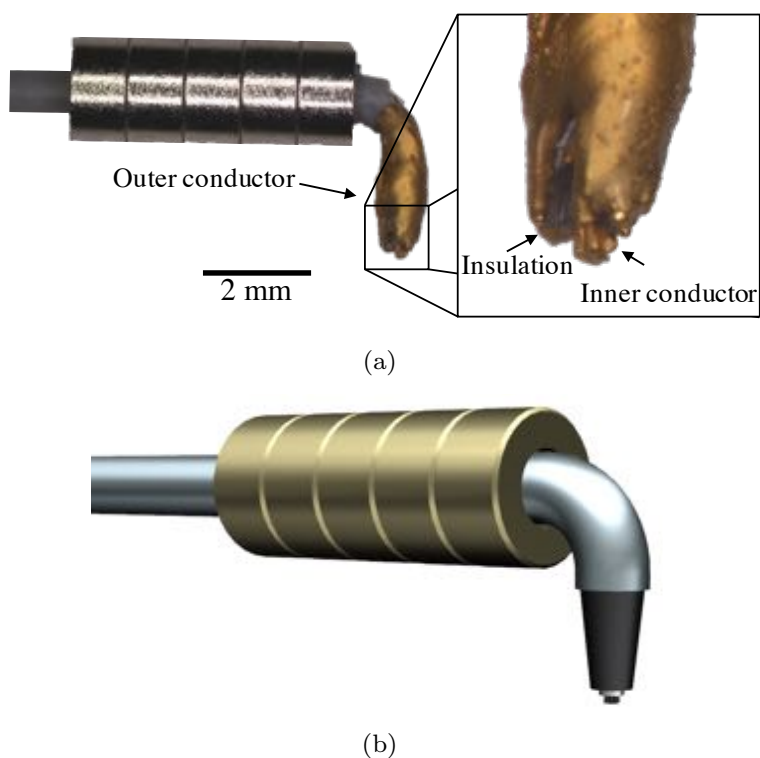
Figure 5.12: (a) Photograph of a fully assembles diathermy tip. The outer and inner conductor as well as the insulation layer are shown. (b) CAD rendering of the diathermy tool tip, including five ring magnets.

5.4.1   Catheter Model

If a catheter is fixed on one end and free on the other, it can be modelled as a cantilever beam using Euler-Bernoulli beam theory [126]. A schematic view of a cantilever beam subjected to a combined tip point loading is illustrated in Fig. 5.13(b). In the absence of an end-force (*i.e.* $f_0 = 0$), a pure bending moment (M_0) is applied at the free tip and the catheter deflection $(x_{cat}(s), y_{cat}(s), \theta_{cat}(s))$ is given by

(a)

(b)
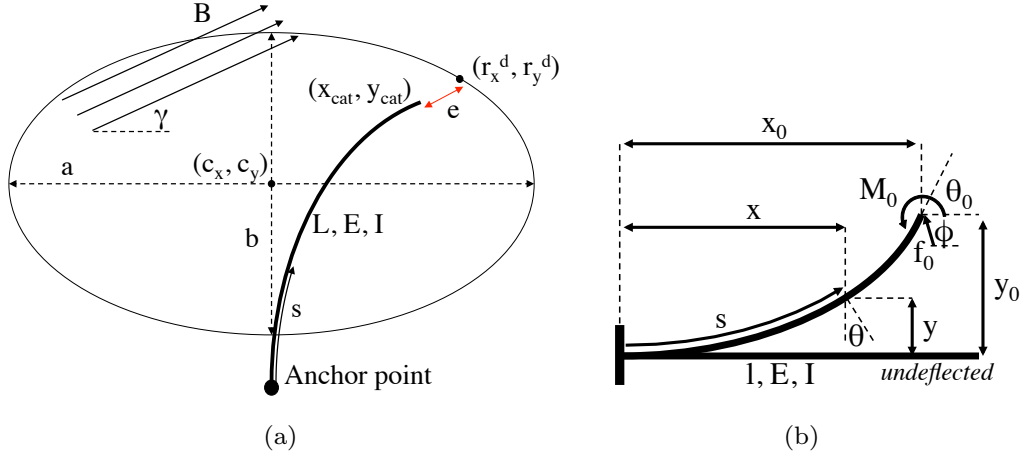
Figure 5.13: (a) Motion model of the controlled catheter which travels along a predetermined elliptical trajectory. (b) A schematic view of a cantilever beam subject to combined tip point loading (moment: M_0 and force f_0). Adapted from [126].

$$\theta_{cat}(s) \quad = \quad \frac{M_0}{EI} s \tag{5.4}$$

$$x_{cat}(s) \quad = \quad \frac{EI}{M_0} \sin\left(\frac{M_0}{EI} s\right) \tag{5.5}$$

$$y_{cat}(s) \quad = \quad \frac{EI}{M_0}\left(1 - \cos\left(\frac{M_0}{EI} s\right)\right) \tag{5.6}$$

where E is the Young's modulus of the catheter material and I is its moment of inertia.

Another mechanical model for catheter bending utilises the principle of stationary potential energy and computes the equilibrium configuration of a catheter for pure end-moments [127]. The equations describing the catheter tip position are similar to Equations 5.4 to 5.6, but with an additional term for the rigid end-effector, *e.g.* the diathermy tool, at the tip of the catheter. The length of

the entire catheter and end-effector is L, while the length of the flexible part is given by l, where $l < L$. The tip position of the catheter is derived by

$$\theta_{cat}(L) = \kappa L \tag{5.7}$$

$$x_{cat}(L) = \frac{\sin(\kappa l)}{\kappa} + (L - l)\cos(\kappa l) \tag{5.8}$$

$$y_{cat}(L) = \frac{1 - \cos(\kappa l)}{\kappa} + (L - l)\sin(\kappa l) \tag{5.9}$$

with boundary condition

$$M = EI\kappa = \mu B \sin(\gamma - \kappa l) \tag{5.10}$$

where B is the magnitude of the magnetic field, γ is the magnetic field angle, and the curvature of the catheter κ is given by

$$\kappa = \frac{M}{EI}. \tag{5.11}$$

5.4.2   Control Algorithm

Figure 5.14 summarises the control scheme for closed loop control of the tool for automated capsulorhexis. The desired catheter tip position (X_{des}) serves as an input to the catheter controller that makes use of the catheter model to derive the required tip moment M_0, and from this compute the desired magnetic field B_{des} as well as the desired length of the catheter L_{des}. The required magnetic field is used by the OctoMag controller to set the individual coil currents. The servo-controller of the MCA uses the measurements from the optical encoder, computes the error between the desired length of the catheter and its actual length, multiplies it with a proportional gain K_p and sends the control action to the stepper motor. This loop is repeated until the error is below a predefined threshold. The image from the camera is used as feedback to close the main loop of the control system. A blob tracker detects the position of the catheter tip on the image and feeds it back to the catheter controller.
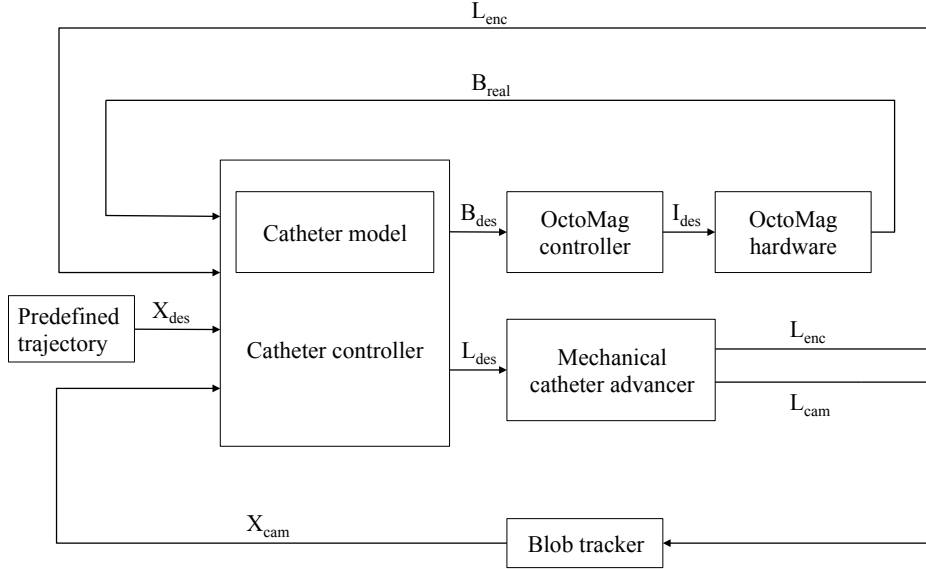
Figure 5.14: Control scheme for closed loop position control of the tool for automated capsulorhexis.

This section describes the control algorithm used for catheter guidance, based on the derivation by Tunay [127]. The design of the feedback control algorithm necessitates an understanding of the system dynamics and the derivation of the state equations. The reference path trajectory is given by $\mathbf{r^d} = [r_x^d, r_y^d]$ and t denotes the time. The system state ($\mathbf{x}$), system output ($\mathbf{y}$), and control input to the system ($\mathbf{u}$) are given by

$$\mathbf{x} = [\kappa, \quad \gamma, \quad L]^T \qquad (5.12)$$

$$\mathbf{y} = [r_x, \quad r_y]^T \qquad (5.13)$$

$$\mathbf{u} = [\dot{\gamma}, \quad \dot{L}]^T \qquad (5.14)$$

where the dot notation symbolizes the time derivative. Here, κ defines the catheter curvature, L the catheter length, and γ is the angle of the applied magnetic field. The control variables $\mathbf{u}$ are the rates of change of the field orientation and the catheter advancement, respectively.

The tip position of the catheter is given by Equations 5.4 to 5.6. The analytical form of the state equations can be derived by using the boundary condition and differentiating over the time t to give

$$\dot{x}_1 \;\; = \;\; \frac{\mu B \cos(x_1 x_3 - x_2)(u_1 - x_1 u_2)}{\beta + \mu B \cos(x_1 x_3 - x_2) x_3} \tag{5.15}$$

$$\dot{x}_2 \;\; = \;\; u_1 \tag{5.16}$$

$$\dot{x}_3 \;\; = \;\; u_2 \tag{5.17}$$

and can be written in matrix form as

$$\dot{\mathbf{x}} \;\; = \;\; G(x) \cdot \mathbf{u} \tag{5.18}$$

$$= \;\; \begin{pmatrix} \frac{\mu B \cos(x_1 x_3 - x_2)}{\beta + \mu B \cos(x_1 x_3 - x_2) x_3} & -\frac{\mu B \cos(x_1 x_3 - x_2) x_1}{\beta + \mu B \cos(x_1 x_3 - x_2) x_3} \\ 1 & 0 \\ 0 & 1 \end{pmatrix} \cdot \mathbf{u} \tag{5.19}$$

where $\beta = EI$ is the bending stiffness of the catheter.

From the matrix form it is observed that the system is uncontrollable only for $x_1 x_3 - x_2 = \pm(2k + 1)\frac{\pi}{2}$, i.e. $\cos(x_1 x_3 - x_2) = 0$, and the angle between the field and the catheter is an odd multiple of 90°. Additionally, the output equation takes the form of

$$\mathbf{y} \;\; = \;\; h(x) \tag{5.20}$$

$$= \;\; \begin{pmatrix} \frac{\sin(x_1 x_3)}{x_1} + (x_3 - l)\cos(x_1 x_3) \\ \frac{1 - \cos(x_1 x_3)}{x_1} + (x_3 - l)\sin(x_1 x_3) \end{pmatrix}. \tag{5.21}$$

The tracking error in x- and y-direction $\mathbf{e(t)}$ between the catheter tip position and the corresponding reference trajectory point on the desired circular path is defined as $\mathbf{e(t)} = \mathbf{r^d(t)} - \mathbf{y(t)}$ and its derivative is equal to

$\dot{\mathbf{e}}(\mathbf{t}) = \dot{\mathbf{r}}^{\mathbf{d}}(\mathbf{t}) - \dot{\mathbf{y}}(\mathbf{t})$. Furthermore, the system dynamics of the system are non-linear. Thus, the Jacobian matrix of the output can be used as a decoupling matrix and is defined as $J(x) = \frac{\partial h(x)}{\partial x} G(x)$. In the case that $G(x)$ is controllable, J(x) is non-singular and $\dot{\mathbf{y}} = J(x)\mathbf{u}$. The control action is computed in order to position the catheter tip on the reference path trajectory as

$$\mathbf{u} = J(x)^{-1}\dot{\mathbf{y}} = J(x)^{-1}\left(\dot{\mathbf{r}}^{\mathbf{d}}(\mathbf{t}) - \dot{\mathbf{e}}(\mathbf{t})\right) \tag{5.22}$$

In order to account for system stability, exponentially stable, decoupled, and linear error dynamics are desired. This condition is satisfied by choosing $\dot{\mathbf{e}}(\mathbf{t}) = -K_p\mathbf{e}(\mathbf{t})$ with $K_p > 0$. Thus, Equation 5.22 can be expressed as

$$\mathbf{u} = J(x)^{-1}\dot{\mathbf{y}} = J(x)^{-1}\left(\dot{\mathbf{r}}^{\mathbf{d}}(\mathbf{t}) + K_p\mathbf{e}(\mathbf{t})\right) \tag{5.23}$$

To move the catheter tip along an elliptical trajectory with given axes, the reference path $\mathbf{r}^{\mathbf{d}}(\mathbf{t})$ is given by

$$\mathbf{r}^{\mathbf{d}}(\mathbf{t}) = \begin{pmatrix} c_x - a\cos(\theta(t)) \\ c_y - b\sin(\theta(t)) \end{pmatrix} \tag{5.24}$$

where c_x and c_y are the coordinates of the elliptical trajectory's centre with respect to the catheter frame. Parameters a and b are the lengths of the two axes of the elliptical path, and $\theta(t)$ is the angle between the centre and the sampled point of the path. As summarised in Fig. 5.15, the control action $\mathbf{u}$ is computed for each point on the predefined trajectory and sent to the OctoMag and the MCA, to move the catheter tip along an ellipse. The controller contains a feed-forward and a feedback action. The feedforward action determines the angular velocity with which the path should be executed and forces the catheter tip to move to the next point after a given timeout period. The feedback action is the blob tracker output, which sends the tracked tip position back to the catheter controller to calculate the tracking error $\mathbf{e}(\mathbf{t})$. Subsequently, the error is multiplied with a proportional gain K_p, subtracted from the feedforward action, and multiplied with the inverse Jacobian $J^{-1}(x)$, as indicated in Equation 5.23.
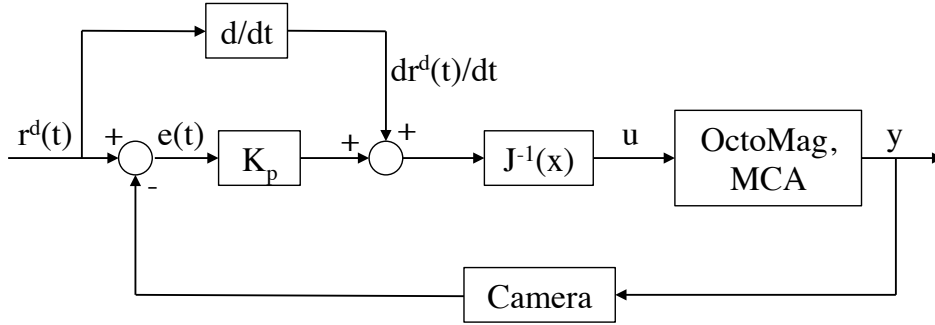
Figure 5.15: Block diagram of the non-linear position controller.

The control action **u** is sent to the system to position the catheter tip with a minimal error. This loop iterates until the path is successfully completed.

5.5   Experimental Evaluation for Automated Capsulorhexis

Several experiments were performed to derive catheter parameters that were later used during catheter position control. Furthermore, experiments have been conducted to test the cutting performance of the diathermy tool in the process of automated capsulorhexis on *ex vivo* porcine eyes.

5.5.1   Experimental Derivation of Catheter Elasticity

During a first set of experiments, a polyurethane (PUR) catheter was used with outer and inner diameters of $0.6\,\text{mm}$ and $0.3\,\text{mm}$, respectively. Three Neodymium-Iron-Boron (NdFeB, N40) magnets are attached to the tip of the catheter, accounting for a total magnetic volume of $0.589\,\text{mm}^3$. The position controller, as described in Section 5.4, makes use of the catheter model. Thus, knowledge about the catheter's bending behaviour, *i.e.* Young's modulus E, is required. To account for possible variations of E along the catheter or other unknown influences, experiments were conducted to test the bending behaviour during magnetic actuation. The measured elasticity E_{meas} is expected to differ from the material constant E at large deflections and due to unknown environmental influences. During experiments, the catheter tip
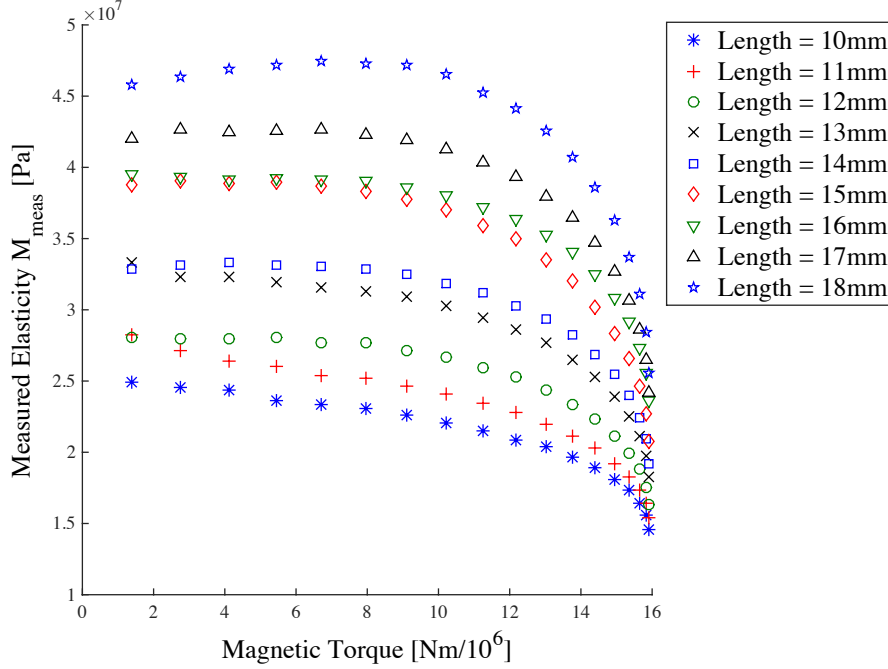
Figure 5.16: Measured elasticity of the magnetic catheter when subject to externally applied magnetic torques. The length of the catheter is altered between 10 and 18 mm to account for catheter advancement. Data are used to provide a lookup table to the position controller.

was inserted into a petri-dish filled with distilled water and placed within the OctoMag workspace. A magnetic field of 30 mT was applied, while the field orientation was altered between 0 and 90° with a stepsize of 5° with respect to the longitudinal catheter axis. To account for the advancement of the catheter during capsulorhexis, its length was changed between 10 and 18 mm with a stepsize of 1 mm. The catheter tip (x_{cat}, y_{cat}) was tracked with a blob tracker and the measured elasticity was derived from Equations 5.8 and 5.9. The area moment of inertia of the catheter is assumed to be

$$I = \frac{\pi}{4}(R^4 - r^4),\tag{5.25}$$

where R and r are the outer and inner catheter diameters, respectively.

Figure 5.16 summarises the experimental results of the measured elasticity E_{meas} and is used to create a lookup table, which is referred to by the catheter controller during position control. For position control of the catheter, the measured elasticity is used instead of a constant E. In the figure, the applied magnetic torque is derived with the knowledge of the total magnetisation and the applied magnetic field (Equation 3.1).

5.5.2   Position Control of Catheter Tip

The magnetic catheter and vision based closed loop position control are tested in an aqueous environment at magnetic field strength of 30 mT. During experiments, the magnetic catheter is advanced and retracted by the MCA and is guided into the OctoMag workspace through a small tube, the anchor shaft, into a petri-dish filled with distilled water. A reference trajectory is selected on the user interface. During execution of the trajectory following, the catheter tip is observed through a calibrated camera and visually tracked using a blob tracker. Position control of the catheter tip is evaluated for different trajectories, *i.e* circular and elliptical paths. Figure 5.17 shows the tracked position of the tip while being controlled along different predefined paths (dashed line). Hybrid magnetic-mechanical actuation of a magnetic catheter tip results in circular and continuous motion of the tip with a defined centre location, as illustrated in the figure.

The position error of the catheter tip is computed as the perpendicular distance between the tracked and the desired trajectory in polar coordinates. Table 5.5 summarises the mean and standard deviation of the measured position error for different trajectories. Results are illustrated in Fig. 5.18. It is shown that the closed loop position control allows for high reproducibility of a trajectory with a mean position error of less than 1% in relation to the largest dimension of the trajectory shape. However, the results may be affected by image noise and small variations in lighting conditions.

(a) (b)
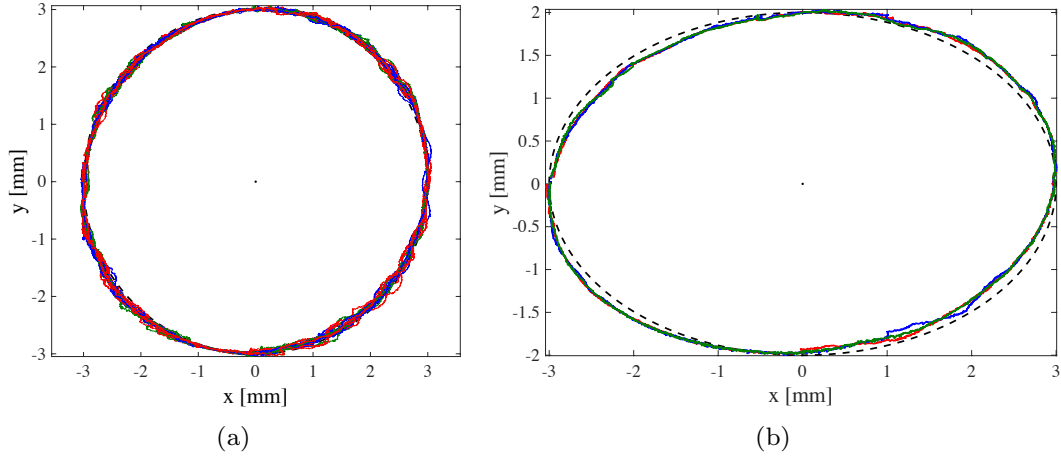
Figure 5.17: Position control of the magnetic catheter tip. The dashed line represents the reference trajectory: (a) a circle with diameter of 6 mm ($n = 20$), (b) an ellipse with axis lengths 4 and 6 mm ($n = 3$), respectively.

Table 5.5: Mean and standard deviation of position errors of the tracked tip of a magnetic catheter following different trajectories.

Trajectory	Mean error [mm]	Std. error [mm]
Circle, ⊘ 4 mm	0.016	0.014
Circle, ⊘ 6 mm	0.038	0.025
Ellipse, 4 and 6 mm	0.051	0.030

5.5.3   Thermal Cutting of Capsular Bag

To investigate the feasibility of a magnetically guided diathermy tool for capsulorhexis (as described in Section 5.3.2), the tool's cutting capabilities were tested on *ex vivo* porcine lenses. Furthermore, the diathermy tool was guided along a circular path on the porcine lens by the position control algorithm (Section 5.4.2) while thermally cutting the lens capsule tissue.
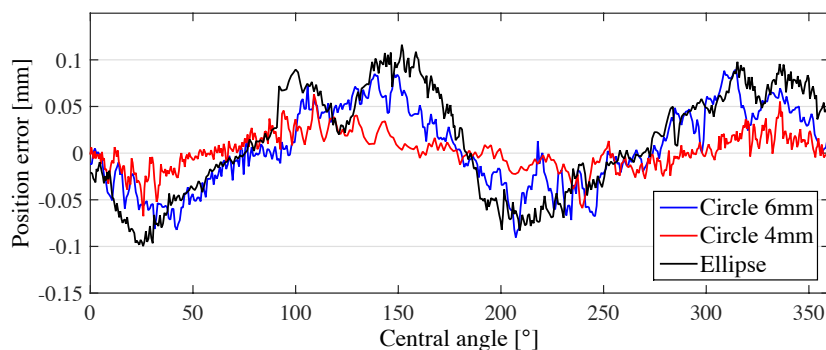
Figure 5.18: Measured position error of the catheter tip when following different trajectories. The average position error is smallest (0.016 mm) for a circular path with a diameter of 4 mm and largest (0.051 mm) for an elliptical trajectory with axis lengths 4 and 6 mm.

5.5.3.1   Parameter Testing

In a first cutting experiment several parameters of the diathermy system were tested while creating linear thermal cuts on *ex vivo* porcine lenses. The evaluated parameters include the type of the waveform (*sine* or *pulse*), the mode (continuous signal or *burst*) and duty cycle of the signal, the total peak-to-peak voltage of the signal, and its frequency. The tested parameters and their according values are summarised in Table 5.6. All experiments were performed on lenses from porcine eyes that had been obtained from the abattoir on the same day and were stored in cold water until experimentation. The porcine lenses were carefully extracted from the eyes, placed in a 3D-printed lens holder to prevent lateral motion during experiments, and covered with balanced salt solution (BSS), silicone oil, or eye drops. Several cuts were made with varying parameter combinations on a total of 29 lenses and the cuts were evaluated according to the quality of the edge, the depth of the cut, and its length. The optimised parameters for thermal cutting of a porcine capsular bag with the customised diathermy tool are shown in Table 5.7.

Table 5.6: The tested parameters for thermal cutting experiments with a flexible diathermy tool.

Parameter	Value	Unit
Waveform Type	*sine* or *pulse*	-
Mode	*continuous* or *burst*	-
Duty Cycle	10 to 70	%
Total Voltage	190 to 310	V
Frequency	300 to 900	Hz
Lens covered with	BSS, silicone oil, or eye drops	-

Table 5.7: Experimentally optimised parameters for thermal cutting of the porcine lens capsule with a custom built flexible diathermy tool.

Waveform	Duty cycle	Voltage	Frequency	Covered in
pulse	20%	370 V	500 Hz	BSS

5.5.3.2   Capsulorhexis

After determining the optimal parameters for thermal cutting with the custom built diathermy tip, experiments were performed to demonstrate a full capsulorhexis on an anterior porcine lens capsule utilising the closed-loop controlled mechanical-magnetic actuation system and the diathermy tip. For this, the mechanical catheter advancer controls the flexible tool's longitudinal direction, while the lateral motion of the tip is guided by magnetic fields generated by the OctoMag. A blob tracker is used to track the diathermy tip and the closed-loop control algorithm (Section 5.4.2) guides it along a circular trajectory with predetermined diameter while thermally cutting the lens capsule.

Figure 5.19 shows three consecutive images of the diathermy tip moving on a circular trajectory (indicated by the white circle in Fig. 5.19(a)) while cutting the lens capsule of an *ex vivo* porcine lens. The white arrow in Fig. 5.19(c) points to released air bubbles during the thermal cutting process and

(a)   (b)   (c)
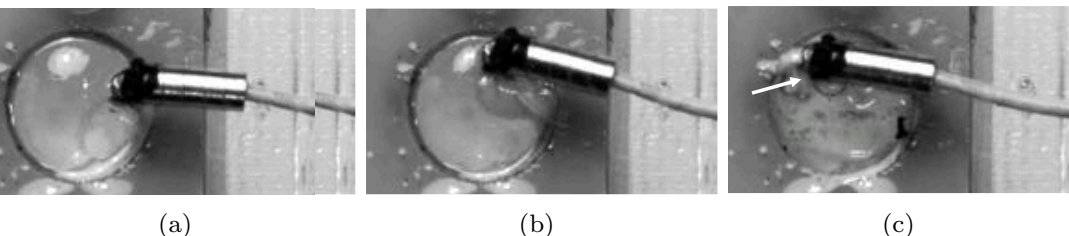
Figure 5.19: Capsulorhexis using a custom built diathermy tip with a flexible body for mechanical-magnetic actuation.

indicates that the tip temperature is above the boiling point of water. Air bubble formation during thermal capsulorhexis were also observed by Krag et al. [128] and Gassmann et al. [122].

Figure 5.20 shows a complete capsulorhexis performed with the customised diathermy tip when guided along a circular trajectory by the mechanical-magnetic actuation system. The section outlined by the black box in Fig. 5.20(a) is enlarged in Fig. 5.20(b) and shows the thermal cut in greater detail. Results show the first application of a mechanical-magnetically controlled flexible catheter that, in combination with a customised diathermy tip, allows to perform a complete capsulorhexis on an *ex vivo* porcine lens capsule. The system guides the diathermy tip along a circular path with defined diameter while cutting the lens capsule thermally within a time duration of 60 s. The resulting edge is smooth and stable and shows no noticable radial tears. However, it is observed that the edges coil up slightly due to coagulation and resulting tissue shrinkage. This phenomenon was also observed by Klöti [123] during first experiments with high-frequency capsulotomy tools. When comparing the results shown in Fig. 5.20 to a capsulotomy performed using a commercially available diathermy tool, presented in [129], the thickness of the edge is similar. However, the automatically controlled procedure results in a more circular capsulotomy than the manual intervention, presumably due to non-smooth movement or tremor of the surgeon's hand.

(a)   (b)
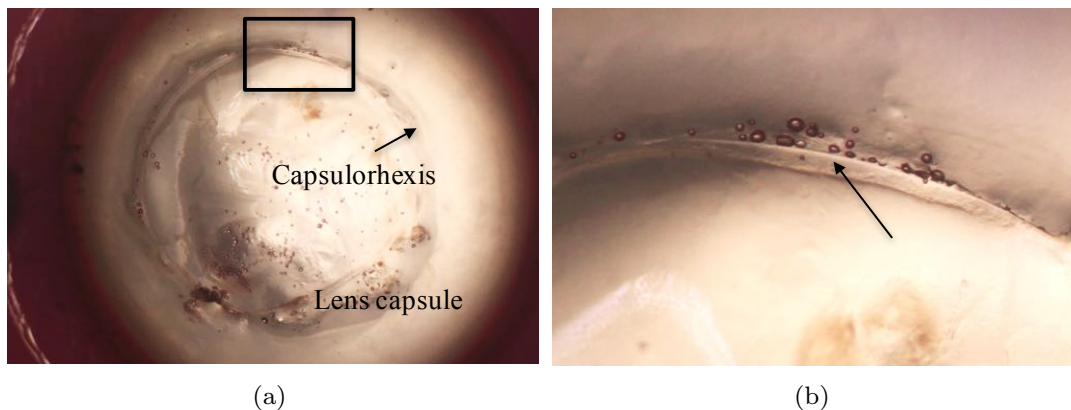
Figure 5.20: A capsulorhexis on an *ex vivo* porcine lens that was performed
with a customised diathermy tip on a magnetic-mechanical actuated flexible
catheter. The section inside the box (a) is enlarged in (b) and shows the
thermal cut (arrow) in more detail.

5.6   Conclusion

This chapter successfully demonstrates automated motion control for capsu-
lorhexis based on hybrid magnetic-mechanical actuation of a flexible magnetic
catheter. The longitudinal direction of the catheter is governed by a mechan-
ical catheter advancer, while the orientation of the catheter tip is controlled
by the electromagnetic manipulation system OctoMag. Vision and encoder
based closed loop control is implemented and guides the end-effector at the tip
of a flexible catheter along a continuous predefined path with high repeata-
bility and accuracy. Furthermore, the size and location of the capsulorhexis
can be predefined by the user. During the automated capsulorhexis process,
the lens capsule is thermally cut using a customised flexible diathermy tool.
Thermal cutting of the lens capsule is demonstrated through proof-of-concept
experiments on *ex vivo* porcine lens capsules. However, the capsulorhexis edge
may be smoothened by integrating a professionally fabricated diathermy tip to
the flexible body of the tool, such as the endodiathermy probe available from
Oertli Instrumente AG [125]. The demonstrated application of a magnetically
oriented catheter for thermal cutting of a lens capsule is fully automated and

shows reproducible control for a flexible catheter tip within short duration of time, thus, indicating the potential for fast and safe ophthalmic applications that potentially do not require excessive medical training.

Chapter 6

Remote Center of Rotation System for Intraocular Surgery

6.1 Robot-assisted Intraocular Surgery

This chapter presents the kinematics, mechanical and electrical design, fabrication, and experimental validation of a remote centre of motion (RCM) device for intraocular surgery. The system is designed to be combined with a magnetically guided catheter in the vicinity of an electromagnetic manipulation system, such as the OctoMag. Such a system combines the precise control and force sensing capabilities of a magnetically guided flexible tool with the stable and exact adjustment of the tool's shaft and the reduction of shear forces at the entry point to the eye in the sclera. Epiretinal membrane peeling as well as retinal vein cannulation (RVC) represent two of many possible candidates for robot-assisted ophthalmic surgery utilising an RCM mechanism in combination with an electromagnetic guidance system.

The mechanical design and fabrication of the system presented in this chapter was supported by Sean Lyttle during his Masterthesis and advised in collaboration with Roel Pieters. Christoph Ryan contributed to the development and evaluation of software and motion control throughout his Masterthesis.

6.1.1 Remote Center of Motion Mechanism

The center of motion of a robot or actuator is the point in space around which it rotates. If this point is fixed in space, not coincident with any of the robot links, and no physical revolute joint exists at this position, then this mechanism

is a remote center of motion robot [130]. An RCM can be achieved virtually by constraining the motion of a robot in software [35, 131] or physically by the manipulator's design [132]. A medical RCM robot allows a surgeon to make an injection or incision into tissue and then manipulate the end effector around a pivot point in a spherical configuration without enlarging the point of incision [133], hence, minimising shear forces.

6.1.2   Epiretinal Membrane Peeling

The epiretinal membrane (ERM) is a non-vascular cellular membrane that results in distortion of vision [134] often associated with past cataract surgery and retinal disease [135]. A study conducted in Australia in 2005 determined the prevalence of ERM in a random sample of the population aged 40 years and older to be 5.9% [136]. A common treatment technique for ERM is the removal of the vitreous humour during *pars plana* vitrectomy and the subsequent peeling of the epiretinal membrane utilising forceps.

6.1.3   Retinal Vein Cannulation

Retinal vein occlusion (RVO) is characterised by hardening of the retinal veins or the formation of blood clots therein. In 2008 an estimated 16.4 million adults were affected by RVO, with 2.5 million suffering from central retinal vein occlusion and 13.9 million from branch retinal vein occlusion [137]. Although many innovative treatment methods for central RVO have been suggested, no safe techniques exist at present [138]. One feasible approach is direct injection of tissue plasminogen activator (t-PA) into the affected retinal vein via retinal vein cannulation (RVC) [139, 140]. However, complications such as vitreous hemorrhage, retinal tear formation or retinal detachment have been observed after manual RVC [141]. RVC is a challenging procedure, as the surgeon must insert a needle with a diameter of 20 to 50 μm into a retinal vein with a diameter of 50 to 150 μm and stabilise it for several minutes [139]. During ophthalmic surgical procedures hand tremor with a root mean square amplitude up to 182 μm have been recorded [142].
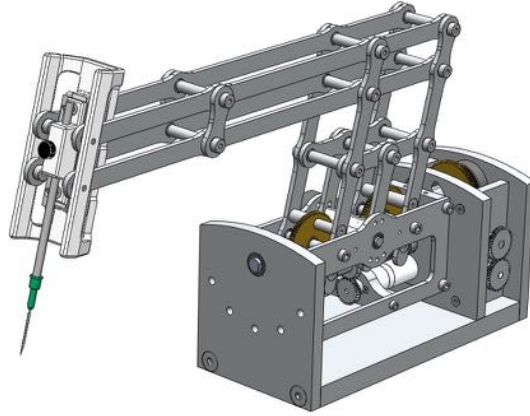
Figure 6.1: Concept design of a surgical device for intraocular experimentation exhibiting a remote center of motion (RCM).

6.2   Design of the RCM Mechanism

The RCM mechanism is designed according to its requirements, presented in Section 6.2.1, to assist in the treatment of ERM peeling or RVC, optionally in combination with a electromagnetic manipulation system. The mechanical, electrical, and kinematic design of the automated device for intraocular surgery, as well as its fabrication and assembly are presented. The concept design of the fully assembled mechanism is illustrated in Fig. 6.1. The robot depicted in this work is designed to be used in several applications in the human eye with interchangeable tools, but can also be adapted to assist in general medical interventions.

6.2.1   Procedure Based Requirements

The outer anteroposterior diameter of the human eye globe has an average diameter of 24.15 mm while the average internal diameter measures 22.12 mm [143]. As the robotic system is intended for ophthalmic interventions, its workspace should allow for manipulation of instruments inside the entire volume of a human eye that ranges from 6.5 to 7.2 mL [143]. In all ophthalmic surgical procedures in the posterior eye, an incision is made between 3.5 and

4 mm from the limbus (*i.e.* the *ora serrata*) to avoid damage of vital tissue and to insert an instrument through the opening. During robot assisted ocular surgery shear forces at the incision point in the sclera should be minimised. To account for this requirement, a mechanism is considered that mechanically restricts unwanted degrees of freedom (DoF) utilising a remote center of motion that pivots around a single point that coincides with the entry point to the eye.

To reach every point on the retina enclosed by the *ora serrata*, a surgeon requires a maximum incision angle of 45° from the normal to the sclera [144]. To perform RVC an available area on the retina of 60° around the center of the eye is required [132].

A system used to assist during surgery must easily integrate into the operating environment and offer good usability. A compact and lightweight design allows for accessibility and simple positioning of the system in close proximity to a patient's head. To provide ease of use, the system should permit quick and simple changing of different surgical instruments. It must provide the opportunity for teleoperated interventions that are controlled through an intuitive user interface by the surgeon.

Because the assistive device is intended for use in the human posterior eye, it must allow for interventions with high dynamic stiffness. The device should move along a given trajectory with minimal play and friction in the system. To assist in the treatment of epiretinal membranes, the stiffness of the system could be increased by rendering it non-backdrivable and by mechanically minimising the effect of backlash in the structure through the use of springs on the robot frame. Non-backdrivability offers the advantage that the end-effector of the robot does not move inside the eye, even when accidentally touched. In case of power failure, the system should allow for manual removal of an instrument from the eye. The device is required to achieve high precision in all DoF, preferably higher than human performance.

Future applications of the robot should allow for its use in conjunction with magnetically steered catheters [108]. Hence, it must be fabricated from nonmagnetic materials and should allow for easy integration with an electro-
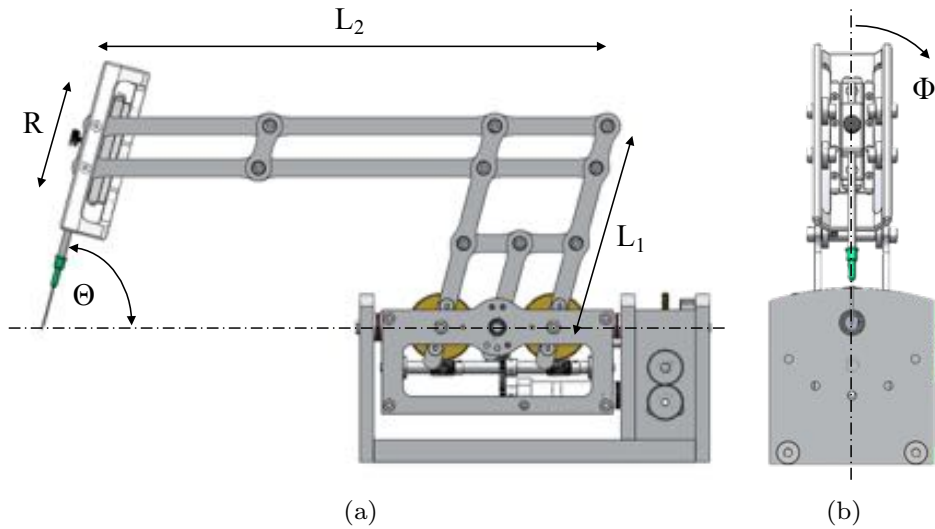
Figure 6.2: Sketch of the kinematic parameters, Θ, Φ, R, of the RCM mechanism exhibiting three DoF. (a) sideview, (b) frontview.

magnetic manipulation system, such as the OctoMag (Section 3.2).

6.2.2   Kinematic Design

The system's mechanical concept is a dual-parallelogram linkage with two DoF, namely roll (Φ) and pitch (Θ), combined with a linear actuator at the tip of the parallelogram structure, which adds an additional DoF, namely R. Thus, the robot has three DoF with a common mechanically constricted RCM. The general structure as well as actuated joints are sketched in Fig. 6.2.

6.2.2.1   Workspace Design

The workspace is designed, such that it fits the volume of a human eye and a maximum area of the retina can be reached during surgery. It is mechanically limited by possible collisions between individual links of the structure. For the system design the following joint limitations are derived in consonance with

the required range of motion

$$\Theta = [-50°, 50°] \tag{6.1}$$

$$\Phi = [-90°, 90°] \tag{6.2}$$

$$R = [0, 32.5 \text{ mm}] \tag{6.3}$$

A MATLAB simulation illustrates the theoretical workspace according to the derived joint limits. The theoretical workspace of the system in its final configuration is illustrated in Fig. 6.3(a) and projections on the xy- and yz-planes are shown in Fig. 6.3(b) and 6.3(c). The black sphere in the center of the workspace has a diameter of 24 mm and represents the volume of a human eye. The workspace is in the shape of a spherical wedge that is spanned by the ranges of the rotary joints Θ and Φ, and the workspace radius is the range of prismatic joint R. For the final conception, with Φ spanning 180°, the theoretical workspace volume can be derived as

$$V = \frac{2}{3}R^3\Theta \tag{6.4}$$

and is 39.9 cm^3 for the design, which easily fits the required workspace.

6.2.2.2   Forward and Inverse Kinematics

To simulate the kinematics of the robotic device, a model is derived in MATLAB that calculates the coordinates of the RCM and end-effector in relation to the absolute values for angles Θ, Φ and R, *i.e.* the forward kinematics. Furthermore, the program allows the user to define a trajectory inside a spherical model of a human eye with a diameter of 24 mm. After the input of a predefined trajectory, the algorithm calculates the robot's inverse kinematics and determines the required actuation of joint angles Θ, Φ and the linear motion R. Figure 6.4(a) illustrates a trajectory consisting of two lines and a circle inside the human eye model. The red asterisk depicts the static RCM. The required joint angles for the trajectory are illustrated in Fig. 6.4(b).
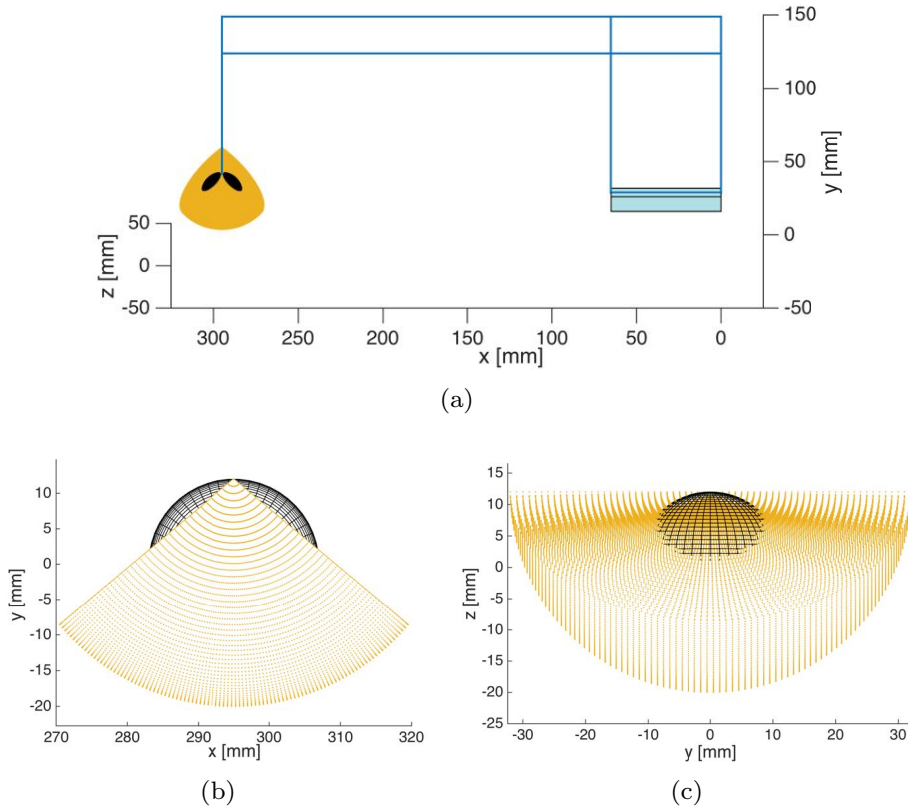
Figure 6.3: (a) The model shows the robot link positions and calculates the full workspace of the mechanism. Projections of the workspace on the (b) xy-plane and (c) yz-plane.

6.2.3   Mechanical Modules

Both the Θ and Φ axes consist of worm gear drive systems that transfer rotary motion orthogonally from one shaft to another while preventing motion transfer in the tangential direction, thus, rendering the system non-backdrivable. During the design process care was taken to eliminate backlash in the structure. The final design is comprised of four modules that include the base, the chassis, the double parallelogram linkage and the end-effector, as illustrated in Fig. 6.5(a) to 6.5(d). The base module supports and drives the roll axis of the robot with a geared DC motor (DCX16, Maxon Motor AG, Switzerland). The chassis module houses the drive assembly for the pitch axis of the system. It
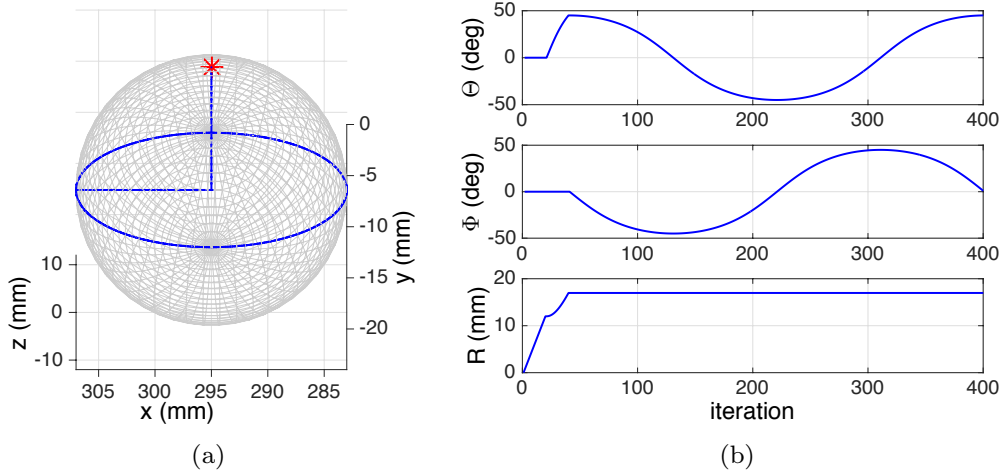
Figure 6.4: (a) Trajectory planning inside human eye model with diameter 24 mm. (b) MATLAB simulation calculating joint angles for a given end-effector trajectory, *i.e.* inverse kinematics.

also contains a DC motor (DCX22) that orients the double parallelogram module. This module supports the end-effector, comprising the R axis of motion, which is driven by a linear piezoelectric actuator (SLC-2460, SmarAct GmbH, Germany).

6.2.4   Fabrication

The robot is primarily fabricated from aluminum due to its high strength-to-weight ratio and low cost. General purpose 6061-T6 alloy was selected for the base and the chassis, while high-quality aircraft grade 7075-T3 was used for the parallelogram linkage structure due to its high stiffness. To reduce the overall weight, all shafts are fabricated from general purpose aluminum alloys while bearings and screws are stainless steel. All worms used in the design are stainless steel and all worm gears are brass to prevent excessive friction and wear. Computerised numerical control (CNC) equipment was used for manufacturing processes to ensure tightest possible center-to-center tolerances between holes. Holes, critical for bearing alignment, were cut with wire electric discharge machining (EDM) to guarantee tight tolerances and good press-fits.
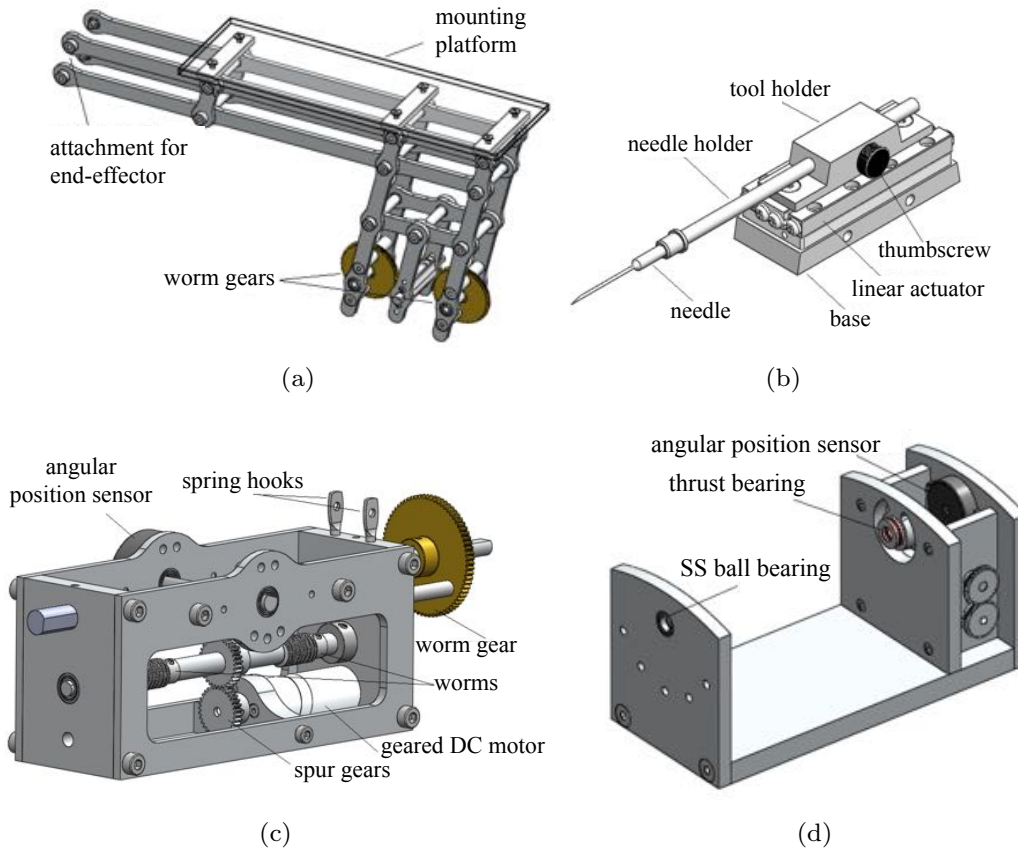
Figure 6.5: Design details of the four mechanism modules (a) Double parallelogram linkage, (b) End effector, (c) Chassis module, (d) Base module.

The 7075 aluminum linkage parts were cut with waterjet and subsequently polished and reamed. Figure 6.6 shows the fully assembled system.

6.3 System Electronics and Software Design

The RCM mechanism's electronics and software are designed for closed loop motion control. The system electronics include redundant sensors, which sense the system state, as well as motion controllers. Software has been implemented to integrate all sensors and provide motion commands to the actuators.

Figure 6.6: Fully fabricated and assembled robotic device for intraocular experimentation exhibiting a remote center of motion.

6.3.1   System Electronics Architecture

The flow of logic and communication between all integral components of the robot's electrical system is sketched in Fig. 6.7. The pitch (Θ) and roll (Φ) axes are driven by Maxon motors with integrated gearboxes and encoders. Both motors incorporate 44:1 planetary gear heads and 256 count quadrature optical encoders and are driven by using identical Maxon EPOS 70/10 positioning and velocity controllers. The EPOS controllers receive a desired position or a constant velocity from the Linux PC via a RS232 connection. The internal feedback loop is completed when a motor's encoder determines the motor state and informs the EPOS controller that moves the motor. The end-effector orientation is tracked by an inertial measurement unit (IMU, MPU-6050, InvenSense Inc., USA), which is attached at the end-effector. Additionally, two cameras (DigiMicro, dnt GmbH, Germany) provide images of the end-effector to the Linux PC for visual tracking. The R axis of motion is actuated with a linear piezoelectric actuator (PEA) that is driven by a controller with an internal closed loop control (HCU-3DM, SmarAct GmbH, Germany). The PEA can resolve its position with sub-μm accuracy and features a minimum step
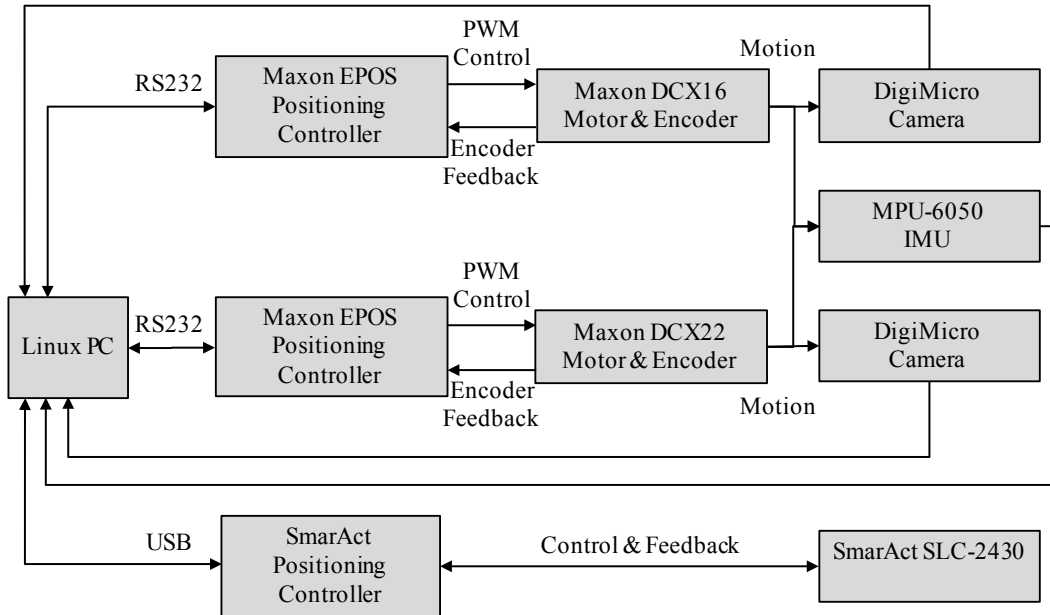
Figure 6.7: System architecture showing the logic and communication between rotary/linear positioners, controllers, and sensors as well as their feedback signals.

size of 50 nm. The PEA controller receives instructions either from the Linux PC via USB, or alternatively from a human operator via a joystick. Position feedback is transferred from the PEA back to the controller and, thus, to the computer.

6.3.2 Software Design

The linux computer includes software, written in C++ in the ROS (Robot Operating System) environment. It utilises the *EposManager* package to send motor commands to the EPOS controllers and receive state information from the motors. Thus, standard commands are used for absolute or relative positioning, and for homing of the motors. The ROS environment has the advantages of being highly modular and the availability of several open source code packages and libraries. In the ROS environment, *nodes* are defined as standalone programs that perform computations, *i.e.* a software module. Several *nodes*
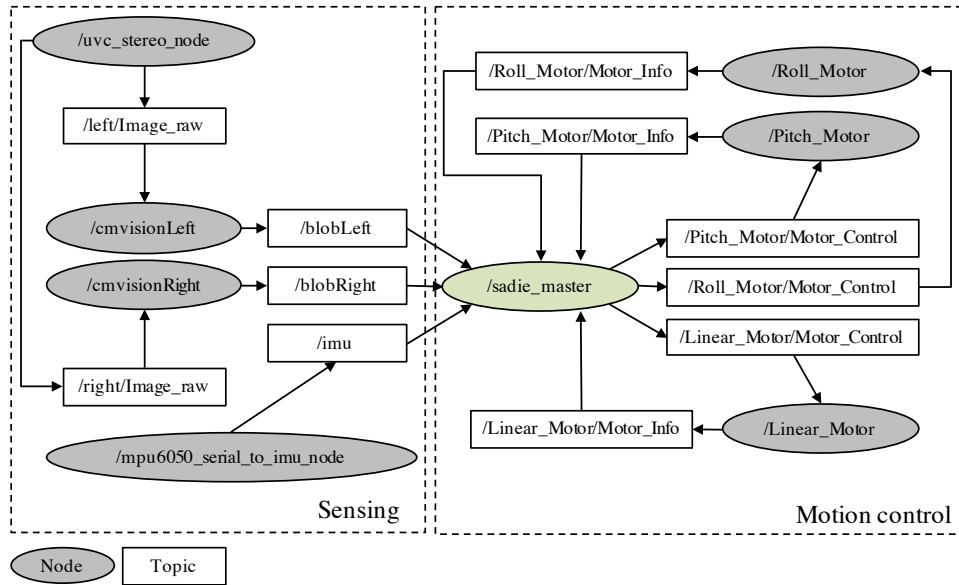
Figure 6.8: Structure of the software written in C++ in the Robot Operating
System (ROS) environment, showing nodes and topics.

communicate via *messages*, which are strictly typed data structures, *e.g.* integers, floats, booleans, or arrays. *Messages* only define the type of information exchanged between *nodes*, whereas *topics* define the unique path of communication. Thus, *nodes* can send or receive a *message* by subscribing to a given *topic*.

Figure 6.8 illustrates the information pathways through *nodes* and *topics* of the RCM mechanism. The figure shows the central *node* /sadie_master that receives state information about the mechanism from computer vision and the inertial measurement unit (IMU). For vision feedback, the *node* /uvc_stereo_node provides raw images from the two cameras to the *nodes* /cmvisionLeft and /cmvisionRight, which make use of a blob tracker to supply the coordinates of the tracked object to the master *node*. The *node* /mpu6050_serial_to_imu_node reads the state information from the IMU and supplies those to /sadie_master. The master *node* includes the control algorithm and computes control commands, which are sent to the motor *nodes* /Roll_Motor, /Pitch_Motor and /Linear_Motor. The motor states are fed back to the master *node*.

6.4   Experimental Validation of the RCM System

To validate the motion characteristics of the RCM system and investigate its potential for surgical interventions in the posterior eye, experiments are performed. A first set of experiments characterises the accuracy of the end-effector tip at several joint angles Θ and Φ. In a second set of experiments the end-effector follows a predefined trajectory, and the motion accuracy is analysed.

6.4.1   Color Tracking of End-Effector Tip

During experiments, a needle equipped with bright orange coloured beads is attached to the end-effector for color tracking of the tip. Vision tracking of the tip is performed to validate the angular measurements from the IMU. Two orthogonal cameras observe the motion of the needle and the x- and y-positions of individual orange beads are tracked using the ROS package *cmvision*, as described in Section 6.3.2.

To analyse the precision of the color tracker, a single stationary orange bead is tracked for 150 seconds by both cameras. As illustrated in Fig. 6.9, the tracker is subject to noise with maximum deviation of ± 1 pixels during tracking. As color tracking of the beads is dependant on changing light conditions in the environment, the incoming light intensity is controlled throughout experimentation.

6.4.2   Experimental Characterisation of Joint Motion

A first experiment characterises the RCM mechanism's end-effector orientation and compares the result to the targeted end-effector rotations. The roll and pitch angles of the RCM mechanism's end-effector are redundantly measured using the IMU and visual color tracking. The orientation and acceleration of the system are measured by the IMU and provided to the computer via a serial connection, as described in Section 6.3.2. For color tracking of the end-effector and the subsequent derivation of pitch and roll angles, a straight needle with two orange beads is attached to the end-effector. The x- and y-positions of
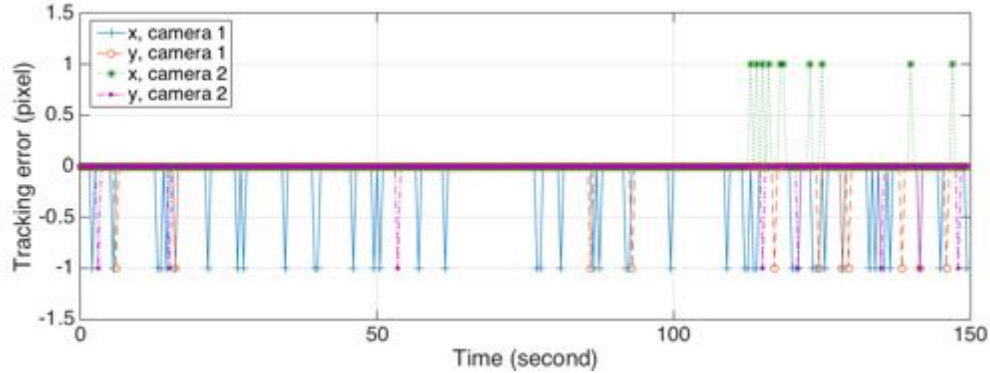
Figure 6.9: Analysis of the color tracker's accuracy while tracking a single orange bead for 150 seconds. The maximum deviation of the color tracker is found as ±1 pixels.

the beads are visually tracked to geometrically deduce pitch and roll of the end-effector.

During experiments, the RCM mechanism is controlled for combinations of pitch and roll orientations. First, the roll is held constant for angles in the range between $-25°$ and $25°$ (step size of $5°$), while the pitch angle is varied in a range between $-45°$ and $35°$ (step size of $5°$) for each roll angle. Each experiment is repeated three times. The angles measured by the IMU and the color tracker are automatically saved into a text file for post-processing. A similar experiment is performed with the pitch held constant at angles between $-25°$ and $25°$, while the roll angle is varied between $-50°$ and $50°$ (step size $5°$).

To analyse the joint motion of the RCM mechanism, post-processing of the measured data is performed in MATLAB. The errors between the targeted angles and the measured values are derived by both measuring techniques. Several matrices are plotted that show the orientation errors for various combinations of pitch and roll on a grid ranging from $-25°$ to $25°$ for both, pitch and roll angles. Figures 6.10(a) and 6.10(b) illustrate the error matrices for measurements performed with the IMU for pitch and roll angles, respectively. Figures 6.10(c) and 6.10(d) show the orientation error for pitch and roll measured with

114

(a)

(b)

(c)

(d)
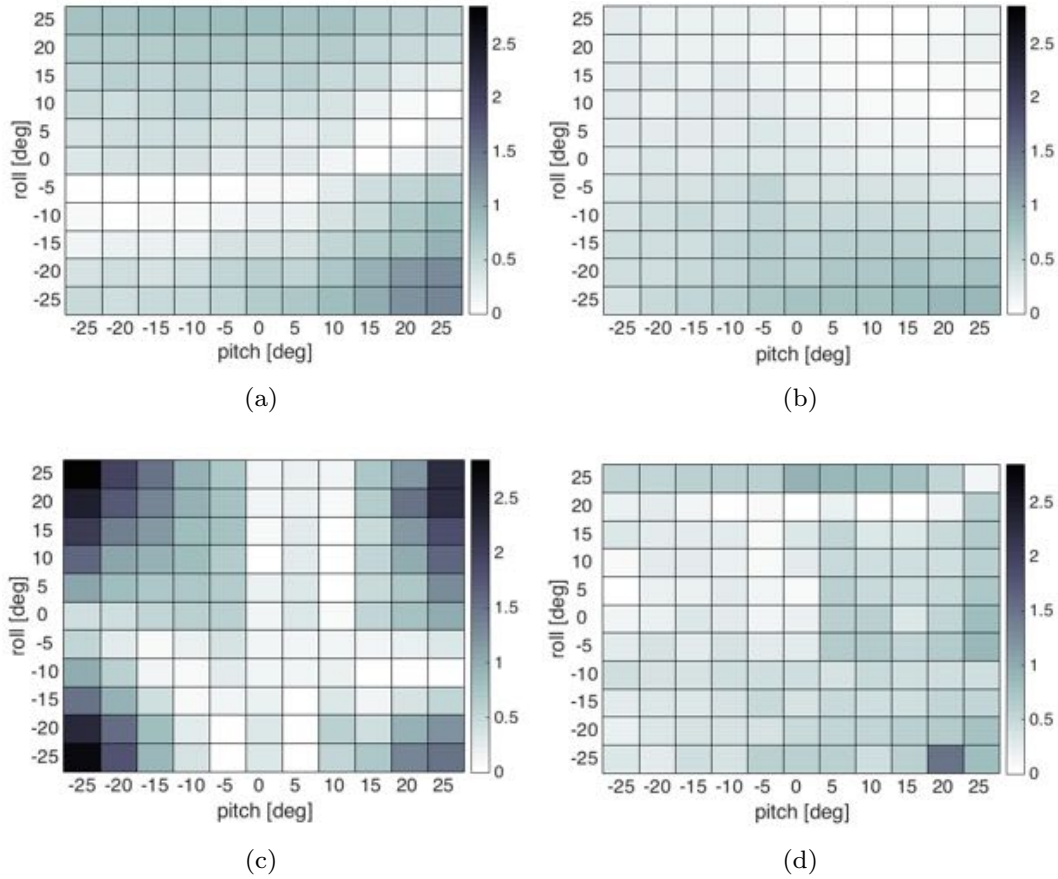
Figure 6.10: Error matrices for measured end-effector orientation. (a) Pitch
error measured with IMU, (b) roll error measured with IMU, (c) pitch error
measured with visual tracking, (d) roll error measured with visual tracking.

visual tracking. In general, the errors measured using vision tracking are larger
compared to those measured with the IMU. Presumably, this difference is due
to the noise of the color tracker, derived in Section 6.4.1. Furthermore, the
figures show that orientation errors tend to increase for large pitch and roll
angles and are small for small set values. This trend becomes especially ob-
vious in Fig. 6.10(c), which also shows the largest overall errors. The mean
pitch angle error, as measured with the IMU, is $0.46°\pm0.28°$ (with a maximum
of $1.36°$), while the mean roll error is measured with the IMU as $0.34°\pm0.22°$
(maximum of $0.89°$). Measuring the angles using visual tracking results in

slightly larger orientation errors with a mean pitch angle error of $0.70°\pm0.65°$ (maximum of $2.85°$) and a mean roll angle error of $0.41°\pm0.23°$ (maximum of $1.49°$). However, as the noise of visual tracking was found to be ±1 pixels, using cameras with higher resolution may decrease the visually measured error of the end-effector orientation.

6.4.3   Trajectory Following Experiments

Another set of experiments evaluates the RCM mechanism during trajectory following. To visually track the end-effector motion, an orange bead is attached to the end-effector close to the RCM of the mechanism. By slowly moving the actuators and observing the bead, the RCM of the system is found at a point with minimal motion, this bead position is assumed as its initial position. Both cameras are calibrated using a checkerboard calibration algorithm provided by the *camera_calibration* package in ROS.

First, the camera conversion factors for conversion of pixel values to spatial coordinates (in mm) are determined for both cameras. An initial value is determined by observation of an object with known dimensions in each cameras' field of view. The initial conversion factor (in mm/ pixel) is used during an initial targeting experiment. The end-effector is moved to individual target points on a grid before being retreated to its initial position, while being visually tracked. The conversion factors for both cameras are derived by an optimisation routine that minimises the error between targeted and tracked points. The conversion factors are found to be $0.100\,$mm/pixel for the camera tracking the x-coordinate and $0.115\,$mm/pixel for the camera tracking y- and z-coordinates of the orange bead. These conversion factors are later used for trajectory following experiments.

To evaluate trajectory following, a trajectory is pre-planned in MATLAB (Section 6.2.2) and uploaded to the system. The RCM mechanism is controlled to follow the trajectory, while the end-effector is visually tracked. The resulting coordinates are saved to a text file for post-processing in MATLAB. Several

(a)

(b)

(c)

(d)
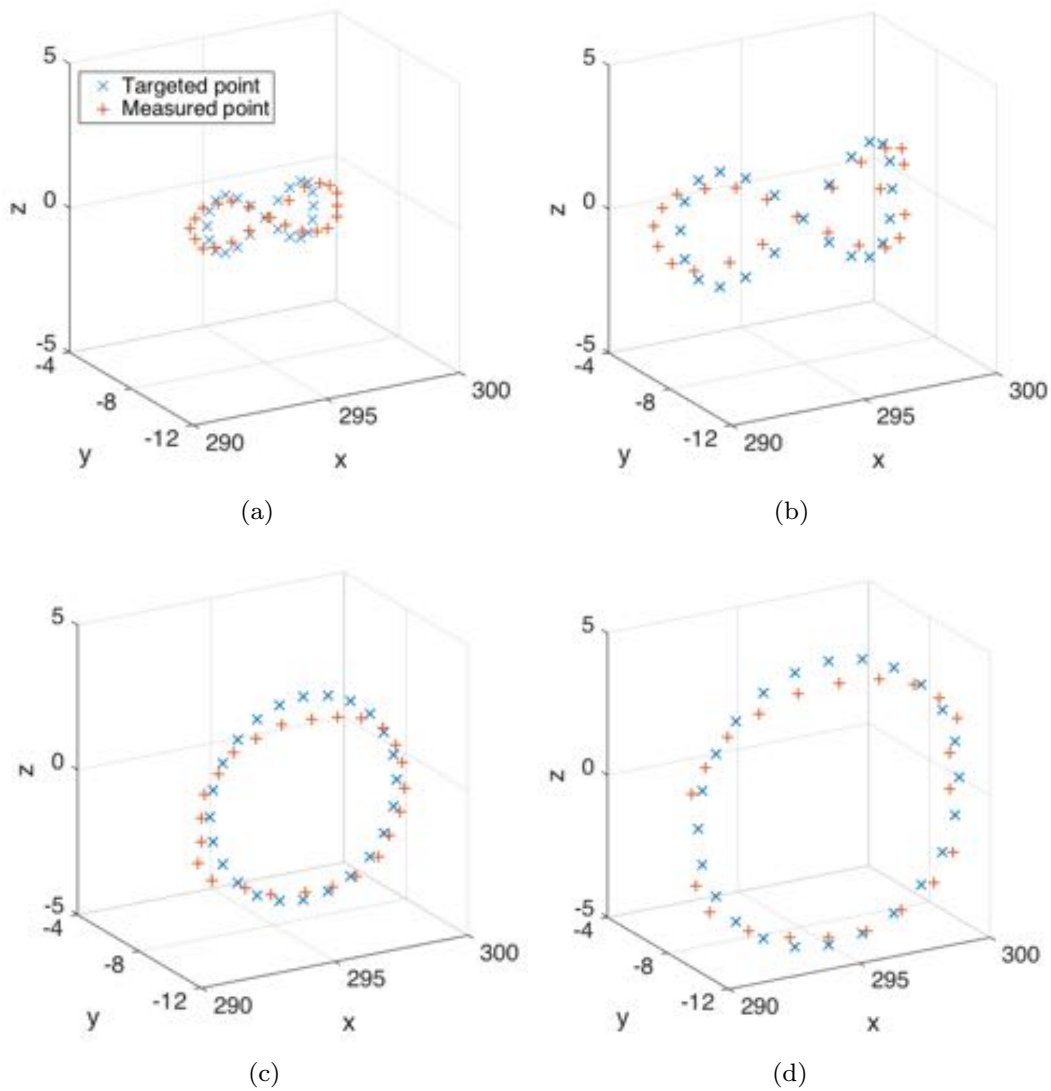
Figure 6.11: Several trajectories with different size and shape are followed with the RCM mechanism's end-effector. The graph shows the targeted ($\times$) and the visually measured ($+$) trajectories.

trajectories are executed during experiments, which exhibit different sizes and shapes, such as a figure-eight trajectory and a circular path. Figure 6.11 shows the targeted ($\times$) and measured waypoints ($+$) of the trajectories that the RCM mechanism's end-effector approaches during experimentation. For each trajec-

Table 6.1: Mean radial error and standard deviations for investigated trajectories during experimentation with the RCM mechanism.

Trajectory	Mean radial error [mm]	Standard deviation [mm]
Small figure-eight	0.56	0.15
Large figure-eight	0.60	0.28
Small circle	0.57	0.21
Large circle	0.70	0.17

tory the mean radial error ϵ_{rad} (in mm) is calculated from the visually tracked spatial errors in x, y, and z-directions, as

$$\epsilon_{rad} = \sqrt{\epsilon_x^2 + \epsilon_y^2 + \epsilon_z^2}. \tag{6.5}$$

The mean radial errors and their standard deviations are summarised for all evaluated trajectories in Table 6.1. The mean errors all show sub-millimeter accuracy of the RCM mechanism's end-effector during trajectory following. However, noise from the color tracker presumably influences the measured results. Using cameras with higher resolution or utilising the IMU for closed-loop control during trajectory following may increase the mechanism's measured precision.

6.5   Conclusion

This chapter demonstrated the development and experimental validation of an assistive system for intraocular surgery. The fully assembled mechanism has a remote center of motion allowing it to pivot around a single point. The robotic system exhibits high precision and stiffness due to its non-backdrivability. It is lightweight, compact, and can be integrated into medical systems that employ magnetic fields, because the mechanism is assembled primarily from nonmagnetic materials. Experiments have been performed to characterise the joint motion using redundant sensors and to evaluate the mechanism's ability to follow a predefined trajectory. The mechanism shows sub-millimeter accuracy

during path following.

Due to its stiffness and the kinematics design, the RCM mechanism is intended to assist in ophthalmic surgery in the posterior eye. During surgery the RCM should be coincident with the incision point in the sclera to minimise shear forces between a medical instrument and the structures of the eye.

Chapter 7

Automated Intravitreal Injection Robot

Neovascular age-related macular degeneration (AMD) is the primary cause of blindness in industrialised countries [11]. This disease is characterised by uncontrolled vascularisation and degenerative lesions in the retina and causes loss of central vision. Since the approval of the first intravitreally applied drugs for the treatment of AMD [14, 15], intravitreal injection has become one of the most frequently performed surgical procedures in ophthalmology with more than 4 million injections worldwide in 2014. The demand for intravitreal therapy (IVT) of various drugs including mostly vascular-endothelial-growth-factor (VEGF) inhibitors evolved dramatically over the past decade. Especially the demand for IVTs to treat the chronic diseases AMD and diabetic maculopathy/retinopathy is severe and is going to increase in the foreseeable future [16]. In this chapter, an assistive device for intravitreal injections is proposed to render IVTs more time and cost efficient, while increasing safety for the patient. The system allows for precise and safe injections into the eye, but is still controlled by the treating physician [145].

The work presented in this chapter was supported by several students and colleagues. Mechanical design of the system was developed in collaboration with Christoph Bollinger and Sean Lyttle, while Daniel Lehmann, Samuel Ruckstuhl, Ken Sutter and Sandro Kränzlin contributed to software and vision system development throughout their corresponding Master- and Semestertheses. Stephan Michels and Matthias Becker contributed substantially to conception of the system and acted as medical advisers throughout the project.

7.1   Intravitreal Therapy

In recent years, pharmaceutical companies discovered IVTs as a new area for investment and development due to the fast growing market for ophthalmic drugs, which achieve more than US$ 1 billion revenue annually. Two large groups of patients needing IVTs have been identified. The first group consists of patients, who seek treatment for neovascular AMD, in western industrialised countries but also increasing numbers in Asia. Increasing life expectancy leads to a further increase in the prevalence of neovascular AMD worldwide [146]. An increasing number of patients suffer from diabetic retinopathy or maculopathy due to increasing occurrence of diabetes mellitus throughout the world. The comparative diabetes prevalence reaches up to 8.3% in India, up to 10.0% in China or Russia, and up to 13.8% in Mexico [147]. More than 50% of diabetic patients develop a diabetic retinopathy or maculopathy within 10 to 20 years after disease diagnosis [148].

Table 7.1: Requirements for an automated assistive device for intravitreal injections.

	Requirements
Safety	Reduction of bacterial contamination (sterilisability)
	Position accuracy $< 100\,\mu\text{m}$
	Orientation accuracy $< 1°$
	Automated recognition of patient and eye
	Eye tracking at $> 15\,\text{Hz}$
	Stable fixation of the patient's direction of gaze
	Control based on anatomic landmarks
	Possibility to save injection history
Cost/Time Efficiency	Remotely controlled system
	Possibility to inject several different drugs
	Automated documentation of procedure
Usability	Lightweight ($<5\,\text{kg}$)
	Audio-visual communication system
	Located in an operating or designated injection room

More intravitreal drugs for an expanding spectrum of ophthalmic diseases are likely to be introduced to the market in the near future, thus, severely raising the number of IVTs and the related health care costs. The access to IVT further increases with the expiration of the patent of the popular approved anti-VEGF drug ranibizumab, starting in 2017. This may open the market for generics. In addition, the off-label use of other VEGF inhibitors, such as bevacizumab and ziv-aflibercept (both approved for cancer treatment), is very common in some countries (*e.g.* USA), despite serious problems due to compounding. However, the cost of off-label drugs is up to ten times lower than that of approved agents [149]. The increasing demand of IVTs raises pressure on reducing the compensation for intravitreal injections, which are mostly performed by medical doctors [150]. Physicians and hospitals are struggling to manage an increasing workload, while obtaining reduced reimbursement. This situation calls for a radical change in the way ophthalmologists deliver IVTs. A challenge arises as the IVT needs to remain under the control of physicians, but costs are to be minimised. Thus, the time the physician spends performing IVTs has to be significantly reduced, while maintaining or even increasing safety and precision of the IVT.

7.2   Robot-Assisted Injection Procedure

The assistive system for automated intravitreal injections was designed according to several requirements concerning patient and physician safety, cost and time efficiency, and usability of the system as summarised in Table 7.1. To ensure safety of the system, it must be sterilisable and the precision of the injection must be high with position accuracy of the needle of less than $100\,\mu\text{m}$ and orientation accuracy less then $1°$. The patient and eye must be correctly identified and the pupil of the treated eye must be tracked at $> 15\,\text{Hz}$, such that the injection procedure can be stopped in case of patient motion. To prevent eye motion, the system should include a stable fixation of the patient's direction of gaze. The position control of the system should be based on anatomic landmarks of the patient to account for anatomical differences. To prevent multiple injections into the same location, which might cause thinning of the sclera, the

injection history of previous injections and their locations should be saved for each patient. In order to render the assistive device attractive to the market, time and cost efficiency must be provided by reducing the time spent by the physician to a minimum of one to two minutes per injection. Thus, the system should allow for automated documentation of the procedure and the possibility to inject different drugs into the patient's eye. Also, the system should be remotely controlled, such that one physician can supervise several patients at the same time. To ensure easy handling and usability of the system, it must allow for quick positioning over the patient's face by a nurse, constraining size and weight. To account for guidelines [150], the injection system must fit into an operating room or a defined injection room. Audio-visual communication between patient and doctor should be included to increase patient acceptance.

Prior to the injection procedure, the patient is prepared by a nurse and the system is coarsely positioned over the patient's head. This is followed by fine positioning of the system, such that the eye is centred in the system workspace. An iris scan identifies the eye, and the injection point is specified. The injection process includes the positioning of the needle over the eye, followed by injection and needle removal. The process is completed by automated data documentation. The injection procedure is summarised in the block diagram in Fig. 7.1.
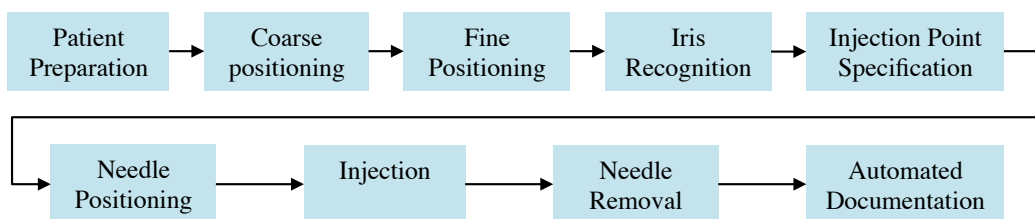
Figure 7.1: Outline of the automated injection process.
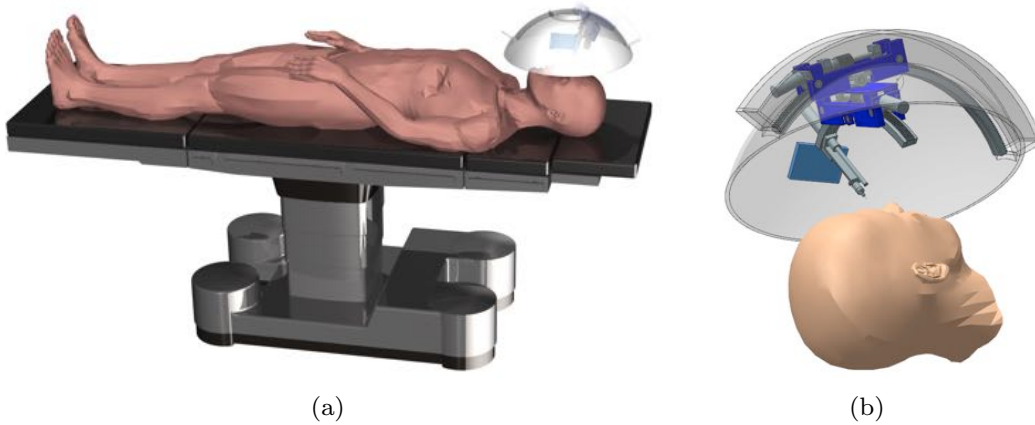
Figure 7.2: (a) The assistive device for intravitreal injection is coarsely positioned over the patient's head with a passive arm and locked into position. (b) The positioning module fine positions the system and the injection module allows for orientation of a syringe and injection of medication into the eye.

7.2.1   Preparation and Positioning

Prior to the intravitreal injection procedure the patient is prepared by a nurse according to the standard of care. The nurse gives local topical anaesthetics, spreads the eyelids using a lid speculum, and disinfects the eye. The nurse then manually positions the system coarsely over the patient's head by moving the passive arm into position and locking the joints. The system is illustrated hanging over a patient's head in Fig. 7.2(a). During the injection process, a top and a side camera continuously take images of the targeted eye. An eye tracking algorithm outputs the relative position and orientation of the treated eye. During fine positioning the system is centred over the eye in three-dimensional space using the positioning module, as outlined in Section 7.3.2. The calibrated cameras are used as feedback for the control loop.

7.2.2   Iris Recognition

The human iris offers a unique, stable pattern, which was shown suitable for person and eye identification [151]. Thus, automated iris recognition of the

patient's iris has been implemented into the system for safety. In daily practice, human error may lead to injections into the wrong eye, *e.g.* left instead of right, or the wrong patient, *e.g.* two patients with the same or a similar name. If the wrong medication or a different dosage of the drug is injected, treatment of the eye's disease may not be optimal. Thus, an iris scan was implemented, that is executed after initialisation of the injection procedure. The algorithm compares the iris to previously stored patient images in a database. Only if the iris is recognised as the right patient and eye, the injection process is started.

The iris recognition algorithm initially acquires an image of the eye under near infrared illumination, thereby reducing specular reflections and revealing the complex features of the iris pattern. Subsequently, the pupil and iris are detected utilising the intensity gradient at the boundaries of the latter. The iris is isolated from the image and converted into a rectangular form by applying a coordinate transformation. Specular reflections in the iris are filtered by thresholding the image and can be ignored during further analysis. Convoluting the unwrapped iris with a Gabor filter results in a binary iris code [152], that can be compared to the saved image codes in the database. In a next step, the degree of similarity of two codes is determined by deriving the Hamming distance as the ratio between disagreeing bits to the total number of bits in the binary codes.

7.2.3   Intravitreal Injection

The assistive device automatically suggests a point for safe injection that lies within a range of 3.5 to 4 mm from the limbus and within an angle of $\pm 80°$ on the temporal side of the eye, as illustrated in Fig. 7.3. This region is chosen to avoid injecting into the crystalline lens of the eye on the one side and the retina on the other, as seen in Fig. 7.3(a). The pre-chosen injection position can be altered manually by the treating physician on an user interface (UI). When all changes and data are submitted, the ophthalmologists initiates the injection procedure on the UI.
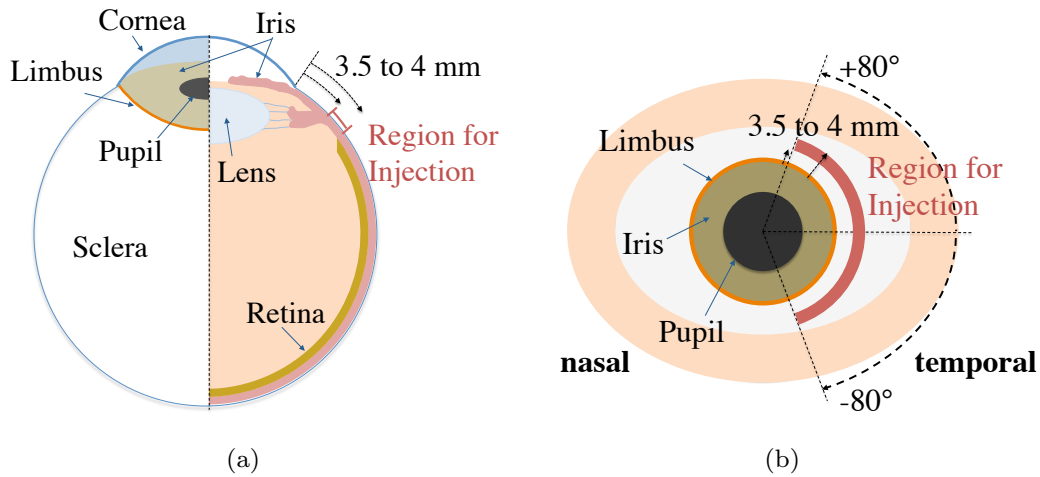
Figure 7.3: (a) The safe region for intravitreal injection spans between $\pm 80°$ from the horizontal on the temporal side of the eye with a radial distance of 3.5 to 4 mm from the limbus.

7.2.4   Patient Data Documentation

A Swiss survey shows that the average time a physician spends on documentation and administrative tasks increased from 15.8% in 2011 to 17.1% in 2013 [153], leaving less time for patient interaction. In practice, the average time for one intravitreal injection process, including preparation and documentation time, is approximately 10 minutes, of which the actual injection only takes one to two minutes. To decrease the time needed for documentation, a system is implemented that allows to directly save a patient's personal and medical data into a database. These data may include the patient's name, date of birth, patient number, as well as his/her condition, suggested treatment, type and amount of injected drug. After each intravitreal injection process the physician can submit all changes made to the patient database, where information is saved as binary code to account for storage space. Storing patient data in a database has the advantage that information is made available and searchable throughout the injection process efficiently.

7.3   System Design

The proposed device consists of two modules, the positioning module used for fine positioning of the device over the eye, and the injection module for the injection process. To inject a needle into the eye, 5 degree of freedom (DoF) motion is required, *i.e.* x-, y-, and z-translations, and two rotations (pitch and yaw of the injection needle). However, the proposed system is overactuated with a total number of 7 DoF. Decoupling the positioning from the injecting process allows for better controllability and higher precision.

7.3.1   System Architecture

The elements of the system architecture are categorised into the imaging system, the main computer including algorithms, and the injection system, as illustrated in Fig. 7.4. The imaging system consists of the user interface, the top and side camera for image acquisition and an infrared illumination system. The main computer includes software, written in C++ in the ROS (Robot Operating System) environment, for iris recognition, continuous eye tracking, position control of the injection system, and data documentation and collection. The injection robot hardware consists of the injection and positioning modules. The injection module includes three DC motors and corresponding controllers (EPOS2 24/2). The positioning module consists of three linear and one rotational stage and their corresponding servo controllers. To ensure safety for the patient and the physician, several safety features have been integrated, such as a *Stop* button on the user interface, a kill switch, continuous eye tracking for recognition of fast eye movement, and iris recognition for identifying patient and eye.

7.3.2   Positioning Module

The positioning module consists of a cartesian 3 DoF stage (Thorlabs Inc., USA) with a travel range of 50 mm each, and an additional rotational DoF with continuous 360° rotation. All of these drives are powered by DC servo motors. Position measurements for the linear stages are provided by hall-effect
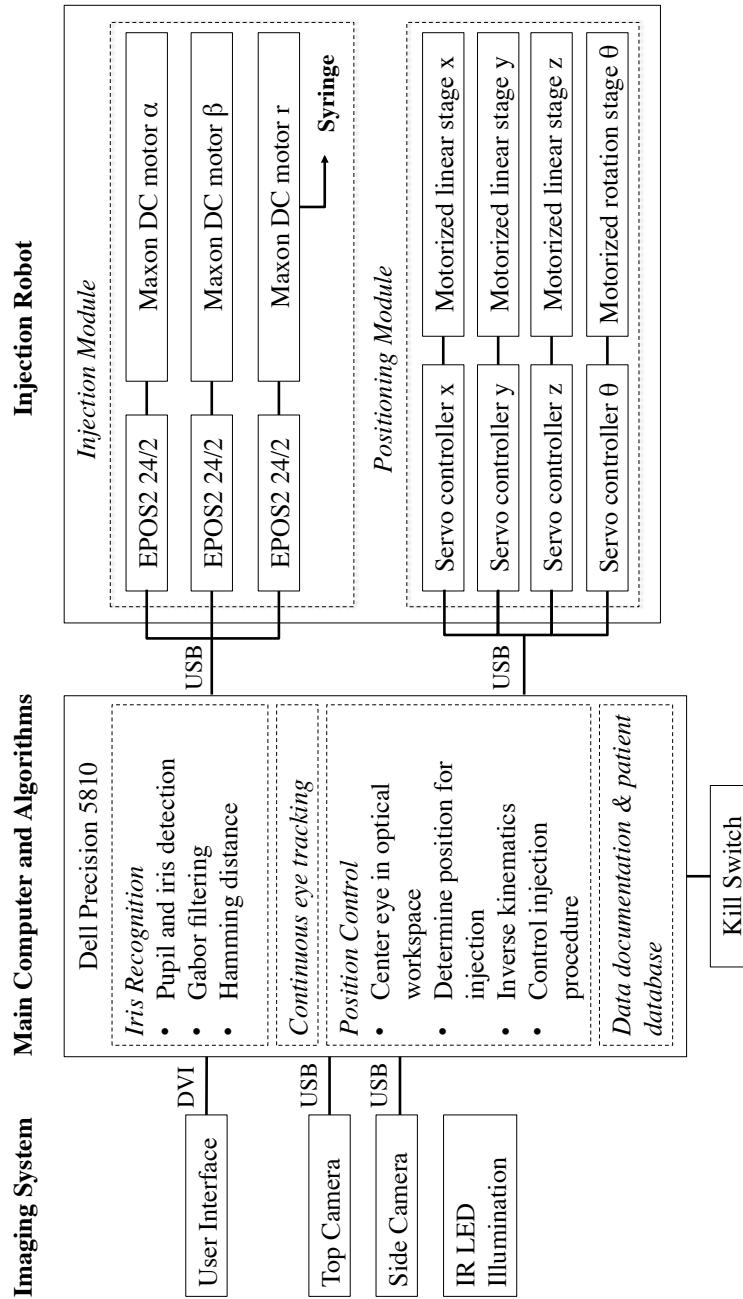
Figure 7.4: The system architecture design, including the imaging system, signal processing, and the injection robot control.

incremental encoders with 512 counts per revolution. Due to a planetary gear reduction ratio, the theoretical minimum linear displacement of the lead screw per encoder count is 29 nm. The minimal incremental motion of the rotary stage is 2.19 arcsec, which is equivalent to 0.6×10^{-3} degrees. After the entire system has been coarsely positioned over the patient's face by a nurse, an eye tracking algorithm detects the eye and the positioning module centres the injection module.

7.3.3   Injection Module

The injection module is suspended from the positioning module and consists of two rotary DoF (α, β) and one translational DoF (r). To increase time efficiency and to account for hygiene, a pre-filled syringe [154] with connected injection needle is directly clipped into the end-effector. An additional actuator allows to push on the syringe's lever to deliver the medication through the needle into the eye. The injection module consists of two arcs (α, β), which allow to pivot the end-effector around the centre of the retina at the back of the eye, *i.e.* the macula. The two rotational DoF are actuated with two DC motors (Maxon Motor AG, Switzerland) with a planetary gear box. Rotary incremental encoders are connected to the motors, which allow for control using an internal controller, supplied by the manufacturer. The theoretical resolution of rotation along the two arcs in the injection module are derived as 5.0×10^{-5} degrees per count and 6.8×10^{-5} degrees per count, respectively. Presumably, the precision is lowered during actuation due to backlash in the mechanical system. The linear stage (r) of the injection module is driven by a DC motor (Maxon Motor AG, Switzerland) with a mounted spindle gear rotating a lead screw with a 0.5 mm pitch. Position measurement is provided by an encoder with 100 counts per revolution, resulting in a theoretical resolution of 1.25 μm. All motors are controlled with Maxon EPOS2 24/2 position controllers.
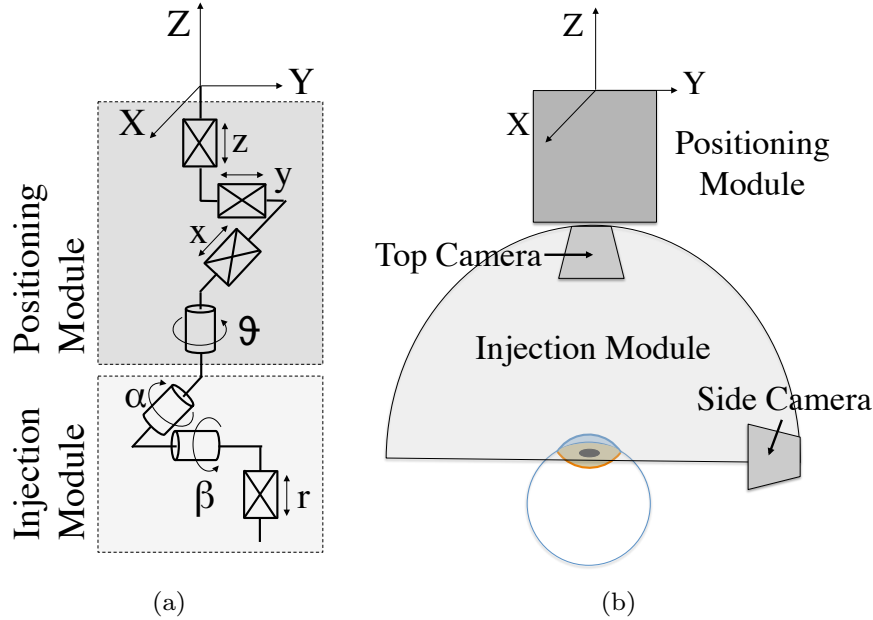
Figure 7.5: (a) Kinematics model for the assistive injection system, including the positioning (x, y, z, θ) and the injection module (α, β, r). (b) Vision system consisting of two near-infrared cameras (top, side) for tracking, iris recognition, monitoring.

7.3.4   Kinematics

Figure 7.5(a) illustrates the kinematics of the assistive injection system, divided into the positioning (x, y, z, θ) and the injection module (α, β, r). The workspace of the positioning module has been designed to fine position the injection module in order to account for error in manual coarse positioning. Its workspace is derived as a cylinder with height of 50 mm and diameter of 70.7 mm. Thus, the workspace volume of the positioning module is given by 196.35 cm^3.

In the system, the α-arc is shifted by an angle from the vertical plane and has a radius of 170 mm. The gear housing, including the subsequent β-arc and r-stage, moves along the α-arc. The representing angle α is measured from the initial position, where the gear housing is positioned at the highest point

of the α-arc. The succeeding β-arc is mounted perpendicular to the α-arc and moves along a bent gear rack with $125\,\mathrm{mm}$ radius. The angle β is defined as the angle between the end-effector and the gear housing. The remaining linear stage r extends and retracts the end-effector. The length is measured from the bent gear rack (β-arc) to the tip of the needle. The needle tip is shifted through offsets in the x- and y-direction (s_x, s_y) in the corresponding tip coordinate system. The forward kinematics of the injection module are derived from its attachment point (P) to the needle tip (N) using the homogeneous transformation matrix

$$H_N^P = \begin{pmatrix} R^{3\times3} & T^{3\times1} \\ 0^{1\times3} & 1 \end{pmatrix} \tag{7.1}$$

with rotation matrix R and transformation matrix T.

The workspace of the injection module has been designed such that injections may be done into the entire safe region for injection, as defined in Fig. 7.3, even if the patient's eye is rotated towards the nose by a maximum angle of $35°$. The motion of the rotation around the eye is limited physically by the length of the arcs, the translation is limited by the length of the end-effector. Joint limitations are derived from the physical system in consonance with the required range of motion. The theoretical workspace of the injection module is simulated in MATLAB and projections on the xy- and yz-planes are plotted over the sketch of an eye ball in Fig. 7.6, the blue lines indicate possible injection trajectories. The workspace is non-symmetric due the constant offsets (s_x, s_y) in the final configuration.

7.3.5 Vision System

Two near-infrared (NIR) sensitive cameras (See3CAM, e-con Systems) are integrated into the assistive intravitreal injection system. The top camera points downwards, the side camera is installed at a right angle to the eye, as illustrated in Fig. 7.5(b). Both cameras are fitted with a lens (Edmund Optics, USA).As the iris reveals its unique patterns under near infrared illumination, the workspace of the injection module is illuminated by several LED's with
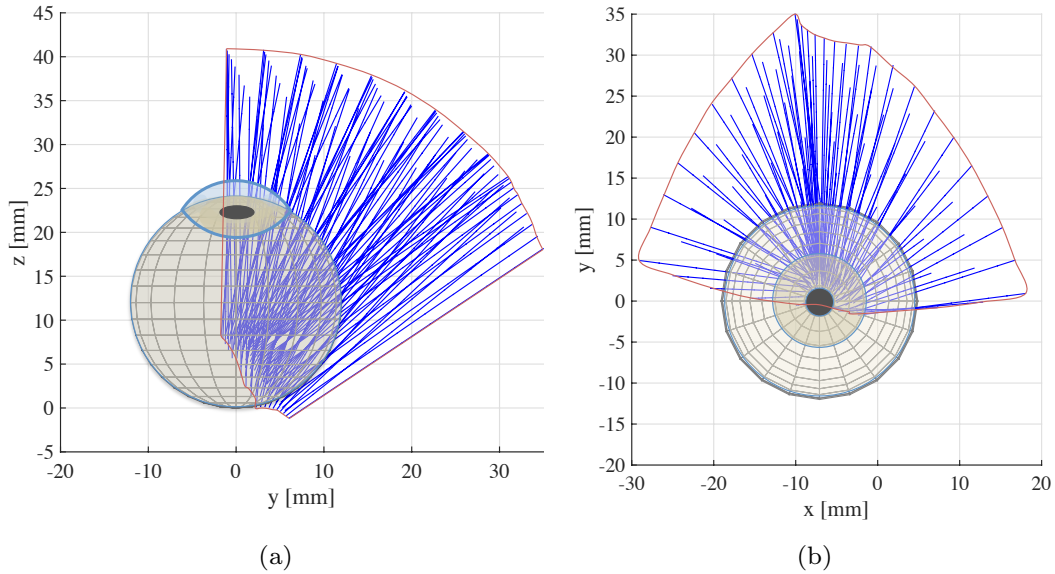
Figure 7.6: Kinematics simulation of the injection module (a) sideview, (b) topview. The red envelope contains the workspace of the injection module. The blue lines indicate possible injection trajectories for the injection of the needle into the eye as indicated in the image.

wavelengths between 830 and 940 nm. The illumination has been designed under consideration of eye safety [155], such that spectral radiance is below allowed cornea exposure limits. The vision system allows for several functionalities, such as tracking of the pupil, scanning the iris, locating the desired injection point, and monitoring of the patient. The camera images are displayed on the UI at all times, allowing the physician to monitor the patient.

A tracking algorithm has been implemented to track the x- and y-position of the pupil of the eye as soon as the eye becomes visible in the top camera's field of view. As soon as the eye is visible in the side camera's field of view, the algorithm also tracks the z-position of the eye. The position information are used as feedback to the positioning module, which centres the injecting system above the patient's eye. The point for injection is selected by the operator. In future applications, it can be selected by the system within the safe region

for injection (defined in Section 7.2.3) and according to the patient's history of injection points, such that no scleral thinning occurs due to subsequent injections in the same location. This is explained in more detail in Appendix B. The physician can change the point of injection by selecting a new point for injection on the UI. After initialisation of the injection process, the top camera is used to take an image of the iris for patient and eye recognition, as described in Section 7.2.2. Subsequently, the vision guided injection process is started.

7.4   Control

The control logic for the automated injection process includes homing of all motors, coarse and fine positioning of the system above the patient's head, needle positioning and alignment, and subsequent injection, as illustrated in Fig. 7.7. All software has been implemented in C++ in the ROS environment.

7.4.1   Homing

Before the injection procedure is started, all actuators must be moved to their homing position. The actuators calibrate themselves by moving in a preset direction until a limit switch is activated. Once all limit switches have been reached by the actuators, a position command is published to the motor controller to move each actuator to a predefined initial position. A flag is set if all actual motor positions are within a predefined error margin (here $\pm$ 10 encoder counts) to the target position. After the flag is set to *true* the system is in its initial position and is ready to start the injection process.

7.4.2   Fine Positioning

After the system has been manually positioned above the patient's head, the system is centred over the treated eye during fine positioning. The side and top cameras start tracking the pupil of the eye. The pupil tracking algorithm first transforms the image into a binary image using the Otsu thresholding technique [156], followed by a number of dilation and erosion steps. The contour of the pupil is found and its circularity is analysed. The vision algorithm
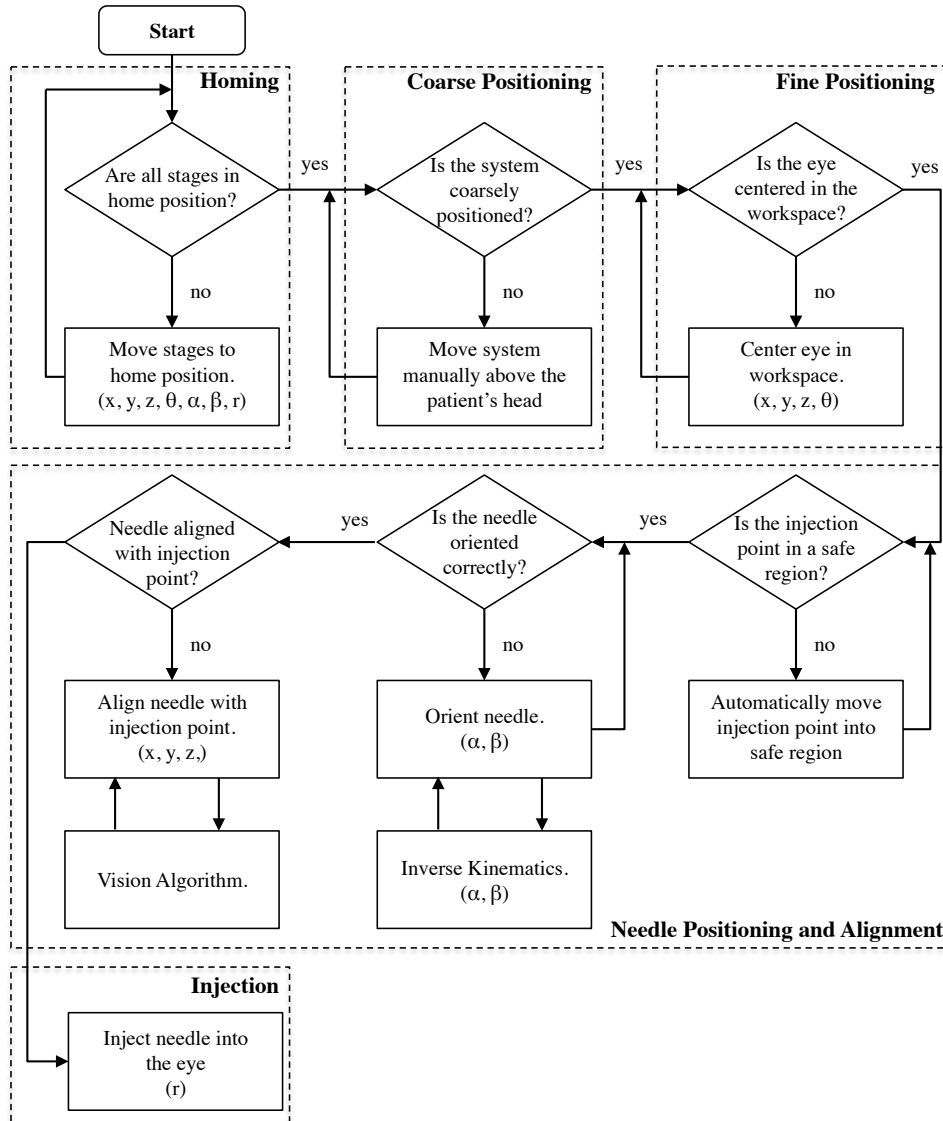
Figure 7.7: The block diagram shows the control logic of the automated injection procedure, including homing, coarse and fine positioning of the system above the patient's head, needle positioning and alignment, and the injection.

outputs the pixel position of the pupil in cartesian space. The error to a target position, the centre of the image, is derived and a P-controller is used to move the actuators in the positioning module (x, y, z), as illustrated in Fig. 7.8. The
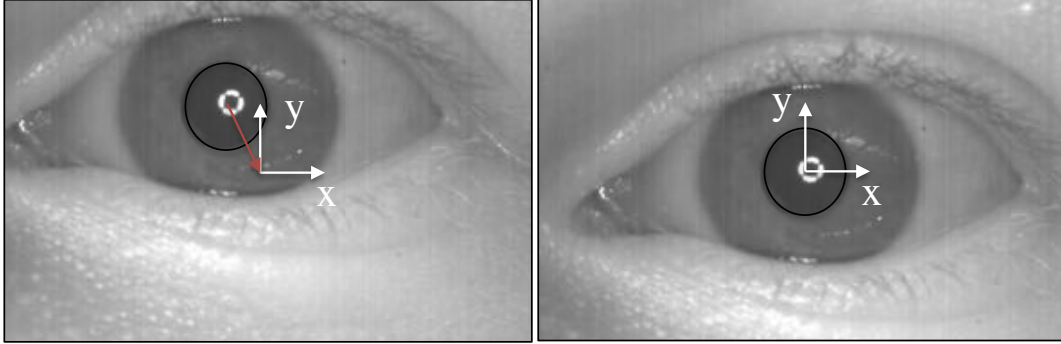
Figure 7.8: During fine positioning of the system, the pupil is tracked in 3D and a P controller moves the actuators of the positioning module until the eye is centred in the workspace of the system.

positioning algorithm is terminated if the error in all three dimensions is less than a specified tolerance (here ± 0.5 mm). A flag is set to *true*, if the system has been centred over the eye.

7.4.3 Needle Positioning and Alignment

After fine positioning, the safe region for injection is calculated (refer to Appendix B) and projected on the image produced by the top camera. This allows the operator to graphically select an injection location within the safe region by clicking with the cursor in the displayed image. If the injection point is selected outside the safe region, it is automatically shifted along the radial direction to lie within the region. Once the injection point has been selected, the direction of gaze (angle ζ about the x-axis) and the coordinates of the injection point in pixels are determined visually, as illustrated in Fig. 7.9(a). During intravitreal injections, the needle should be oriented towards the macula to prevent damaging the crystalline lens and thus ensure safety. With this assumption, the injection orientation in 3D space, $\vec{n}_{inj}$ is calculated as

$$\vec{n}_{inj} = -\frac{\vec{r}_{inj} + \vec{r}_{gaze}}{|\vec{r}_{inj} + \vec{r}_{gaze}|} \qquad (7.2)$$
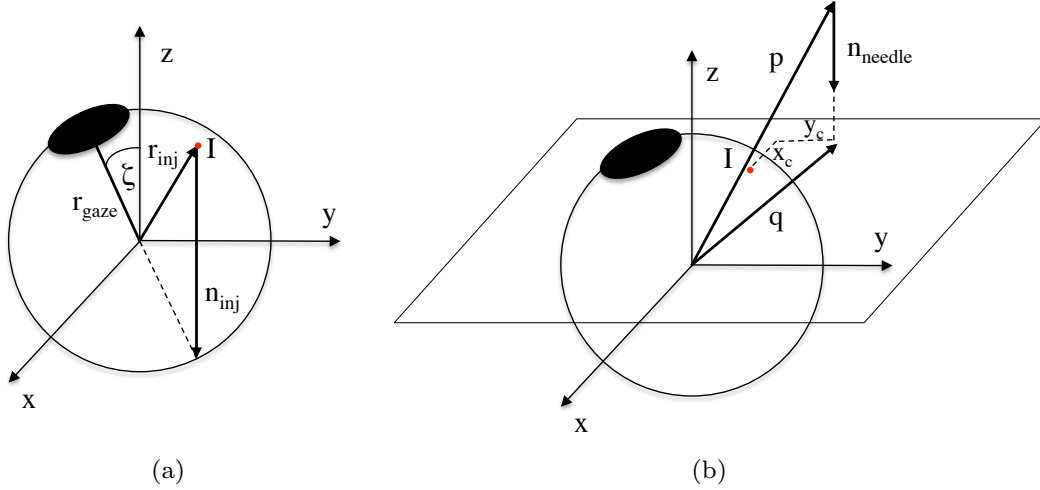
Figure 7.9: (a) Derivation of the injection orientation ($\vec{n}_{inj}$) and (b) position (x_c, y_c). The angle ζ indicates the direction of gaze, I is the preselected injection point.

where $\vec{r}_{inj}$ and $\vec{r}_{gaze}$ are the position vectors from the centre of the eye to the injection point I and the pupil, respectively.

Subsequently, a non-linear least-squares solver is used to derive the required positions of the α- and β-arcs by minimising the error between the required injection orientation, $\vec{n}_{inj}$, and the current orientation of the needle, as given by the forward kinematics

$$\vec{n}_{needle} = \begin{pmatrix} -\sin\alpha\cos\beta \\ \cos\alpha\cos\beta\sin\delta - \sin\beta\cos\delta \\ -\sin\beta\sin\delta - \cos\alpha\cos\beta\cos\delta \end{pmatrix}. \tag{7.3}$$

After calculating the targets for α and β, the corresponding position is published to the motor controllers, which position the arcs within a predefined error margin (here $\pm 0.2°$). To align the needle direction with the injection point, the correction motion in the horizontal plane is calculated. The injection direction vector, starting at an arbitrary point on the injection line from the needle, is

elongated by a factor s until the line crosses the xy-plane shifted to the height of the injection point, as illustrated in Fig. 7.9(b). The position vector $\vec{p}$ is calculated from the forward kinematics, while position vector $\vec{q}$ is derived as

$$\vec{q} = \vec{p} + s \cdot \vec{n}_{needle}. \tag{7.4}$$

The correction in x- and y-directions (x_c, y_c) are finally calculated as the difference between the x and y components of $\vec{q}$ and $\vec{r}_{inj}$. The values are converted to encoder counts and published to the motor controllers, which move the x- and y-stages accordingly.

7.4.4   Injection

After the needle is oriented correctly and is positioned above the selected injection point, the linear stage (r) of the injection module is moved by a calculated distance through the sclera into the eye, waits for several seconds, and is retracted to its initial position. In the current version of the robot, medication release has not been implemented, yet. Future work includes the release of medication and the implementation of closed-loop control for the actuator.

7.5   Experimental Validation of the Injection Process

To evaluate the injection system, the iris recognition algorithm and the injection process are demonstrated through experiments.

7.5.1   Iris Recognition

The iris recognition was tested by evaluating the segmentation and recognition performance. Segmentation performance is evaluated by applying the algorithm to 2739 images from an eye database, which offers demanding conditions as images feature eyelash and eyelid occlusions combined with changing illumination conditions. The algorithm achieved a 93.39% correct segmentation rate. However, in practice the iris recognition algorithm will be used on images of patients' eyes held open by a lid speculum, reducing occlusions and increasing

the success rate. Examples of iris segmentation featuring eyelash and eyelid occlusions under changing light conditions are shown in Fig. 7.10. To analyse the recognition performance, 100 images of 20 different eyes, *i.e.* five images per eye, were taken and the Hamming distance was derived for all possible intraclass (same eyes) and interclass (different eyes) combinations. The resultant distributions are normalised and shown in Fig. 7.11. The two distributions are completely separated, such that a Hamming distance threshold of 0.4 would result in 100% correct recognition rate.

7.5.2 Injection Module Precision and Accuracy

The accuracy and precision of the motion of α- and β-arcs inside the injection module are experimentally evaluated by moving the arcs to predefined positions and measuring the angle of the needle. Three orange beads are attached to the tip of the needle and are tracked visually using the ROS packages *uvc_camera* and *cmvision*. Each arc's motion is evaluated separately, while the other arc is held at a stationary position. Prior to the experiment both arcs are calibrated with the homing procedure. The β-arc is evaluated with a stationary outer arc ($\alpha = 0°$) and the α-arc's motion is analysed while keeping angle β stationary at $28°$. During experiments, the initial positions of the arcs for each measurement are $\alpha = -30°$ and $\beta = 30°$, respectively. The evaluated arc is moved to a targeted angle, while the other arc is stationary. Subsequently, the actual angle of the arc is measured visually and the arc is moved back to its initial position. Each measurement is repeated 10 times. The orientation of
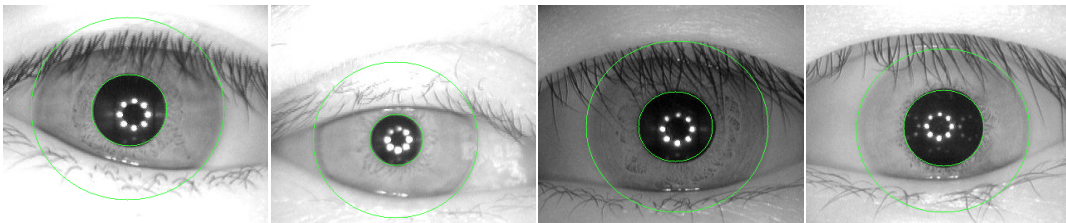
Figure 7.10: Four examples of successful iris segmentation under demanding conditions, such as eyelash and eyelid occlusions and changing light conditions.
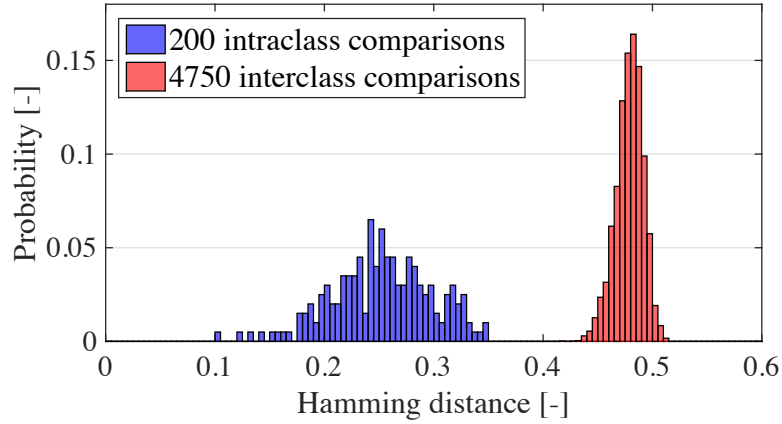
Figure 7.11: Hamming distance distribution of as calculated from hundred images of twenty eyes (five images of each eye). Defining the threshold at 0.4, correct recognition can be achieved for all images.

the needle is derived by linearly fitting a line through the three tracked beads and calculating the angle between this line and the vertical axis. The accuracy is derived as the position error from the measured to the targeted angle. The precision is calculated as the difference between the maximum and the minimum value of measured angles. Tables 7.2 and 7.3 summarise the mean and one standard deviation (1σ) of the accuracy and precision of each arc's motion. The measured accuracy is below $1°$ and the precision below $1.6°$ for both arcs, respectively.

Table 7.2: Measured accuracy (mean and standard deviation) and precision of the motion of arc α (n = 10).

Target angle	$-20°$	$-10°$	$0°$	$10°$	$20°$	$30°$
Accuracy, mean [°]	0.89	-0.55	0.33	0.81	0.26	-0.40
Accuracy, 1σ [°]	0.31	0.32	0.48	0.43	0.30	0.52
Precision [°]	0.98	1.10	1.42	1.11	0.95	1.49

Table 7.3: Measured accuracy (mean and standard deviation) and precision of the motion of arc β (n = 10).

Target angle	40°	50°	60°	70°	80°
Accuracy, mean [°]	0.40	0.20	0.11	-0.04	-0.66
Accuracy, 1σ [°]	0.20	0.36	0.37	0.48	0.42
Precision [°]	0.58	1.06	1.07	1.56	1.36

7.5.3   Intravitreal Injection in *Ex Vivo* Eyes

To demonstrate the functions of the proposed assistive device for intravitreal injections, porcine eyes are injected during *ex vivo* experiments. The experimental setup is illustrated in Fig. 7.12. Cadaver eyes were obtained from the local abattoir and experiments took place less than 10 hours *post mortem*. For each experiment, a porcine eye was fixed in a rubber holder and placed within the reach of the passive arm. First, a human operator moved the passive arm coarsely over the pig eye and fixed it in position. Then the positioning module centred the injection module over the eye. Prior to injection, a human operator selected a point for injection within the safe region on the eye. Then the injection process was started, ignoring eye recognition. Figure 7.13 depicts the steps of the injection procedure. Figure 7.13(a) shows the end-effector with the attached injection needle in its initial position. In a next step, the injection needle is aligned with the targeted point of injection on the *pars plana* by controlling the injection module (Fig. 7.13(b)). By actuating the linear actuator in the end-effector, the injection is accomplished (Fig. 7.13(c)). Finally, the needle is retracted linearly (Fig. 7.13(d)) and the assistive device moves back to its initial position. The experimental process was repeated and the true injection point was compared to the targeted point for safe injection during post-processing. Resulting, it was found that all injections were within the safe region for injection on the cadaver eye. The positioning error ϵ was derived as the difference between the targeted and the actual injection point, as measured visually. The measured accuracy of positioning was found to be $0.8 \pm 0.6\,\text{mm}$ for four separate injection experiments.
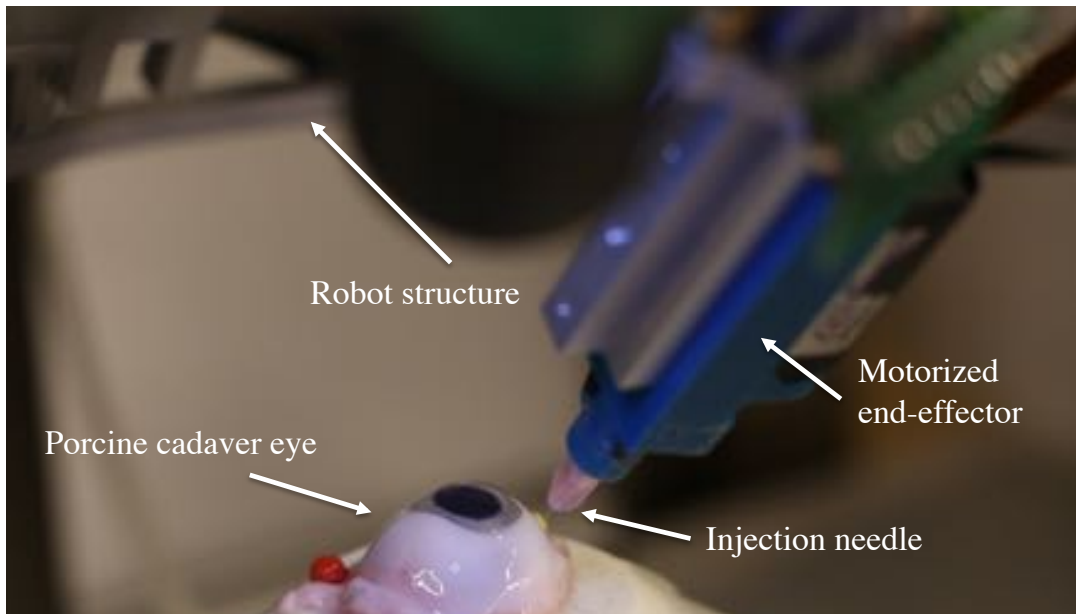
Figure 7.12: Experimental setup of injecting into a porcine cadaver eye. The robot structure supports and controls the position and orientation of the end-effector that allows for injecting a needle into the eye.

7.6   Conclusion

This chapter outlines the potential of an automated assistive system for intravitreal therapy for the treatment of age-related macular degeneration and other chronic ocular diseases. The development of an injection system is demonstrated that consists of a positioning and an injection module. Experiments with *ex vivo* porcine eyes show that the system allows for precise injection into the previously defined safe region for injection, such that neither the crystalline lens, nor the retina in the eye are damaged. In conclusion, technical feasibility of an automated system for IVT is shown that offers a wide range of advantages in today's care of growing number of patients with medically treatable ocular diseases.
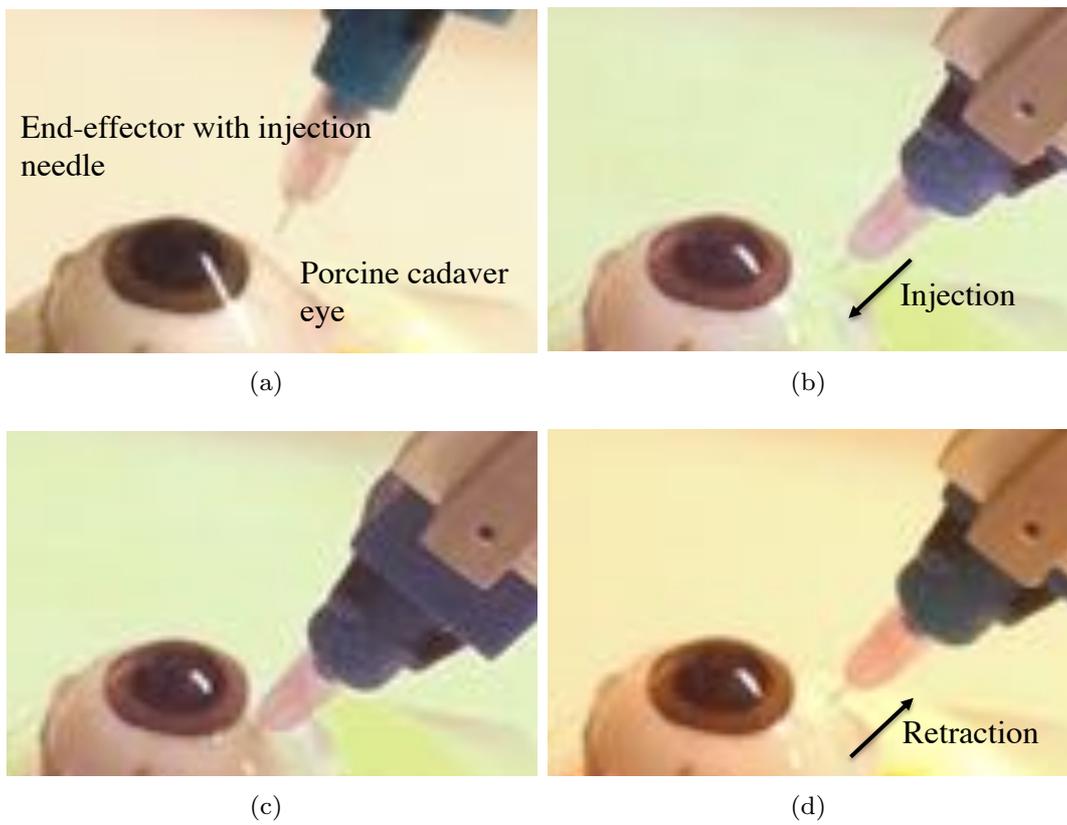
Figure 7.13: Automated injection procedure into an *ex vivo* porcine eye. (a) Alignment of the injection needle. (b) Intravitreal injection. (c) Injection needle inside cadaver eye to deliver medication. (d) Retraction of injection needle from the eye.

Chapter 8

Research Summary and Future Work

8.1 Research Summary

This thesis focuses on the the exploration of assistive robots for minimally invasive surgery for applications in ophthalmology in the posterior and anterior sections of the eye. The main contributions of this work are summarised in the following:

- The motion and manoeuvrability of magnetically controlled, wireless, cylindrical microrobots in the posterior section of the eye has been explored. Motion experiments were conducted in *ex vivo* porcine vitreous and *in vivo* lapine eyes, which were filled with vitreous, silicone oil, or balanced salt solution. Results showed good rotational motion, while translation of intravitreal microrobots was restricted in vitreous due to collagen fibres. Swimming speed of a helically shaped microrobot was investigated in a vitreous phantom with different collagen fibre concentrations. It could be shown that an optimal relationship exists between the dimensions of the microrobot and the fibre content of the surrounding medium.

  Applications for intravitreal microrobots include targeted drug delivery and surgical interventions. A wireless microrobot with an attached hook was magnetically controlled to remove vitreous floaters from the posterior eye in a model. After ophthalmic surgery, the microrobot can be removed utilising a customised tool. Removal of microrobots from the eye was demonstrated in *ex vivo* porcine eyes.

145

- A hybrid magnetic-mechanical actuation system has been developed that actuates a flexible tool inside the anterior eye chamber for automated capsulorhexis, a key step in cataract surgery. The system consists of a mechanical catheter advancer, the electromagnetic actuation system OctoMag, and a flexible tool for high frequency endodiathermy. The system has been shown to control the tool tip on a circular path while cutting through the lens capsular bag during experiments on *ex vivo* porcine lenses.

- A robotic system with a remote centre of motion has been developed for retinal surgery. The system can enter the posterior section of the eye through a single incision in the sclera and then pivots around this entrance point to reduce shear stresses on the tissue. The system has been characterised through experiments and, in future, will be used in an experimental setting to accomplish precise injections into retinal veins in *ex vivo* porcine eyes.

- To treat age-related macular degeneration cost and time efficiently, a system has been developed that automatically injects medication into the vitreous of the eye. The assistive system is remotely initiated by a human operator and allows for high precision injections with a predictable outcome. A computer algorithm tracks the patient's eye at all times during the automated injection process. Automated injection has been demonstrated with *ex vivo* porcine eyes.

In conclusion, several minimally invasive robotic systems for ophthalmology have been explored throughout this work. The assistive robotic devices are either tethered or untethered and can be applied for targeted drug delivery or surgical treatment in the anterior or the posterior section of the eye.

8.2 Future Work

Robot assisted systems for medical applications are an emerging and growing concept. Robotic systems are especially relevant to the field of ophthalmology

due to the small required forces, which often lie below the human perception limit, and the delicate nature of anatomical structures in the eye. Cost and time efficiency become an increasingly important feature of ophthalmic procedures, due to the ageing demographics in many industrialised countries, as well as the scarcity of ophthalmic surgeons. Future assistive systems for ophthalmic interventions must be developed specifically for specific surgeries, but may combine many functions. The robotic systems that were explored throughout this thesis show potential to be utilised for several surgical interventions in the anterior and the posterior eye. However, further development and optimisation are a necessity before testing them in humans.

The potential of wireless microrobots for ophthalmic applications in the posterior section of the eye has been explored in this work. In order to extend on this work and eventually evaluate the technology through clinical studies, applications should be developed that show supremacy over manual surgical interventions. High precision and force feedback are advantages of magnetically controlled microrobots in the eye. Possible applications include targeted drug delivery to the retina, floater removal from the vitreous, epiretinal membrane peeling, subretinal injections for gene therapy and others. In addition, biocompatibility of microrobots must be ensured for interventions with long duration.

A hybrid magnetic-mechanical system for controlling a flexible diathermy tool for automated capsulorhexis has been demonstrated. The system design and fabrication could be optimised and functionality should be demonstrated in an intact porcine eye. The quality (*e.g.* shape, location, size) of the resulting opening in the lens capsule should be quantified and compared to manual capsulorhexis. After evaluating the system, it could be extended to a system demonstrating a complete cataract surgery procedure.

A remote centre of motion (RCM) system has been developed and thorough characterisation of the system's kinematics has been performed. In future applications, the system for retinal surgery will be used to demonstrate retinal

vein injections in porcine eyes. Furthermore, the system could be used in combination with the electromagnetic manipulation system OctoMag. Magnetic manipulation of steerable needles or catheters can be combined using the RCM system for control of location and orientation of the tool at the scleral incision. In order to apply the device for subretinal injections, it could be combined with an optical coherence tomography (OCT) system for detailed visualisation of the retinal layers.

In this thesis, a working prototype has been built, which demonstrates safe and fast injections into the vitreous of *ex vivo* porcine eyes. In future, a clinical grade system for intravitreal injections will be developed and the system will be subject to a certification process in order to obtain the CE certification mark. Clinical usability of the injection system will then be evaluated during clinical studies. The production and commercialisation of the system for automated injections into the eye will be resumed by the start-up company Ophthorobotics AG.

References

[1]   K. Fuchs, "Minimally invasive surgery.," *Endoscopy*, vol. 34, no. 2, pp. 154–159, 2002.

[2]   V. Vitiello, K. Kwok, and G. Yang, "Introduction to robot-assisted minimally invasive surgery (mis)," *Medical Robotics: Minimally Invasive Surgery*, pp. 1–40, 2012.

[3]   L. A. Levin, S. F. Nilsson, J. Ver Hoeve, S. Wu, P. L. Kaufman, and A. Alm, *Adler's Physiology of the Eye*. Elsevier Health Sciences, 2011.

[4]   D. A. Atchison, G. Smith, and G. Smith, "Optics of the human eye," 2000.

[5]   S. Krag, T. Olsen, and T. T. Andreassen, "Biomechanical characteristics of the human anterior lens capsule in relation to age.," *Investigative ophthalmology & visual science*, vol. 38, no. 2, pp. 357–363, 1997.

[6]   B. P. Danysh and M. K. Duncan, "The lens capsule," *Experimental eye research*, vol. 88, no. 2, pp. 151–164, 2009.

[7]   K. Bos, D. Holmes, R. Meadows, K. Kadler, D. McLeod, and P. Bishop, "Collagen fibril organisation in mammalian vitreous by freeze etch/rotary shadowing electron microscopy," *Micron*, vol. 32, no. 3, pp. 301–306, 2001.

[8]   P. N. Bishop, "Structural macromolecules and supramolecular organisation of the vitreous gel," *Progress in retinal and eye research*, vol. 19, no. 3, pp. 323–344, 2000.

[9]   J. Sebag, "Age-related changes in human vitreous structure," *Graefe's archive for clinical and experimental ophthalmology*, vol. 225, no. 2, pp. 89–93, 1987.

[10] J. Kokavec, S. H. Min, M. H. Tan, J. S. Gilhotra, H. S. Newland, S. R. Durkin, J. Grigg, and R. J. Casson, "Biochemical analysis of the living human vitreous," *Clinical & experimental ophthalmology*, 2016.

[11] World Health Organization (WHO), "Priority Eye Diseases." `http://www.who.int/blindness/causes/priority/en/`. Accessed: 20-01-2016.

[12] National Eye Institute (NEI), "2010 U.S. Age-Specific Prevalence Rates for Cataract by Age, and Race/Ethnicity." `https://nei.nih.gov/eyedata/cataract#1`. Accessed: 20-01-2016.

[13] J. Bolger, "How to master capsulorhexis," *Eye*, vol. 9, no. 4, pp. 526–529, 1995.

[14] E. S. Gragoudas, A. P. Adamis, E. T. Cunningham Jr, M. Feinsod, and D. R. Guyer, "Pegaptanib for neovascular age-related macular degeneration," *New England Journal of Medicine*, vol. 351, no. 27, pp. 2805–2816, 2004.

[15] P. J. Rosenfeld, D. M. Brown, J. S. Heier, D. S. Boyer, P. K. Kaiser, C. Y. Chung, and R. Y. Kim, "Ranibizumab for neovascular age-related macular degeneration," *New England Journal of Medicine*, vol. 355, no. 14, pp. 1419–1431, 2006.

[16] S. Day, K. Acquah, P. P. Lee, P. Mruthyunjaya, and F. A. Sloan, "Medicare costs for neovascular age-related macular degeneration, 1994–2007," *American journal of ophthalmology*, vol. 152, no. 6, pp. 1014–1020, 2011.

[17] P. K. Gupta, P. S. Jensen, and E. de Juan Jr, "Surgical forces and tactile perception during retinal microsurgery," in *Proc. Medical Image Computing and Computer-Assisted Intervention–MICCAI99*, pp. 1218–1225, Springer, 1999.

[18] A. D. Jagtap and C. N. Riviere, "Applied force during vitreoretinal microsurgery with handheld instruments," in *Proc. IEEE Int. Conf. Eng. Med. Biol. Soc*, pp. 2771–2773, 2004.

[19] R. V. Clayman, "Transatlantic robot-assisted telesurgery," *The Journal of urology*, vol. 168, no. 2, pp. 873–874, 2002.

[20] J. G. Camara, R. R. B. Zabala, R. D. Henson, and S. H. Senft, "Teleophthalmology: the use of real-time telementoring to remove an orbital tumor," *Ophthalmology*, vol. 107, no. 8, pp. 1468–1471, 2000.

[21] R. Taylor, P. Jensen, L. Whitcomb, A. Barnes, R. Kumar, D. Stoianovici, P. Gupta, Z. Wang, E. Dejuan, and L. Kavoussi, "A steady-hand robotic system for microsurgical augmentation," *The International Journal of Robotics Research*, vol. 18, no. 12, pp. 1201–1210, 1999.

[22] A. Üneri, M. Balicki, J. Handa, P. Gehlbach, R. H. Taylor, I. Iordachita, *et al.*, "New steady-hand eye robot with micro-force sensing for vitreoretinal surgery," in *Proc. Biomedical Robotics and Biomechatronics (BioRob), 2010 3rd IEEE RAS and EMBS International Conference on*, pp. 814–819, 2010.

[23] R. Kumar, P. Berkelman, P. Gupta, A. Barnes, P. S. Jensen, L. L. Whitcomb, and R. H. Taylor, "Preliminary experiments in cooperative human/robot force control for robot assisted microsurgical manipulation," in *Robotics and Automation (ICRA), 2000 IEEE International Conference on*, vol. 1, pp. 610–617, IEEE, 2000.

[24] B. Mitchell, J. Koo, I. Iordachita, P. Kazanzides, A. Kapoor, J. Handa, G. Hager, and R. Taylor, "Development and application of a new steady-hand manipulator for retinal surgery," in *Robotics and Automation (ICRA), 2007 IEEE International Conference on*, pp. 623–629, IEEE, 2007.

[25] C. N. Riviere, W. T. Ang, and P. K. Khosla, "Toward active tremor canceling in handheld microsurgical instruments," *Robotics and Automation, IEEE Transactions on*, vol. 19, no. 5, pp. 793–800, 2003.

[26] R. MacLachlan, B. C. Becker, J. Cuevas Tabares, G. W. Podnar, L. Lobes, C. N. Riviere, *et al.*, "Micron: an actively stabilized hand-

held tool for microsurgery," *Robotics, IEEE Transactions on*, vol. 28, no. 1, pp. 195–212, 2012.

[27] B. C. Becker, S. Voros, R. MacLachlan, G. D. Hager, C. N. Riviere, *et al.*, "Active guidance of a handheld micromanipulator using visual servoing," in *Robotics and Automation (ICRA), 2009 IEEE International Conference on*, pp. 339–344, IEEE, 2009.

[28] B. C. Becker, C. R. Valdivieso, J. Biswas, L. Lobes, C. N. Riviere, *et al.*, "Active guidance for laser retinal surgery with a handheld instrument," in *Engineering in Medicine and Biology Society, 2009. EMBC 2009. Annual International Conference of the IEEE*, pp. 5587–5590, IEEE, 2009.

[29] D. H. Bourla, J. P. Hubschman, M. Culjat, A. Tsirbas, A. Gupta, and S. D. Schwartz, "Feasibility study of intraocular robotic surgery with the da vinci surgical system," *Retina*, vol. 28, no. 1, pp. 154–158, 2008.

[30] A. Tsirbas, C. Mango, and J. Hubschman, "Robotic surgery in ophthalmology," in *Telesurgery*, pp. 125–139, Springer, 2008.

[31] W. Wei, R. Goldman, H. Fine, S. Chang, and N. Simaan, "Modeling and performance evaluation of hybrid multi-arm robots operating on hollow suspended organs," *IEEE Trans. Robot*, vol. 25, no. 1, pp. 147–157, 2009.

[32] H. Yu, J.-H. Shen, R. J. Shah, N. Simaan, and K. M. Joos, "Evaluation of microsurgical tasks with oct-guided and/or robot-assisted ophthalmic forceps," *Biomedical optics express*, vol. 6, no. 2, pp. 457–472, 2015.

[33] H. Yu, J.-H. Shen, K. M. Joos, and N. Simaan, "Design, calibration and preliminary testing of a robotic telemanipulator for oct guided retinal surgery," in *Robotics and Automation (ICRA), 2013 IEEE International Conference on*, pp. 225–231, IEEE, 2013.

[34] H. Yu, R. J. Shah, J. H. Shen, K. M. Joos, and N. Simaan, "Preliminary evaluation of a robotic retinal surgical manipulator," *Investigative Ophthalmology & Visual Science*, vol. 55, no. 13, pp. 2317–2317, 2014.

[35] T. Nakano, N. Sugita, T. Ueta, Y. Tamaki, and M. Mitsuishi, "A parallel robot to assist vitreoretinal surgery," *International journal of computer assisted radiology and surgery*, vol. 4, no. 6, pp. 517–526, 2009.

[36] H. Takahashi, T. Yonemura, N. Sugita, M. Mitsuishi, S. Sora, A. Morita, and R. Mochizuki, "Master manipulator with higher operability designed for micro neuro surgical system," in *Robotics and Automation (ICRA), 2008 IEEE International Conference on*, pp. 3902–3907, IEEE, 2008.

[37] T. Ueta, Y. Yamaguchi, Y. Shirakawa, T. Nakano, R. Ideta, Y. Noda, A. Morita, R. Mochizuki, N. Sugita, M. Mitsuishi, *et al.*, "Robot-assisted vitreoretinal surgery: development of a prototype and feasibility studies in an animal model," *Ophthalmology*, vol. 116, no. 8, pp. 1538–1543, 2009.

[38] Y. Ida, N. Sugita, T. Ueta, Y. Tamaki, K. Tanimoto, and M. Mitsuishi, "Microsurgical robotic system for vitreoretinal surgery," *International journal of computer assisted radiology and surgery*, vol. 7, no. 1, pp. 27–34, 2012.

[39] E. Rahimy, J. Wilson, T. Tsao, S. Schwartz, and J. Hubschman, "Robot-assisted intraocular surgery: development of the iriss and feasibility studies in an animal model," *Eye*, vol. 27, no. 8, pp. 972–978, 2013.

[40] N. Gooch, S. A. Molokhia, R. Condie, R. M. Burr, B. Archer, B. K. Ambati, and B. Wirostko, "Ocular drug delivery for glaucoma management," *Pharmaceutics*, vol. 4, no. 1, pp. 197–211, 2012.

[41] N. M. Davies, "Biopharmaceutical considerations in topical ocular drug delivery," *Clinical and experimental pharmacology and physiology*, vol. 27, no. 7, pp. 558–562, 2000.

[42] A. Urtti, "Challenges and obstacles of ocular pharmacokinetics and drug delivery," *Advanced drug delivery reviews*, vol. 58, no. 11, pp. 1131–1135, 2006.

[43] N. Kuno and S. Fujii, "Recent advances in ocular drug delivery systems," *Polymers*, vol. 3, no. 1, pp. 193–221, 2011.

[44] F. E. Kane, J. Burdan, A. Cutino, and K. E. Green, "Iluvien: a new sustained delivery technology for posterior eye disease," *Expert Opinion on Drug Delivery*, vol. 5, no. 9, pp. 1039–1046, 2008.

[45] G. Jaffe, W. Tao, C. S. Group, *et al.*, "A phase 2 study of encapsulated cntf-secreting cell implant (nt-501) in patients with geographic atrophy associated with dry amd-18 month results," *Investigative Ophthalmology & Visual Science*, vol. 51, no. 13, pp. 6415–6415, 2010.

[46] T. R. Thrimawithana, S. Young, C. R. Bunt, C. Green, and R. G. Alany, "Drug delivery to the posterior segment of the eye," *Drug discovery today*, vol. 16, no. 5, pp. 270–277, 2011.

[47] B. J. Nelson, I. K. Kaliakatsos, and J. J. Abbott, "Microrobots for minimally invasive medicine," *Annual review of biomedical engineering*, vol. 12, pp. 55–85, 2010.

[48] Z. Nagy, O. Ergeneman, J. J. Abbott, M. Hutter, A. M. Hirt, and B. J. Nelson, "Modeling assembled-mems microrobots for wireless magnetic control," in *Robotics and Automation (ICRA), 2008 IEEE International Conference on*, pp. 874–879, IEEE, 2008.

[49] G. Chatzipirpiridis, O. Ergeneman, J. Pokki, F. Ullrich, S. Fusco, J. A. Ortega, K. M. Sivaraman, B. J. Nelson, and S. Pané, "Electroforming of implantable tubular magnetic microrobots for wireless ophthalmologic applications," *Advanced healthcare materials*, vol. 4, no. 2, pp. 209–214, 2015.

[50] L. Zhang, J. J. Abbott, L. Dong, K. E. Peyer, B. E. Kratochvil, H. Zhang, C. Bergeles, and B. J. Nelson, "Characterizing the swimming properties of artificial bacterial flagella," *Nano Letters*, vol. 9, no. 10, pp. 3663–3667, 2009.

[51] L. Zhang, J. J. Abbott, L. Dong, B. E. Kratochvil, D. Bell, and B. J. Nelson, "Artificial bacterial flagella: Fabrication and magnetic control," *Applied Physics Letters*, vol. 94, no. 6, p. 064107, 2009.

[52] K. E. Peyer, L. Zhang, and B. J. Nelson, "Bio-inspired magnetic swimming microrobots for biomedical applications," *Nanoscale*, vol. 5, no. 4, pp. 1259–1272, 2013.

[53] C. Bergeles, M. P. Kummer, B. E. Kratochvil, C. Framme, and B. J. Nelson, "Steerable intravitreal inserts for drug delivery: in vitro and ex vivo mobility experiments," in *Medical Image Computing and Computer-Assisted Intervention–MICCAI 2011*, pp. 33–40, Springer, 2011.

[54] K. B. Yesin, K. Vollmers, and B. J. Nelson, "Modeling and control of untethered biomicrorobots in a fluidic environment using electromagnetic fields," *The International Journal of Robotics Research*, vol. 25, no. 5-6, pp. 527–536, 2006.

[55] O. Ergeneman, G. Dogangil, M. P. Kummer, J. J. Abbott, M. K. Nazeeruddin, and B. J. Nelson, "A magnetically controlled wireless optical oxygen sensor for intraocular measurements," *Sensors Journal, IEEE*, vol. 8, no. 1, pp. 29–37, 2008.

[56] G. Dogangil, O. Ergeneman, J. J. Abbott, S. Pané, H. Hall, S. Muntwyler, and B. J. Nelson, "Toward targeted retinal drug delivery with wireless magnetic microrobots," in *Intelligent Robots and Systems, 2008. IROS 2008. IEEE/RSJ International Conference on*, pp. 1921–1926, IEEE, 2008.

[57] J. Pokki, O. Ergeneman, K. Sivaraman, B. Özkale, M. Zeeshan, T. Lühmann, B. Nelson, and S. Pané, "Electroplated porous polypyrrole nanostructures patterned by colloidal lithography for drug-delivery applications," *Nanoscale*, vol. 4, no. 10, pp. 3083–3088, 2012.

[58] F. Ullrich, S. Fusco, G. Chatzipirpiridis, S. Pané, and B. J. Nelson, "Recent progress in magnetically actuated microrobotics for ophthalmic therapies," *European Ophthalmic Review*, vol. 8, no. 2, pp. 120–126, 2014.

[59] S. Erni, S. Schürle, A. Fakhraee, B. E. Kratochvil, and B. J. Nelson, "Comparison, optimization, and limitations of magnetic manipulation

systems," *Journal of Micro-Bio Robotics*, vol. 8, no. 3-4, pp. 107–120, 2013.

[60] B. J. Nelson, "Microrobotics in medicine," *The International Journal of Robotics Research*, vol. 25, no. 5-6, pp. 527–536, 2006.

[61] A. M. Flynn, K. Udayakumar, D. S. Barrett, J. D. McLurkin, D. L. Franck, and A. Shectman, "Tomorrow's surgery: micromotors and microrobots for minimally invasive procedures," *Minimally Invasive Therapy & Allied Technologies*, vol. 7, no. 4, pp. 343–352, 1998.

[62] J. Hirschberg, *Der Electromagnet in der Augenheilkunde: Eine Monographie von Jul. Hirschberg. Mit 17 Abbildungen im Text.* Veit & Comp., 1885.

[63] C. D. Kelman, "Kelman Electromagnetic Technique," in *Cataract Surgery and Intraocular Lenses: A 21st-Century Perspective* (J. G. Ford and C. L. Karp, eds.), ch. 13, pp. 182–190, Am Med Assoc, 2 ed., 2001.

[64] J. Dailey, J. Phillips, C. Li, and J. Riffle, "Synthesis of silicone magnetic fluid for use in eye surgery," *Journal of magnetism and magnetic materials*, vol. 194, no. 1, pp. 140–148, 1999.

[65] D. Holligan, G. Gillies, and J. Dailey, "Magnetic guidance of ferrofluidic nanoparticles in an in vitro model of intraocular retinal repair," *Nanotechnology*, vol. 14, no. 6, p. 661, 2003.

[66] T. Qiu, T.-C. Lee, A. G. Mark, K. I. Morozov, R. Münster, O. Mierka, S. Turek, A. M. Leshansky, and P. Fischer, "Swimming by reciprocal motion at low reynolds number," *Nature communications*, vol. 5, 2014.

[67] S. Ernst, F. Ouyang, C. Linder, K. Hertting, F. Stahl, J. Chun, H. Hachiya, D. Bänsch, M. Antz, and K.-H. Kuck, "Initial experience with remote catheter ablation using a novel magnetic navigation system magnetic remote catheter ablation," *Circulation*, vol. 109, no. 12, pp. 1472–1475, 2004.

[68] J. Moreno, T. Archondo, R. Barrios, N. Pérez-Castellano, R. Porro, J. G. Quintanilla, V. C. Godoy, R. Cervigón, L. Lobo, Y. Fayad, *et al.*, "Ablation of atrioventricular nodal reentrant tachycardia using remote magnetic guidance (stereotaxis®) requires lower temperature and power settings because of improved local contact," *Revista Española de Cardiología (English Edition)*, vol. 62, no. 9, pp. 1001–1011, 2009.

[69] B. L. Nguyen, J. L. Merino, and E. S. Gang, "Remote navigation for ablation procedures â a new step forward in the treatment of cardiac arrhythmias," *Eur Cardiol*, vol. 6, pp. 50–56, 2010.

[70] Stereotaxis, "Robotic Navigation.." `http://www.stereotaxis.com`. Accessed: 21-01-2016.

[71] Aeon Scientific, "Magnetic catheter steering system." `http://www.aeon-scientific.com`. Accessed: 21-01-2016.

[72] M. P. Kummer, J. J. Abbott, B. E. Kratochvil, R. Borer, A. Sengul, and B. J. Nelson, "Octomag: An electromagnetic system for 5-dof wireless micromanipulation," *Robotics, IEEE Transactions on*, vol. 26, no. 6, pp. 1006–1017, 2010.

[73] International Commission on Non-Ionizing Radiation Protection and others, "Guidelines on limits of exposure to static magnetic fields," *Health Physics*, vol. 96, no. 4, pp. 504–514, 2009.

[74] F. Ullrich, C. Bergeles, J. Pokki, O. Ergeneman, S. Erni, G. Chatzipiridis, S. Pané, C. Framme, and B. J. Nelson, "Mobility experiments with microrobots for minimally invasive intraocular surgerymicrorobot experiments for intraocular surgery," *Investigative ophthalmology & visual science*, vol. 54, no. 4, pp. 2853–2863, 2013.

[75] J. Marescaux, J. Leroy, M. Gagner, F. Rubino, D. Mutter, M. Vix, S. E. Butner, and M. K. Smith, "Transatlantic robot-assisted telesurgery," *Nature*, vol. 413, no. 6854, pp. 379–380, 2001.

[76] F. Ullrich, F. Qiu, J. Pokki, T. Huang, S. Pané, and B. J. Nelson, "Swimming characteristics of helical microrobots in fibrous environments," in *Biomedical Robotics and Biomechatronics (BioRob), 2016 IEEE RAS/EMBS International Conference on*, pp. 470–475, IEEE, 2016.

[77] K. M. Sivaraman, C. Kellenberger, S. Pané, O. Ergeneman, T. Lühmann, N. A. Luechinger, H. Hall, W. J. Stark, and B. J. Nelson, "Porous polysulfone coatings for enhanced drug delivery," *Biomedical microdevices*, vol. 14, no. 3, pp. 603–612, 2012.

[78] K. M. Sivaraman, K. Bayrakceken, O. Ergeneman, S. Pané, T. Lühmann, H. Hall, and B. J. Nelson, "Tailoring the drug loading capacity of polypyrrole films for use in intraocular biomicrorobots," in *Engineering in Medicine and Biology Society (EMBC), 2010 Annual International Conference of the IEEE*, pp. 4359–4362, IEEE, 2010.

[79] The Federal Authorities of the Swiss Confederation, "Tierschutzverordnung." `https://www.admin.ch/opc/de/classified-compilation/20080796/index.html`. Accessed: 25-01-2016.

[80] B. Lee, M. Litt, and G. Buchsbaum, "Rheology of the vitreous body: Part 2. viscoelasticity of bovine and porcine vitreous.," *Biorheology*, vol. 31, no. 4, pp. 327–338, 1993.

[81] P. Sharif-Kashani, J.-P. Hubschman, D. Sassoon, and H. P. Kavehpour, "Rheology of the vitreous gel: effects of macromolecule organization on the viscoelastic properties," *Journal of biomechanics*, vol. 44, no. 3, pp. 419–423, 2011.

[82] D. J. Bell, S. Leutenegger, K. Hammar, L. Dong, and B. J. Nelson, "Flagella-like propulsion for microrobots using a nanocoil and a rotating electromagnetic field," in *Robotics and Automation (ICRA), 2007 IEEE International Conference on*, pp. 1128–1133, IEEE, 2007.

[83] F. Qiu, R. Mhanna, L. Zhang, Y. Ding, S. Fujita, and B. J. Nelson, "Artificial bacterial flagella functionalized with temperature-sensitive liposomes for controlled release," *Sensors and Actuators B: Chemical*, vol. 196, pp. 676–681, 2014.

[84] R. Mhanna, F. Qiu, L. Zhang, Y. Ding, K. Sugihara, M. Zenobi-Wong, and B. J. Nelson, "Artificial bacterial flagella for remote-controlled targeted single-cell drug delivery," *Small*, vol. 10, no. 10, pp. 1953–1957, 2014.

[85] F. Qiu, S. Fujita, R. Mhanna, L. Zhang, B. R. Simona, and B. J. Nelson, "Magnetic helical microswimmers functionalized with lipoplexes for targeted gene delivery," *Advanced Functional Materials*, vol. 25, no. 11, pp. 1666–1671, 2015.

[86] A. Servant, F. Qiu, M. Mazza, K. Kostarelos, and B. J. Nelson, "Controlled in vivo swimming of a swarm of bacteria-like microrobotic flagella," *Advanced Materials*, vol. 27, no. 19, pp. 2981–2988, 2015.

[87] J. Gray and G. Hancock, "The propulsion of sea-urchin spermatozoa," *Journal of Experimental Biology*, vol. 32, no. 4, pp. 802–814, 1955.

[88] S. Childress, *Mechanics of swimming and flying.* Cambridge University Press, 2 ed., 1981.

[89] M. Holwill and R. Burge, "A hydrodynamic study of the motility of flagellated bacteria," *Archives of biochemistry and biophysics*, vol. 101, no. 2, pp. 249–260, 1963.

[90] S. E. Spagnolie, B. Liu, and T. R. Powers, "Locomotion of helical bodies in viscoelastic fluids: enhanced swimming at large helical amplitudes," *Physical review letters*, vol. 111, no. 6, p. 068101, 2013.

[91] H. C. Berg and L. Turner, "Movement of microorganisms in viscous environments," *Nature*, vol. 278, pp. 349–351, 1979.

[92] Y. Magariyama and S. Kudo, "A mathematical explanation of an increase in bacterial swimming speed with viscosity in linear-polymer solutions," *Biophysical journal*, vol. 83, no. 2, pp. 733–739, 2002.

[93] A. Leshansky, "Enhanced low-reynolds-number propulsion in heterogeneous viscous environments," *Physical Review E*, vol. 80, no. 5, p. 051911, 2009.

[94] B. Liu, T. R. Powers, and K. S. Breuer, "Force-free swimming of a model helical flagellum in viscoelastic fluids," *Proceedings of the National Academy of Sciences*, vol. 108, no. 49, pp. 19516–19520, 2011.

[95] H. C. Fu, V. B. Shenoy, and T. R. Powers, "Low-reynolds-number swimming in gels," *EPL (Europhysics Letters)*, vol. 91, no. 2, p. 24002, 2010.

[96] D. Schamel, A. G. Mark, J. G. Gibbs, C. Miksch, K. I. Morozov, A. M. Leshansky, and P. Fischer, "Nanopropellers and their actuation in complex viscoelastic media," *ACS nano*, vol. 8, no. 9, pp. 8794–8801, 2014.

[97] J. J. Abbott, M. C. Lagomarsino, L. Zhang, L. Dong, and B. J. Nelson, "How should microrobots swim?," *The international journal of Robotics Research*, 2009.

[98] K. E. Peyer, F. Qiu, L. Zhang, and B. J. Nelson, "Movement of artificial bacterial flagella in heterogeneous viscous environments at the microscale," in *Intelligent Robots and Systems (IROS), 2012 IEEE/RSJ International Conference on*, pp. 2553–2558, IEEE, 2012.

[99] S. Gorgieva and V. Kokol, *Collagen-vs. gelatine-based biomaterials and their biocompatibility: review and perspectives.* INTECH Open Access Publisher, 2011.

[100] M. A. Masuelli, M. G. Sansone, and D. Aplicada, *Hydrodynamic Properties of Gelatin-Studies from Intrinsic Viscosity Measurements.* INTECH Open Access Publisher, 2012.

[101] D. P. Sendrowski and M. A. Bronstein, "Current treatment for vitreous floaters," *Optometry-Journal of the American Optometric Association*, vol. 81, no. 3, pp. 157–161, 2010.

[102] W.-F. Tsai, Y.-C. Chen, and C.-Y. Su, "Treatment of vitreous floaters with neodymium yag laser.," *British journal of ophthalmology*, vol. 77, no. 8, pp. 485–488, 1993.

[103] Y. Delaney, A. Oyinloye, and L. Benjamin, "Nd: Yag vitreolysis and pars plana vitrectomy: surgical treatment for vitreous floaters," *Eye*, vol. 16, no. 1, pp. 21–26, 2002.

[104] Ellex, "Floater types.." `http://www.ellex.com/patients/floaters/`. Accessed: 04-04-2016.

[105] P. R. Stoessel, R. N. Grass, A. Sánchez-Ferrer, R. Fuhrer, T. Schweizer, R. Mezzenga, and W. J. Stark, "Spinning angora rabbit wool-like porous fibers from a non-equilibrated gelatin/water/2-propanol mixture," *Advanced Functional Materials*, vol. 24, no. 13, pp. 1831–1839, 2014.

[106] P. R. Stoessel, R. A. Raso, T. Kaufmann, R. N. Grass, and W. J. Stark, "Fibers mechanically similar to sheep wool obtained by wet spinning of gelatin and optional plasticizers," *Macromolecular Materials and Engineering*, vol. 300, no. 2, pp. 234–241, 2015.

[107] F. Ullrich, J. Lussi, D. Felekis, S. Michels, A. J. Petruska, and B. J. Nelson, "Perforation forces of the intact porcine anterior lens capsule," *Journal of the mechanical behavior of biomedical materials*, vol. 62, pp. 347–354, 2016.

[108] F. Ullrich, S. Schuerle, R. Pieters, A. Dishy, S. Michels, and B. J. Nelson, "Automated capsulorhexis based on a hybrid magnetic-mechanical actuation system," in *Robotics and Automation (ICRA), 2014 IEEE International Conference on*, pp. 4387–4392, IEEE, 2014.

[109] R. J. Olson, N. Mamalis, L. Werner, and D. J. Apple, "Cataract treatment in the beginning of the 21st century," *American journal of ophthalmology*, vol. 136, no. 1, pp. 146–154, 2003.

[110] T. Raviv, "The perfectly sized capsulorhexis," *J. Cataract Refract. Surg*, vol. 6, pp. 37–41, 2009.

[111] G. Ravalico, D. Tognetto, M. Palomba, P. Busatto, and F. Baccara, "Capsulorhexis size and posterior capsule opacification," *Journal of Cataract & Refractive Surgery*, vol. 22, no. 1, pp. 98–103, 1996.

[112] T. Sugiura, D. Kurosaka, Y. Uezuki, S. Eguchi, H. Obata, and T. Takahashi, "Creating cataract in a pig eye," *Journal of Cataract & Refractive Surgery*, vol. 25, no. 5, pp. 615–621, 1999.

[113] S. K. Pandey, L. Werner, M. Escobar-Gomez, N. Visessook, Q. Peng, and D. J. Apple, "Creating cataracts of varying hardness to practice extracapsular cataract extraction and phacoemulsification," *Journal of Cataract & Refractive Surgery*, vol. 26, no. 3, pp. 322–329, 2000.

[114] A. S. Vilupuru and A. Glasser, "Optical and biometric relationships of the isolated pig crystalline lens," *Ophthalmic and Physiological Optics*, vol. 21, no. 4, pp. 296–311, 2001.

[115] S. Krag and T. T. Andreassen, "Biomechanical measurements of the porcine lens capsule," *Experimental eye research*, vol. 62, no. 3, pp. 253–260, 1996.

[116] M. Dubbelman and G. Van der Heijde, "The shape of the aging human lens: curvature, equivalent refractive index and the lens paradox," *Vision research*, vol. 41, no. 14, pp. 1867–1877, 2001.

[117] D. Moore, G. McCabe, W. Duckworth, and L. Alwan, *The practice of business statistics*. Wh Freeman, 2008.

[118] I. N. Sneddon, "The relation between load and penetration in the axisymmetric boussinesq problem for a punch of arbitrary profile," *International journal of engineering science*, vol. 3, no. 1, pp. 47–57, 1965.

[119] M. Chyasnavichyus, S. L. Young, and V. V. Tsukruk, "Probing of polymer surfaces in the viscoelastic regime," *Langmuir*, vol. 30, no. 35, pp. 10566–10582, 2014.

[120] C. Storm, J. J. Pastore, F. C. MacKintosh, T. C. Lubensky, and P. A. Janmey, "Nonlinear elasticity in biological gels," *Nature*, vol. 435, no. 7039, pp. 191–194, 2005.

[121] R. Klöti, "Bipolar-Nassfeld-Diathermie in der Mikrochirurgie," *Klinische Monatsblätter für Augenheilkunde*, vol. 184, no. 05, pp. 442–444, 1984.

[122] F. Gassmann, B. Schimmelpfennig, and R. Klöti, "Anterior capsulotomy by means of bipolar radio-frequency endodiathermy," *Journal of Cataract & Refractive Surgery*, vol. 14, no. 6, pp. 673–676, 1988.

[123] R. Klöti, "Vordere Hochfrequenz (HF)-Kapsulotomie. I. Experimentelle Studie," *Klinische Monatsblätter für Augenheilkunde*, vol. 200, no. 5, pp. 507–510, 1992.

[124] C. Coester, "Vordere Hochfrequenz-Kapsulotomie: Chancen und Probleme," *Klinische Monatsblätter für Augenheilkunde*, vol. 208, no. 05, pp. 268–269, 1996.

[125] Oertli Instrumente AG, "Klöti Bipolar." `http://www.oertli-instruments.com`. Accessed: 13-04-2016.

[126] H. Tari, "On the parametric large deflection study of euler–bernoulli cantilever beams subjected to combined tip point loading," *International Journal of Non-Linear Mechanics*, vol. 49, pp. 90–99, 2013.

[127] I. Tunay, "Modeling magnetic catheters in external fields," in *Engineering in Medicine and Biology Society, 2004. IEMBS'04. 26th Annual International Conference of the IEEE*, vol. 1, pp. 2006–2009, IEEE, 2004.

[128] S. Krag, K. Thim, and L. Corydon, "Diathermic capsulotomy versus capsulorhexis: a biomechanical study," *Journal of Cataract & Refractive Surgery*, vol. 23, no. 1, pp. 86–90, 1997.

[129] O. Findl and M. Amon, "Anterior capsulotomy created by radiofrequency endodiathermy and continuous curvilinear posterior capsulorhexis in a patient with intumescent cataract and primary capsular fibrosis," *Journal of Cataract & Refractive Surgery*, vol. 24, no. 6, pp. 870–871, 1998.

[130] S. J. Blumenkranz and D. J. Rosa, "Manipulator positioning linkage for robotic surgery," June 12 2001. US Patent 6,246,200.

[131] E. M. Boctor, R. J. Webster III, H. Mathieu, A. M. Okamura, and G. Fichtinger, "Virtual remote center of motion control for needle placement robots," *Computer Aided Surgery*, vol. 9, no. 5, pp. 175–183, 2004.

[132] A. Gijbels, N. Wouters, P. Stalmans, H. Van Brussel, D. Reynaerts, and E. V. Poorten, "Design and realisation of a novel robotic manipulator for retinal surgery," in *Intelligent Robots and Systems (IROS), 2013 IEEE/RSJ International Conference on*, pp. 3598–3603, IEEE, 2013.

[133] G. Zong, X. Pei, J. Yu, and S. Bi, "Classification and type synthesis of 1-dof remote center of motion mechanisms," *Mechanism and Machine Theory*, vol. 43, no. 12, pp. 1585–1595, 2008.

[134] A. K. Kwok, T. Y. Lai, and K. S. Yuen, "Epiretinal membrane surgery with or without internal limiting membrane peeling," *Clinical & experimental ophthalmology*, vol. 33, no. 4, pp. 379–385, 2005.

[135] P. Mitchell, W. Smith, T. Chey, J. J. Wang, and A. Chang, "Prevalence and associations of epiretinal membranes: the blue mountains eye study, australia," *Ophthalmology*, vol. 104, no. 6, pp. 1033–1040, 1997.

[136] D. J. McCarty, B. N. Mukesh, V. Chikani, J. J. Wang, P. Mitchell, H. R. Taylor, and C. A. McCarty, "Prevalence and associations of epiretinal membranes in the visual impairment project," *American journal of ophthalmology*, vol. 140, no. 2, pp. 288–e1, 2005.

[137] S. Rogers, R. L. McIntosh, N. Cheung, L. Lim, J. J. Wang, P. Mitchell, J. W. Kowalski, H. Nguyen, T. Y. Wong, I. E. D. Consortium, *et al.*, "The prevalence of retinal vein occlusion: pooled data from population studies from the United States, Europe, Asia, and Australia," *Ophthalmology*, vol. 117, no. 2, pp. 313–319, 2010.

[138] M. B. Parodi, P. Lanzetta, G. Guarnaccia, and T. Friberg, "Surgical treatments of central retinal vein occlusion," in *Seminars in ophthalmology*, vol. 18, pp. 142–146, Informa UK Ltd UK, 2003.

[139] J. N. Weiss and L. A. Bynoe, "Injection of tissue plasminogen activator into a branch retinal vein in eyes with central retinal vein occlusion," *Ophthalmology*, vol. 108, no. 12, pp. 2249–2257, 2001.

[140] M. K. Tameesh, R. R. Lakhanpal, G. Y. Fujii, M. Javaheri, T. H. Shelley, S. D'anna, A. C. Barnes, E. Margalit, M. Farah, E. De Juan, *et al.*, "Retinal vein cannulation with prolonged infusion of tissue plasminogen activator (t-pa) for the treatment of experimental retinal vein occlusion in dogs," *American journal of ophthalmology*, vol. 138, no. 5, pp. 829–839, 2004.

[141] N. Berker and C. Batman, "Surgical treatment of central retinal vein occlusion," *Acta ophthalmologica*, vol. 86, no. 3, pp. 245–252, 2008.

[142] C. N. Riviere and P. S. Jensen, "A study of instrument motion in retinal microsurgery," in *Engineering in Medicine and Biology Society, 2000. Proceedings of the 22nd Annual International Conference of the IEEE*, vol. 1, pp. 59–60, IEEE, 2000.

[143] D. J. Park and J. Karesh, "Topographic anatomy of the eye: an overview," *Duanes Foundations of Clinical Ophthalmology*, vol. 1, 2006.

[144] H. Kolb, E. Fernandez, and R. Nelson, *Facts and Figures Concerning the Human Retina–Webvision: The Organization of the Retina and Visual System.* University of Utah Health Sciences Center, 1995.

[145] F. Ullrich, S. Michels, D. Lehmann, R. S. Pieters, M. Becker, and B. J. Nelson, "Assistive device for efficient intravitreal injections," *Ophthalmic Surgery, Lasers and Imaging Retina*, vol. 47, no. 8, 2016.

[146] A. R. Rudnicka, V. V. Kapetanakis, Z. Jarrar, A. K. Wathern, R. Wormald, A. E. Fletcher, D. G. Cook, and C. G. Owen, "Incidence of late-stage age-related macular degeneration in american whites: systematic review and meta-analysis," *American journal of ophthalmology*, vol. 160, no. 1, pp. 85–93, 2015.

[147] M. Badran and I. Laher, "Type II diabetes mellitus in Arabic-speaking countries," *International journal of endocrinology*, vol. 2012, 2012.

[148] R. McKay, C. A. McCarty, and H. R. Taylor, "Diabetic retinopathy in victoria, australia: the visual impairment project," *British journal of ophthalmology*, vol. 84, no. 8, pp. 865–870, 2000.

[149] J. Gudeman, M. Jozwiakowski, J. Chollet, and M. Randell, "Potential risks of pharmacy compounding," *Drugs in R&D*, vol. 13, no. 1, pp. 1–8, 2013.

[150] S. Michels, M. Becker, J. Wachtlin, and S. Binder, "The intravitreal injection: Variations in regulations, cost and reimbursement in europe," *Spektrum der Augenheilkunde*, vol. 26, no. 1, pp. 2–6, 2012.

[151] J. G. Daugman, "High confidence visual recognition of persons by a test of statistical independence," *Pattern Analysis and Machine Intelligence, IEEE Transactions on*, vol. 15, no. 11, pp. 1148–1161, 1993.

[152] J. G. Daugman, "Uncertainty relation for resolution in space, spatial frequency, and orientation optimized by two-dimensional visual cortical filters," *JOSA A*, vol. 2, no. 7, pp. 1160–1169, 1985.

[153] L. Golder, "Begleitstudie anlässlich der Einführung von Swiss-DRG im Auftrag der FMH." `http://www.gfsbern.ch/de-ch/Detail/begleitstudie-anlaesslich-der-einfuehrung-von-swissdrg`. Accessed: 05-02-2016.

[154] E. Souied, S. Nghiem-Buffet, C. Leteneux, S. Bayer, A. Derveloy, A. Sagkriotis, G. Becker, and S. Cohen, "Ranibizumab prefilled syringes: benefits of reduced syringe preparation times and less complex preparation procedures.," *European journal of ophthalmology*, vol. 25, no. 6, pp. 529–534, 2015.

[155] C. Jaeger, "Eye safety of ireds used in lamp applications," *Application note, OSRAM Opto Semiconductors GmbH*, 2009.

[156] N. Otsu, "A threshold selection method from gray-level histograms," *Automatica*, vol. 11, no. 285-296, pp. 23–27, 1975.

[157] H. Gross, F. Blechinger, and B. Achtner, *Human eye.* Wiley Online Library, 2008.

[158] F. Ullrich, K. S. Dheman, S. Schuerle, and B. J. Nelson, "Magnetically actuated and guided milli-gripper for medical applications," in *Robotics and Automation (ICRA), 2015 IEEE International Conference on*, pp. 1751–1756, IEEE, 2015.

[159] P. Klaritsch, K. Albert, T. Van Mieghem, L. Gucciardo, E. Done, B. Bynens, and J. Deprest, "Instrumental requirements for minimal invasive fetal surgery," *BJOG: An International Journal of Obstetrics & Gynaecology*, vol. 116, no. 2, pp. 188–197, 2009.

[160] A. Alogla, P. Scanlan, W. Shu, and R. Reuben, "A scalable syringe-actuated microgripper for biological manipulation," *Sensors and Actuators A: Physical*, vol. 202, pp. 135–139, 2013.

[161] R. Pérez, J. Agnus, C. Clévy, A. Hubert, and N. Chaillet, "Modeling, fabrication, and validation of a high-performance 2-dof piezoactuator for micromanipulation," *Mechatronics, IEEE/ASME Transactions on*, vol. 10, no. 2, pp. 161–171, 2005.

[162] J. Kyung, B. Ko, Y. Ha, and G. Chung, "Design of a microgripper for micromanipulation of microcomponents using sma wires and flexible

hinges," *Sensors and Actuators A: Physical*, vol. 141, no. 1, pp. 144–150, 2008.

[163] Z. Zhong and C. Yeong, "Development of a gripper using sma wire," *Sensors and Actuators A: Physical*, vol. 126, no. 2, pp. 375–381, 2006.

[164] M. Kohl, B. Krevet, and E. Just, "SMA microgripper system," *Sensors and Actuators A: Physical*, vol. 97, pp. 646–652, 2002.

[165] F. Beyeler, A. Neild, S. Oberti, D. J. Bell, Y. Sun, J. Dual, and B. J. Nelson, "Monolithically fabricated microgripper with integrated force sensor for manipulating microobjects and biological cells aligned in an ultrasonic field," *Microelectromechanical Systems, Journal of*, vol. 16, no. 1, pp. 7–15, 2007.

[166] T. G. Leong, C. L. Randall, B. R. Benson, N. Bassik, G. M. Stern, and D. H. Gracias, "Tetherless thermobiochemically actuated microgrippers," *Proceedings of the National Academy of Sciences*, vol. 106, no. 3, pp. 703–708, 2009.

[167] H. Chang, H. Zhao, F. Ye, G. Yuan, J. Xie, M. Kraft, and W. Yuan, "A rotary comb-actuated microgripper with a large displacement range," *Microsystem technologies*, vol. 20, no. 1, pp. 119–126, 2014.

[168] G. Iddan, G. Meron, A. Glukhovsky, and P. Swain, "Wireless capsule endoscopy," *Nature*, vol. 405, p. 417, 2000.

[169] D. G. Adler and C. J. Gostout, "Wireless capsule endoscopy," *Hospital Physician*, vol. 39, no. 5, pp. 14–22, 2003.

[170] S. Park, K.-i. Koo, S. M. Bang, J. Y. Park, S. Y. Song, *et al.*, "A novel microactuator for microbiopsy in capsular endoscopes," *Journal of Micromechanics and Microengineering*, vol. 18, no. 2, p. 025032, 2008.

[171] K.-C. Kong, J. Cha, D. Jeon, and D.-i. D. Cho, "A rotational micro biopsy device for the capsule endoscope," in *Intelligent Robots and Sys-*

tems, 2005.(IROS 2005). 2005 IEEE/RSJ International Conference on, pp. 1839–1843, IEEE, 2005.

[172] M. Simi, G. Gerboni, A. Menciassi, and P. Valdastri, "Magnetic torsion spring mechanism for a wireless biopsy capsule," *Journal of Medical Devices*, vol. 7, no. 4, p. 041009, 2013.

[173] F. Carpi, N. Kastelein, M. Talcott, and C. Pappone, "Magnetically controllable gastrointestinal steering of video capsules," *Biomedical Engineering, IEEE Transactions on*, vol. 58, no. 2, pp. 231–234, 2011.

[174] S. Yim and M. Sitti, "Design and analysis of a magnetically actuated and compliant capsule endoscopic robot," in *Robotics and Automation (ICRA), 2011 IEEE International Conference on*, pp. 4810–4815, IEEE, 2011.

[175] S. Yim and M. Sitti, "Design and rolling locomotion of a magnetically actuated soft capsule endoscope," *Robotics, IEEE Transactions on*, vol. 28, no. 1, pp. 183–194, 2012.

[176] R. S. Hartenberg and J. Denavit, *Kinematic synthesis of linkages*. McGraw-Hill, 1964.

Chapter A

Intravitreal Microrobots near the Retina

A.1 Microrobot in the Vitreous Humor

It has been shown that untethered microrobots can be steered and controlled in fluidic environments through externally applied magnetic forces [72]. This method allows for minimally invasive surgery and diagnostic procedures inside the vitreous cavity of the eye utilising intraocular microrobots [55], [56]. In this approach a wireless microrobot is injected through the *pars plana* region of the eye into the vitreous cavity, where it can be moved with an electromagnetic manipulation system, the OctoMag [72], to accurately accomplish ophthalmic operations. The utilisation of steerable microrobots in ophthalmology shows several advantages, such as reduced risk of inflammation and damage of the retina. An experimental study by [17] shows that only $19.3 \pm 8.1\%$ of all forces during retinal surgery can be perceived by the ophthalmic surgeon. During operation inside the eye the delicate structure of the retina is under constant risk of damage and only highly skilled and experienced ophthalmic surgeons can accomplish such operations. Utilising wirelessly controlled microrobots as ophthalmic tools during retinal surgery enables precise tracking of applied forces, which are beyond the limits of human perception. Thus, especially ophthalmic surgery in close proximity to the retina can benefit from intravitreal microrobots.

The human vitreous changes its viscosity during the ageing process and liquefies [9], so that its fluidic properties become similar to those of water.

171

Therefore, wireless microrobotic tools for ophthalmic surgery must be controllable in low-viscosity fluids. Due to decreased buoyancy in water compared to vitreous the microrobot sinks near the retina due to gravity. When the microrobot is adjacent to retinal tissue in the eye, resistive forces become more prominent. These forces include friction between the microrobot and the retina, adhesion forces, and drag. This section experimentally investigates the influence of an intraocular microrobot's direction of motion, its orientation, and its surface properties on the magnitude of restrictive forces in close proximity to the retina.

A.2   Materials and Methods

To simulate the conditions during retinal surgery utilising microrobots, experiments are conducted in *ex vivo* porcine eyes, which were obtained from the abattoir. The cornea, lens and vitreous are removed while carefully maintaining the original shape of the eye. To remove any residual vitreous in the eye globe it is flushed thoroughly with distilled water. The vitreous is replaced by phosphate-buffered saline solution (PBS for laboratory use) and a microrobot is injected into the eye using a $23G$ injection needle. Subsequently, the porcine eye is placed in the centre of the OctoMag workspace that is observed by a camera at a frame rate of $30\,\mathrm{Hz}$. Magnetic fields, defining the microrobot orientation, and magnetic gradients, resulting in translational movement, are applied to the microrobotic tool, which lies close to the retinal tissue.

Ex vivo experiments are conducted for microrobots with different surface properties, one coated with a gold (Au) layer the other coated with polypyrrole (Ppy). In order to investigate the influence of microrobot orientation and direction of motion, five different combinations are defined, as illustrated in Fig. A.1. For each configuration, a magnetic gradient is applied in the direction as indicated by the black arrows, resulting in translational movement of the microrobot. In configurations (a) and (b) the gradient is along the microrobot orientation, while it is orthogonal in configurations (c), (d) and (e).

172
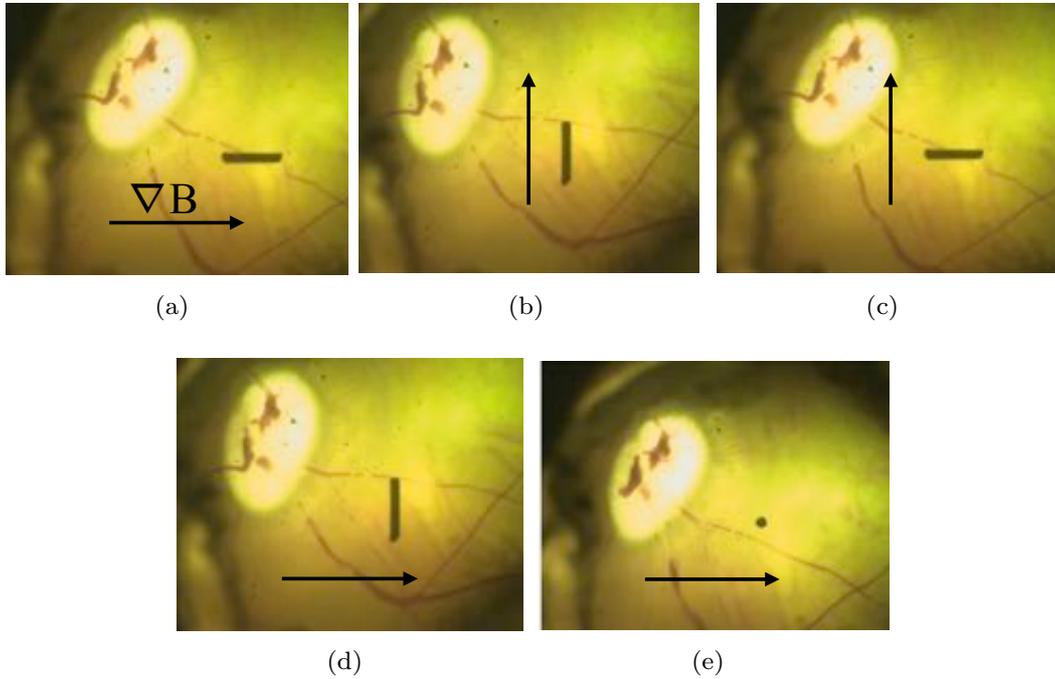
Figure A.1: Microrobot motion configurations. The black arrow shows the magnetic field gradient, and thus, the direction of microrobot motion.

In configuration (e) the microrobot points upwards and therefore exhibits the smallest contact area with the retina. The magnetic gradient, generated by the OctoMag, is gradually increased from 0 to a maximum of $500\,\text{mT/m}$ and the translational movement of the microrobot is recorded and tracked by the camera. Experiments are repeated for each configuration at a constant magnetic field strength of 5, 10, and $15\,\text{mT}$. An additional gradient opposing the gravitational force (z-gradient) is applied between 0 and $50\,\text{mT/m}$. Subsequently, camera images are analysed using a customised vision toolbox in Matlab, resulting in the position and orientation information of the microrobot at each applied magnetic gradient and field in time.

configuration (c)	5 mT	10 mT	15 mT
Au-coated [mT/m]	420.8±113.4	241.7±53.4	187.5±45.6
Ppy-coated [mT/m]	245.8±53.5	159.2± 48.3	88.3±4.1

Table A.1: Experimental values (mean±standard deviation) for the *critical* gradient for Au- and Ppy-coated intraocular microrobots (configuration (c)) at constant magnetic field magnitudes 5, 10 and 15 mT.

A.3 Experimental Results

The representative graph in Fig. A.2(a) shows the translation of an intraocular microrobot due to an applied magnetic gradient for the configuration shown in Fig.A.1(c). It is observed that the microrobot translation is minimal until a *critical* magnetic gradient is reached. This gradient is representative for the strength of restrictive forces, such as friction, adhesion and drag, between the microrobot and the retina. Experimental values for the *critical* gradients are summarised in Table A.1 for different surface coatings as well as magnetic field magnitudes of a microrobot in configuration shown in Fig.A.1(c). The results are graphed in Fig. A.3 for gravity opposing z-gradients between 0 and 50 mT.

The *critical* gradients for gold and polypyrrole coated intraocular microrobots near the retina are illustrated in Fig. A.2(b). The data shown are for a microrobot that was moved perpendicularly to its orientation (Fig. A.1(c)).

## A.4 Discussion and Conclusion

The experiments show that an intraocular microrobot that is magnetically moved near the retina in an vitrectomised eye filled with a watery solution, first has to overcome a *critical* force, before starting to move. This force is due to friction between the microrobot and the retina, adhesion forces, and drag. The applied *critical* gradient decreases with increasing magnetic field strength. It is observed that the movement of an Ppy-coated intraocular microrobot is less restricted in vicinity to the retina than a Au-coated microrobot. Furthermore, results show that microrobot movement is least restricted for a rolling

microrobot, which is moved in configuration (c) and (d), defined in Fig. A.1. The largest net motion is observed when the microrobot's orientation is perpendicular to the applied magnetic gradient and, hence, its direction of motion. A possible reason for this behaviour could be the concave surface of the retina, that may restrict robot motion at certain orientations (Fig. A.1(a),A.1(b), and A.1(e)).

Concluding, most efficient microrobot motion in close proximity to the retina is observed for a polypyrrole coated microrobot, which is moved with a high magnetic field strength (here 15 mT) in a rolling configuration.
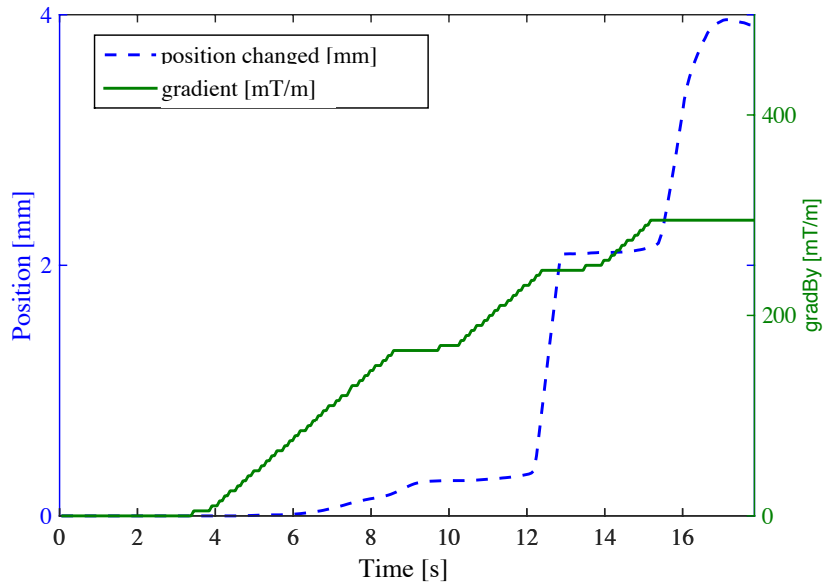
(a)
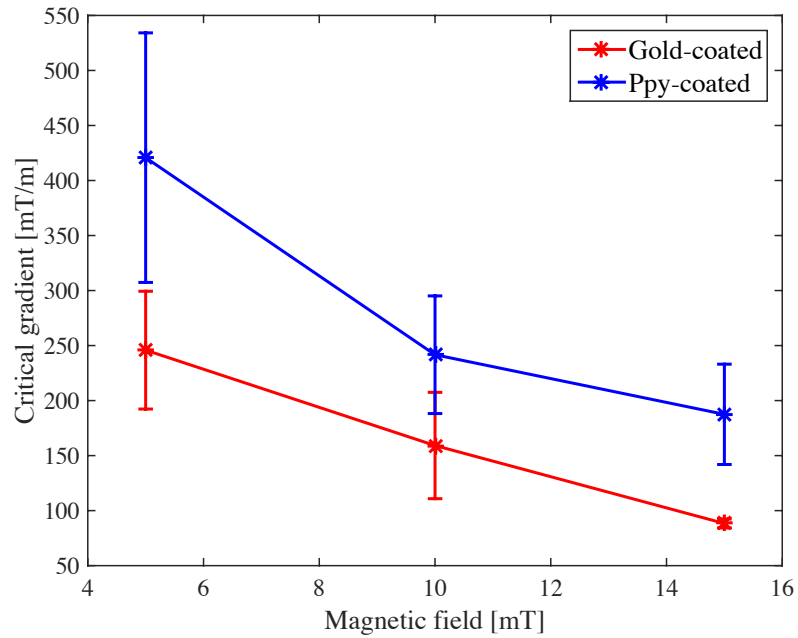
(b)

Figure A.2: (a) Translation of intraocular microrobot in close proximity to the retina resulting from an increased magnetic gradient. The *critical* gradient is 215 mT/m. (b) Comparison between the critical gradient of gold and polypyrrole coated intraocular microrobots.
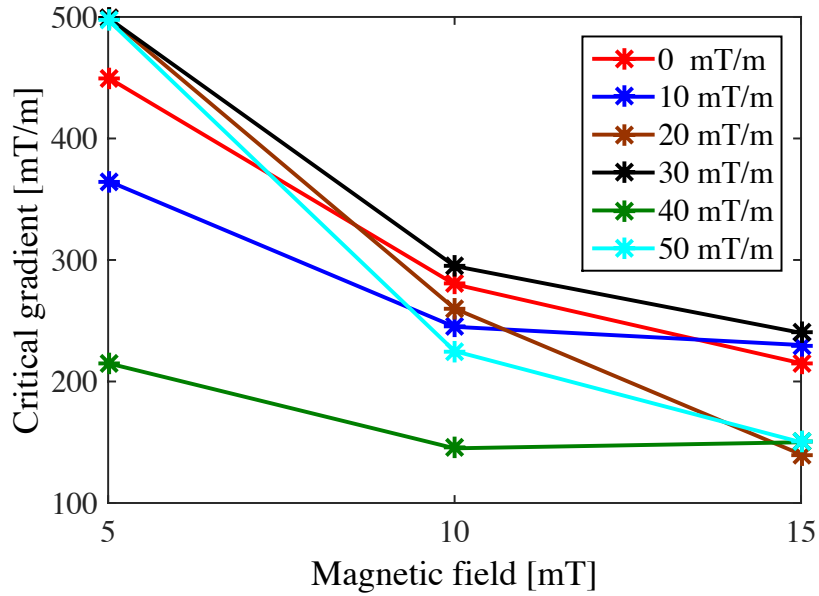
(a)
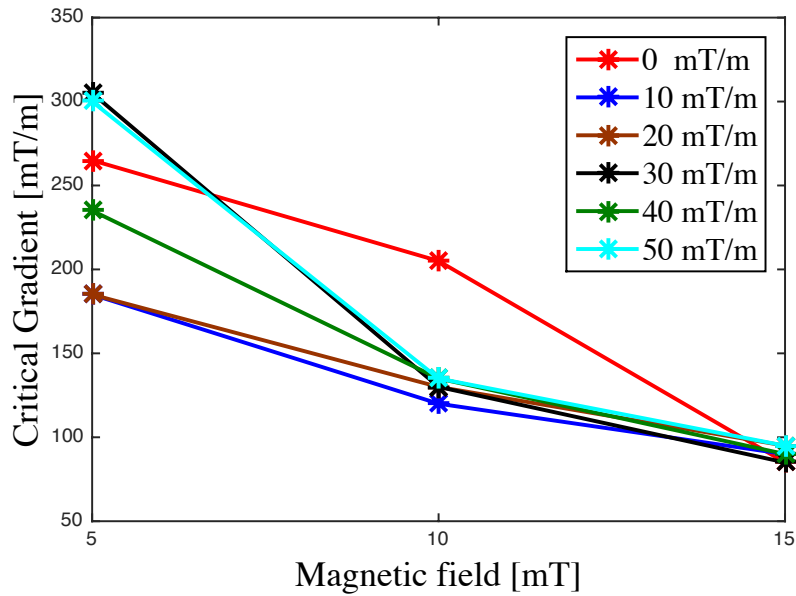
(b)

Figure A.3: Experimentally derived critical gradient for (a) Au- and (b) Ppy-coated intravitreal microrobots (configuration (c)) on porcine retina (*ex vivo*). Experiments are conducted with additional gravity opposing gradients between 0 and 50 mT.

Chapter B

Visual Derivation of a Safe Injection Point

The vision system of the assistive device for intravitreal injections, as described in Chapter 7, consists of two cameras. One camera observes the eye from the top (xy-plane), the other is located at the side of the eye and provides additional information in the yz-plane, as illustrated in Fig. B.1.
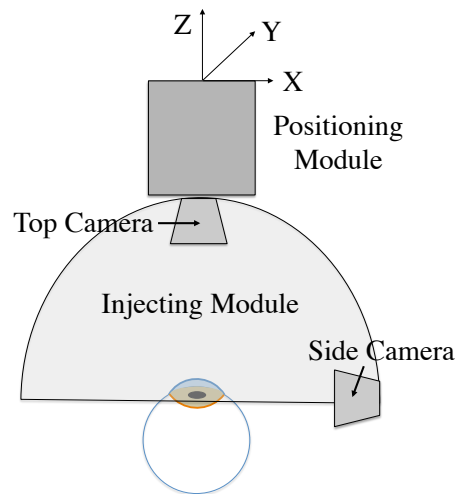
Figure B.1: A schematic view of the vision concept. The top camera observes the xy-plane, the side camera provides information on the yz-plane.

B.1   Eye Model Assumptions

To model the eye and its movements, several assumptions have been made.

- The eye is modelled as a perfect sphere with a diameter of 24 mm, the approximate size of an adult human eye [157].

- The eye is assumed to only rotate from the nasal to the temporal side, while rotations from top to bottom or are restricted.

- It is assumed that the eye always pivots around its geometrical centre, while translations are neglected.

- During fine positioning of the system, the patient is assumed to look straight up into the top camera.

- When selecting the injection point, the eye is assumed to look straight up into the top camera, so that the orientation of the eye is known.

- It is assumed that after fine positioning of the eye, it does not move into any direction, *i.e.* the relative position between the eye and the system is constant.

B.2   Eye Position and Orientation

Eye position and orientation can be derived independently with the above assumptions. During eye positioning, the patient looks straight up into the top camera. Using a pupil tracker, the position of the centroid of the pupil is derived from the top camera and the side camera images. Prior to experiments, the cameras have been calibrated and the pixel size is known.

After eye positioning, the location of the eye centre is known. When the eye is rotated (Fig. B.2), the position of the pupil centre changes and the direction of gaze (ζ) is calculated with

$$\sin(\zeta) = \frac{\Delta x}{r_{eye}} \tag{B.1}$$

where ζ is the angle that the eye rotates around the y-axis, Δx is the position difference of the tracked pupil centre in pixels, and r_{eye} is the radius of the eye in pixels.
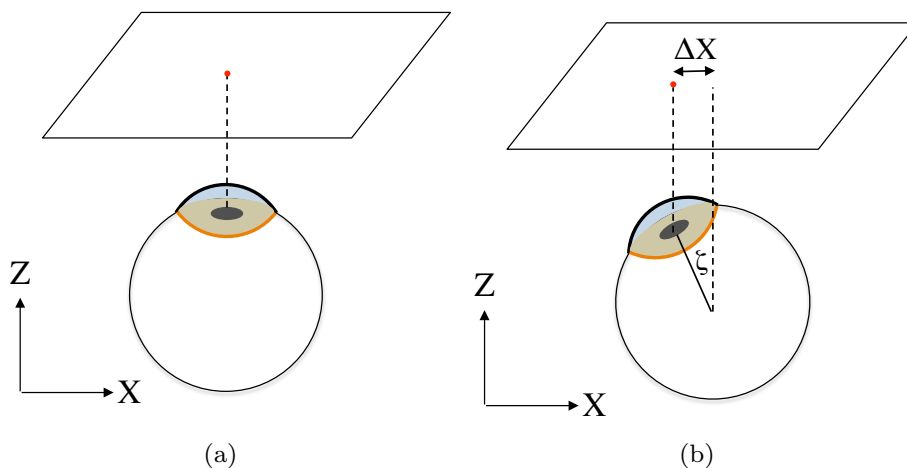
Figure B.2: Schematic of eye rotation and the projected image as observed with the top camera. (a) Eye looking straight up. (b) Eye is rotated around the y-axis.

B.3   Derivation of the Region for Safe Injection

Before injection, the human operator can select an injection point. The system calculates the safe region for injection and shows the top camera image with the overlaid region for safe injection, as illustrated in Fig. B.3(a). The safe injection region lays between $3.5\,\text{mm}$ and $4\,\text{mm}$ from the limbus and within an angle of $\pm 80°$ on the temporal side of the eye (see Section 7.2.3).

To display the safe region on the image, it is calculated using the eye model assumptions. The position of the safe region for injection is found to lie between x_{min} and x_{max}, derived by

$$\cos(\gamma_{min}) = 1 - \frac{(r_{iris} + d_{safe,min})^2}{2 \cdot \sin(\gamma)} \tag{B.2}$$

$$\cos(\gamma_{max}) = 1 - \frac{(r_{iris} + d_{safe,max})^2}{2 \cdot \sin(\gamma)} \tag{B.3}$$

$$x_{min} = r_{eye} \cdot \sin(\gamma_{min}) \tag{B.4}$$

$$x_{max} = r_{eye} \cdot \sin(\gamma_{max}) \tag{B.5}$$

(a)   (b)
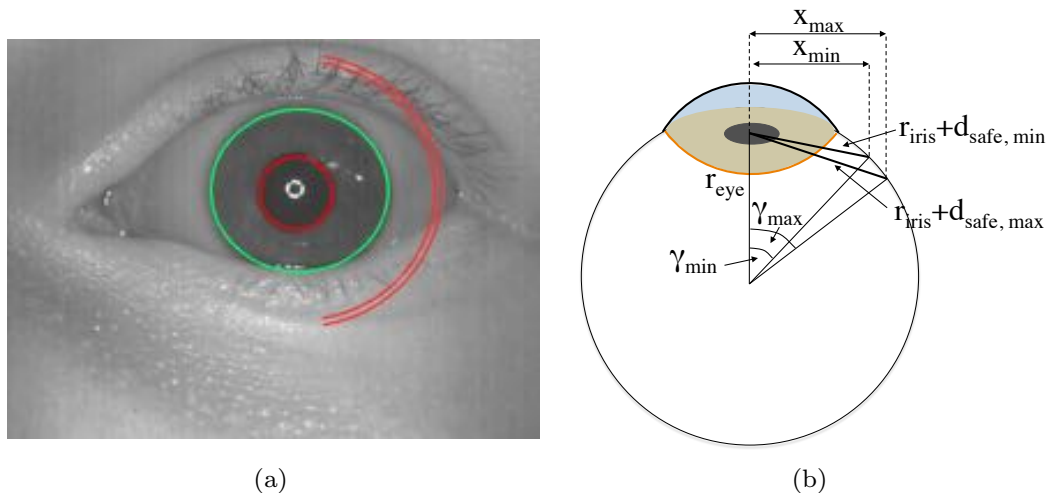
Figure B.3: (a) Calculation of safe injection region. (b) Injection region overlaid on top camera image with detected pupil and iris.

where $d_{safe,min} = 3.5\,\text{mm}$ and $d_{safe,max} = 4\,\text{mm}$, and r_{iris} and r_{eye} are the radii of the iris and the eye, respectively, as shown in Fig. B.3(b). Subsequently, two concentric semi-circles with radii x_{min} and x_{max} are displayed on the top camera image (Fig. B.3(a)). A human operator can thus select an injection point within the safe region for injection. If a injection point is selected, that lies outside of this region, the algorithm automatically shifts the point to lie within the region.

B.4   Injection Point Coordinates

After the injection point has been selected, the algorithm updates the coordinates of the injection point as the eye orientation changes. This is done by tracking the centroid of the pupil and keeping the angle between the direction of gaze and the injection point (β) constant as described in

$$\sin(\beta) = \frac{x}{r_{eye}} = const \tag{B.6}$$

where x is the x-coordinate of the injection point projection on the xy-plane. Thus, the coordinates of the injection point $(x_{inj}, y_{inj}, z_{inj})$ are updated as

$$x_{inj} = r_{eye}\sin(\beta - \zeta) \tag{B.7}$$

$$y_{inj} = const \tag{B.8}$$

$$z_{inj} = r_{eye}\cos(\beta - \zeta) \tag{B.9}$$

where ζ is the eye rotation angle (direction of gaze), as illustrated in Fig. B.2.

Chapter C

Magnetically Actuated and Guided Miniature Gripper

This thesis demonstrates several wireless and tethered robotic systems for ophthalmic applications. All of the presented magnetically steered systems have end-effectors with no moving parts due to size constraints. This chapter outlines the development of a modular miniature gripper for medical applications, which was presented in [158]. Kanika Dheman and Simone Schürle collaborated in this work. The design employs a permanent magnet for two purposes. It enables the actuation of the gripper and is simultaneously used to steer the device in an externally applied magnetic field. The modular miniature gripper can be moved without direct contact allowing for high mobility, or it can be attached to the distal tip of a catheter, which can then be magnetically steered by an electromagnetic manipulation system. In future, the actuation method may be scaled down to be used in ophthalmic applications.

C.1 Miniature Grippers for Medical Applications

Recent advances in endoscope technology, precise steering of catheters, and miniaturisation of flexible surgical tools promise to convert many procedures into minimally invasive endoscopic ones. The development of miniaturised and flexible tools and manipulators, such as milli- and micro-grippers, is of great importance to perform biopsies and manipulation of tissue with minimum damage to tissue [159]. Several tethered milli- and micro-grippers have been developed utilising different actuations systems, such as pneumatic [160], piezoelectric [161] and actuation based on shape memory effects [162–164]. Microelectromechanical system (MEMS) based micro grippers have been devel-
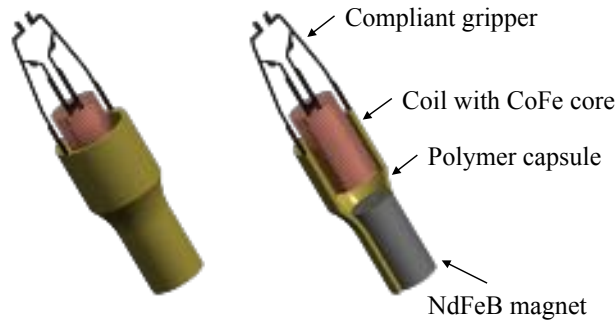
Figure C.1: The milli-gripper consists of a compliant gripper attached to a coil with a CoFe core in close proximity to a NdFeB magnet, all integrated in a polymer capsule. By applying a current to the coil, the attractive magnetic force causes the gripper jaws to close.

oped for single-cell handling and manipulation of particles smaller than $100\,\mu m$ [165–167].

Wireless capsule endoscopy was first clinically introduced in 2000 by Iddan et al. [168] and approved by the Food and Drug Administration (FDA) one year later. It describes a procedure in which a capsule with an integrated camera is passively moved through the gastrointestinal tract searching for obscure or occult bleeding. Currently, these capsular devices do not offer therapeutic capabilities and discovered lesions must be further investigated and intervened upon with conventional surgical methods [169]. Navigation of the capsules is passively controlled by peristalsis and gravity, and surgeons are incapable of stopping the capsule or turning it around. In order to eliminate these shortcomings, researchers have developed capsules with integrated biopsy devices [170–172]. Furthermore, magnetic steering with externally produced magnetic fields allows for control of capsules inside the body. Carpi et al. [173] integrated a magnet into a conventional video capsule and moved it utilising a magnetic navigation system. Yim et al. [174, 175] designed a soft capsule endoscope that can roll on the stomach surface and is steered by an external permanent magnet.

C.2   Gripper Design

The proposed system, illustrated in Fig. C.1, consists of a compliant gripper, an electromagnetic coil with a soft-magnetic cobalt iron (CoFe) core and a neodymium iron boron (NdFeB) magnet, which are all integrated into a polymer capsule. The gripper is fabricated from Nitinol, a metal alloy of nickel (Ni) and titanium (Ti) that exhibits large elasticity, and is highly biocompatible. Thus, it is suitable for medical applications. The coil is rigidly attached to the compliant gripper and in close proximity to the permanent magnet. When a current is passed through the coil, the magnetic interaction between the coil and the permanent magnet produces an attractive force between the coil and magnet, which actuates the gripper jaws. Additionally, the permanent magnet allows for controlled motion of the entire device in an externally applied magnetic field in either a contactless or tethered configuration.

C.2.1   Kinematics Design

For modelling simplicity, the forward kinematics of the compliant gripper are derived by applying a four bar linkage model [176] as illustrated in Fig. C.2(a). The objective is to establish the cumulative effect of multiple hinges on the resulting motion of the gripper jaws. This analysis assumes perfect rigidity of each link and free rotation of every joint around a single degree of freedom. The Denavit-Hartenberg convention is applied for kinematics modelling and the homogeneous transformation matrix for the effector bar is

$$
\begin{pmatrix}
c(\alpha_1) & -s(\alpha_1) & 0 & l_1 c(\theta_1) + l_2 c(\alpha_2) + l_3 s(\alpha_1) \\
s(\alpha_1) & c(\alpha_1) & 0 & l_1 s(\theta_1) + l_2 s(\alpha_2) + l_3 c(\alpha_1) \\
0 & 0 & 1 & 0 \\
0 & 0 & 0 & 1
\end{pmatrix}
$$

where $\alpha_1 = \theta_1 - \theta_2 - \theta_3$ and $\alpha_2 = \theta_1 - \theta_2$. Applying the geometric simplification

$$
\theta_3 = \frac{\pi}{2} + \theta_1 - \theta_2, \tag{C.1}
$$
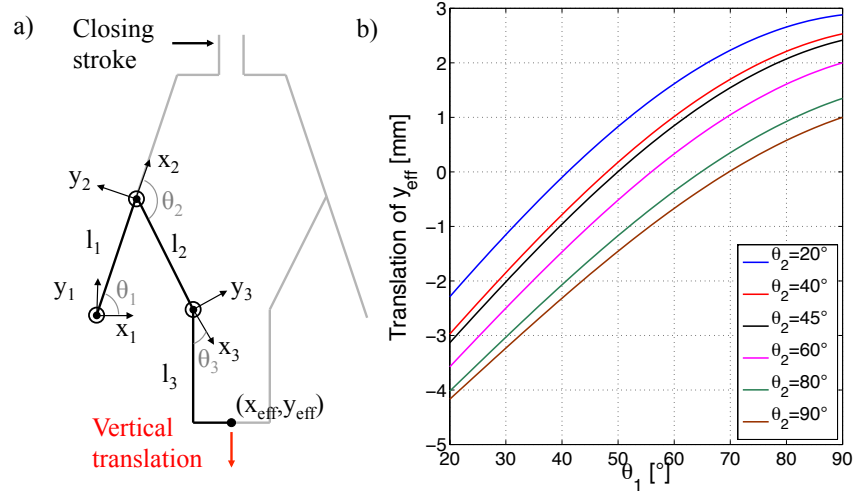
Figure C.2: a) Kinematics analysis of gripper model using Denavit-Hartenberg convention. b) Relation between angles θ_1, θ_2 and the vertical displacement of the effector bar y_{eff}.

the vertical translation of the effector bar becomes

$$y_{eff} = l_1 \sin(\theta_1) + l_2 \sin(\theta_1 - \theta_2) - l_3. \tag{C.2}$$

Figure C.2(b) shows the vertical translation of the effector bar y_{eff} in relation to various magnitudes of angles θ_1 and θ_2 for l_1 =5 mm, l_2 =2 mm and l_3 =4 mm. It is observed that, for all θ_2, decreasing θ_1 increases the vertical downward motion of the effector bar and, therefore, the gripping stroke. Analysis shows that for large θ_1, *i.e.* a vertical link l_1, the system becomes stiff and the displacement of the effector bar becomes small. Therefore, a small θ_1 and large θ_2 are desirable to increase the motion range of the gripper. However, by decreasing angle θ_1, the width of the gripper increases. The graph helps to find the optimal value for parameters θ_1 and θ_2 to maximise the translational displacement of the effector bar. These values are used as initial design parameters for finite element modelling (FEM).
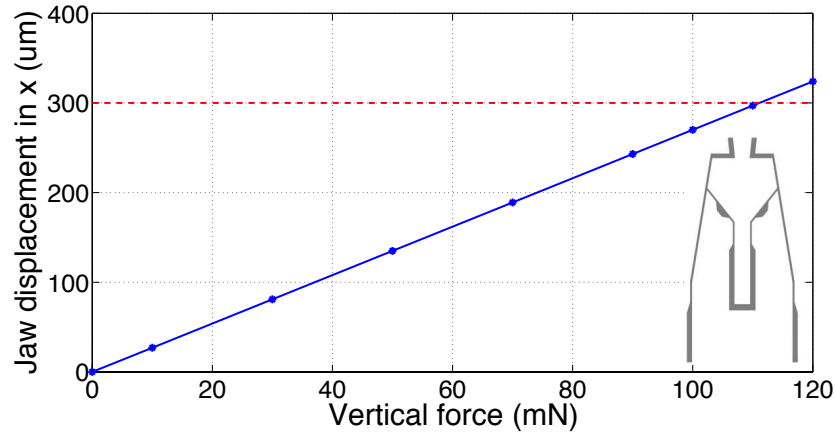
Figure C.3: FEM results for displacement of a single gripper jaw in relation to a vertically applied force. The gripper jaws fully close at 111 mN.

C.2.2   FEM Simulation

A model of the gripper was developed using computer aided design (CAD) software (NX 7.5, Siemens PLM) and parameters are tuned with FEM to derive the best gripping response utilising the Nastran solver for simulation, which predicts mechanical effects on a system in response to the applied input force. The model is meshed with three dimensional tetrahedral meshing elements with element size of 0.1 mm. The material chosen for simulation is Nitinol with mass density 6.54 g/mm^3, elastic modulus 83 GPa and Poisson's ratio 0.33. Although the elastic modulus of Nitinol changes with stress, the highest value for the martensite form of the alloy was used for simulations to provide a worst-case scenario. Fixed constraints are introduced at the legs and a vertical force between 0 and 120 mN is applied to the effector bar. Figure C.3 shows the resulting jaw displacements for various input forces. FEM simulations suggest that the gripper closes, *i.e.* both jaws have undergone a horizontal displacement of 300 μm, with a vertically applied force of 111 mN. Results for a vertical input force of 111 mN is illustrated in Fig. C.4. The simulation results show that a displacement of 300 μm in x-direction is expected for each jaw for the given input force, as illustrated in Fig. C.4(a). The effector bar displacement

(Fig. C.4(b) for the same input is 136 µm. Figure C.4(c) illustrates the magnitude of total displacement [mm] of the gripper structure. The maximum Von Mises stress of 128.28 MPa is much smaller than the yield strength of Nitinol (>1100 MPa) and is found at the inner hinge of the gripper, shown in Fig. C.4(d).

C.2.3 Gripper Fabrication

The two dimensional gripper structure is fabricated with a monolithic laser ablation process conducive to the choice of material. A piezoelectric positioning stage (SmarAct, Germany) with three degrees of freedom supports and positions a Nitinol sheet for micro-machining. The gripper was manufactured using a DUETTO picosecond micromachining green laser (Time-Bandwidth, Switzerland) with 532 nm wavelength and 100% power at a frequency of 300 kHz. Higher frequencies enable higher scan speed while lowering the energy per pulse, hence, reducing heating effects. The beam width of the laser was measured as 33 µm, which is sufficient to fabricate the gripper with minimum feature size of 100 µm. Figure C.5(a) shows the fully fabricated gripper with thickness of 254 µm. The gripper jaws are 920 µm apart and are oriented at 6.92° in the open configuration so they align when the gripper is closed. Figure C.5(b) shows two different gripper designs during the laser ablation process with the green laser.

C.2.4 System Assembly

A capsule with largest diameter 8.5 mm, smallest diameter 5 mm, and length 18.5 mm is 3D printed (Objet500, Stratasys, Eden Prairie, MN, USA). A permanent NdFeB magnet with diameter 4 mm and length 8 mm is attached to one end of the capsule, and the gripper feet are attached to the other end. A coil with diameter 4 mm and length 7 mm is wound with copper wire with diameter 150 µm around a CoFe core of dimensions $1.0 \times 1.3 \times 7.0$ mm. The effector bar of the Nitinol gripper is attached to the coil, such that the coil is without contact to the polymer capsule, as shown in Fig. C.1.
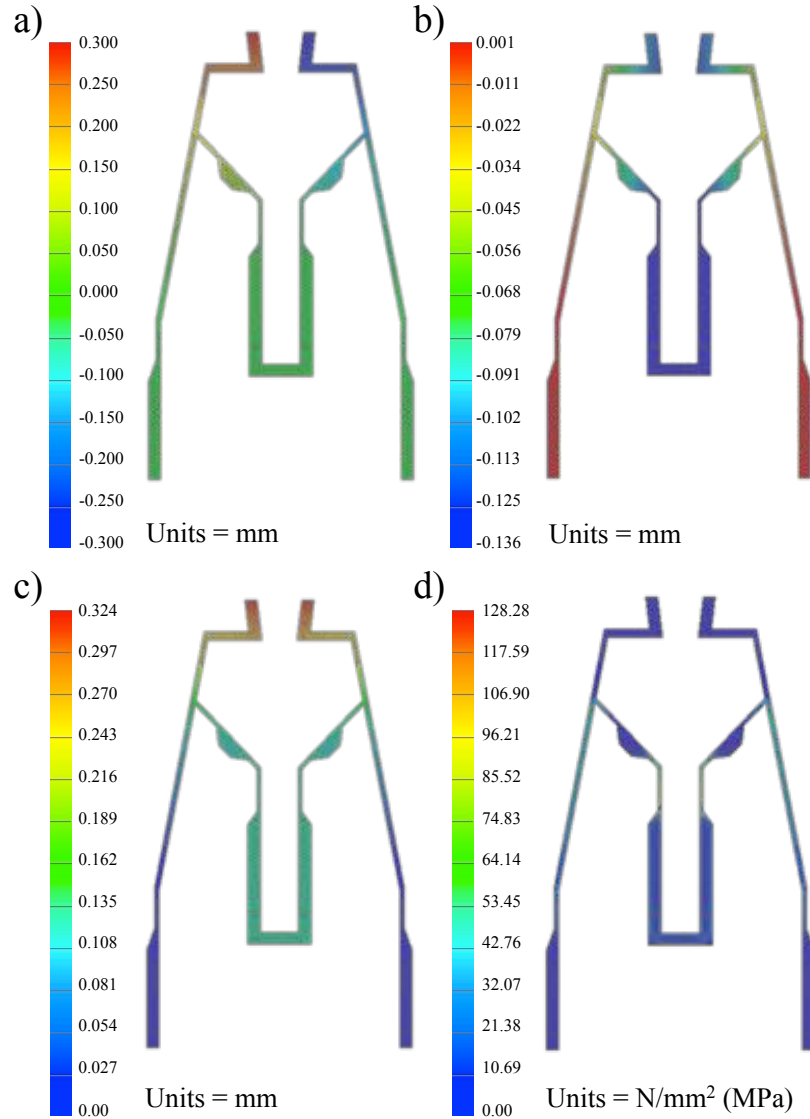
Figure C.4: FEM simulation of Nitinol gripper with fixed constraints on legs and vertical force of 111 mN acting on effector bar. a) Displacement in x (max. value 300 μm), b) Displacement in y (max. value 136 μm), c) Magnitude of displacement (max. value 324 μm), d) Von Mises stress (max. value 128.28 MPa)

C.3   Experimental Validation

C.3.1   Methods

To characterise the gripper, the relationship between translation of the effector bar and the gripping stroke is quantised. A thin needle is attached to

191
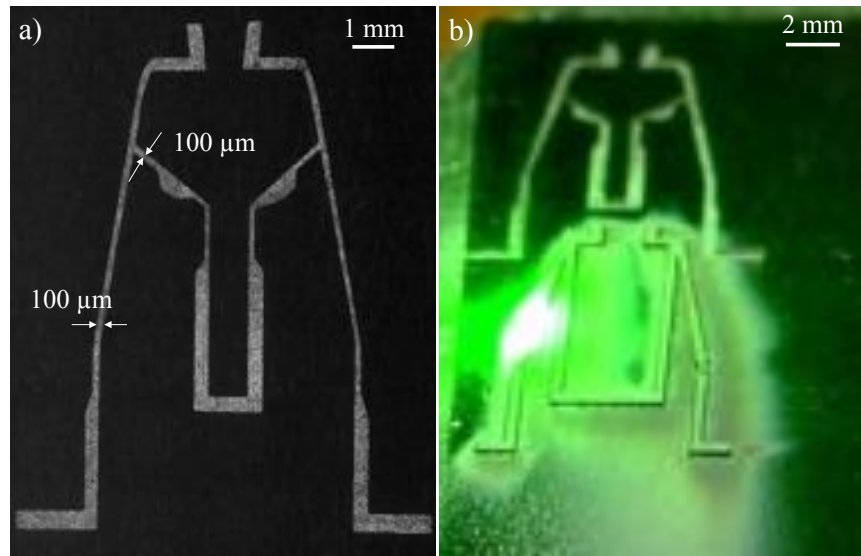
Figure C.5: a) Fully fabricated Nitinol gripper with thickness $254\,\mu$m and smallest feature size of $100\,\mu$m. b) Fabrication process of two different gripper designs with a picosecond micro machining green laser.

a piezoelectric micropositioner (Smaract, Germany) that pulls on the effector bar. The needle is moved in steps of $50\,\mu$m and the tip closure is observed through a digital microscope (DNT, Germany) and post-processed in MAT-LAB. The gripping performance of the milli-gripper to manipulate biological tissue is analysed. A sample of porcine liver tissue is prepared and moved towards the gripper jaws. When the gripper jaws touch the liver sample, the gripper is actuated to grasp a small sample of the tissue, as illustrated in Fig. C.8. The liver sample is then slowly moved away, while the gripper jaws remain closed. To characterise the fully assembled gripping system the gripper is attached to the electromagnetic coil and placed in close proximity to the permanent magnet, all integrated in a polymer capsule. By applying current to the coil, the magnetic attractive force between coil and permanent magnet causes the gripper to close. Currents between 0 and $90\,$mA are applied to the coil.
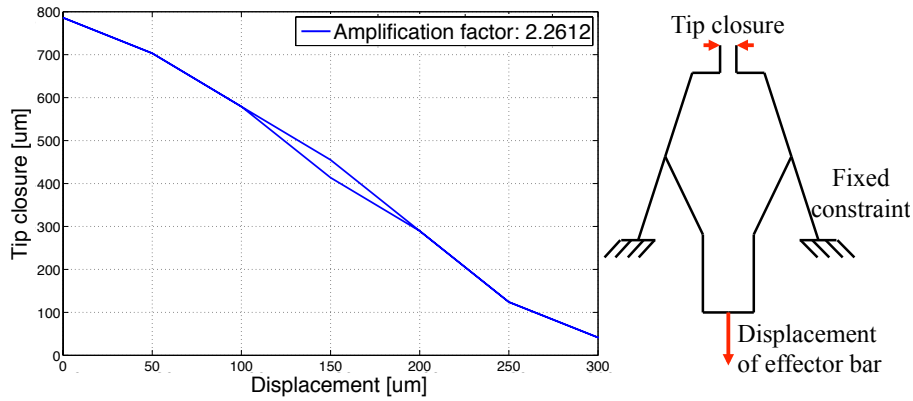
Figure C.6: Closing hysteresis of gripper jaws at $50\,\mu\text{m}$ steps with average amplification factor between effector bar displacement and tip closure of 2.26.
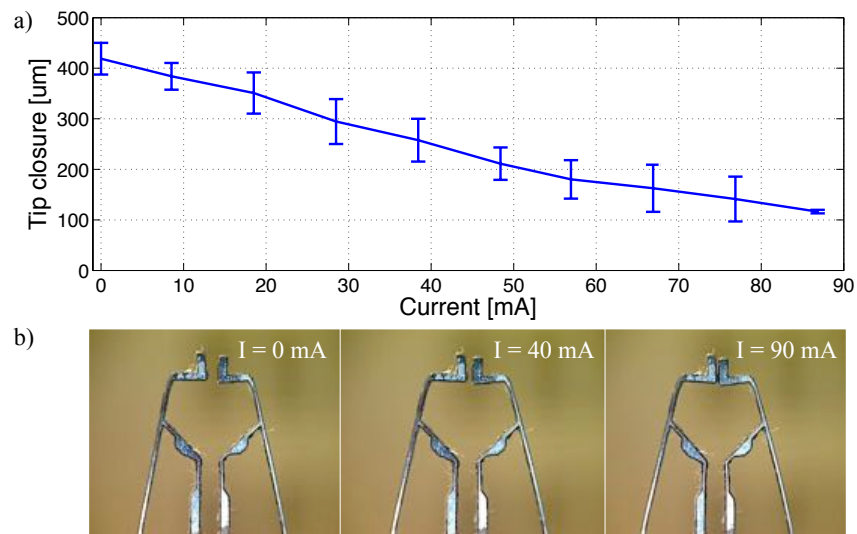

Figure C.7: a) Closing stroke of gripper jaws in $[\mu\text{m}]$ as a function of current $[\text{mA}]$ applied to the coil. The gripper closes at an average rate of $3.6\,\mu\text{m}/\text{mA}$. b) Closing gripper jaws for changing current in the actuation coil for currents of $I = 0$, 40 and $90\,\text{mA}$.

C.3.2   Results

Figure C.6 illustrates the resulting tip closing behaviour when the effector bar is displaced with $50\,\mu\text{m}$ steps up to a maximum displacement of $300\,\mu\text{m}$. The
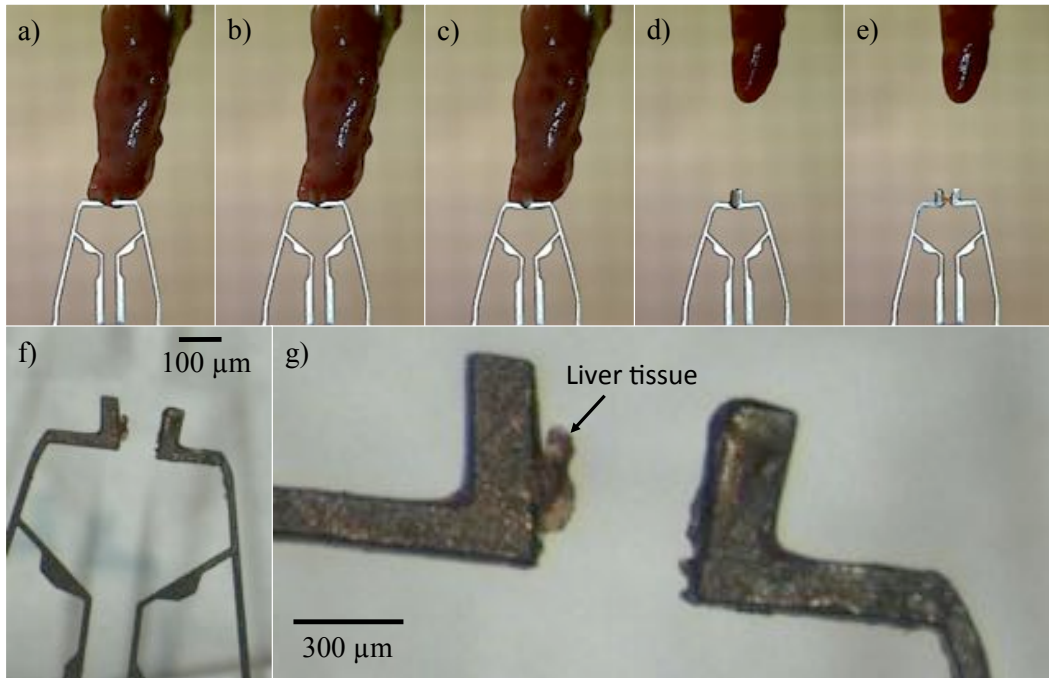
Figure C.8: a-e) Actuation of gripper in porcine liver. f) The gripper jaws after actuation with liver tissue. g) Microscope image of gripper after actuation with liver tissue visible.

graph shows a slight hysteresis for opening and closing of the tip. The average amplification factor is 2.26, determined as the ratio between the input displacement of the effector bar and the output tip closure. Figure C.8(g) shows a microscopic image of the milli-gripper after grasping the porcine liver. The image demonstrates that a small amount of tissue was grasped. Thus, the milli-gripper could potentially be used for biopsies or harvesting of small samples of biological tissue. Figure C.7(a) shows the relationship between a current applied to the coil and the gripper closing stroke with power of 550 mW. An average closing relation of 3.6 µm/mA is observed. The gripper jaws are fully closed when a current of 90 mA is passed through the electromagnet. Figure C.7(b) shows the gripper jaws when currents of 0, 40 and 90 mA are applied to the coil.
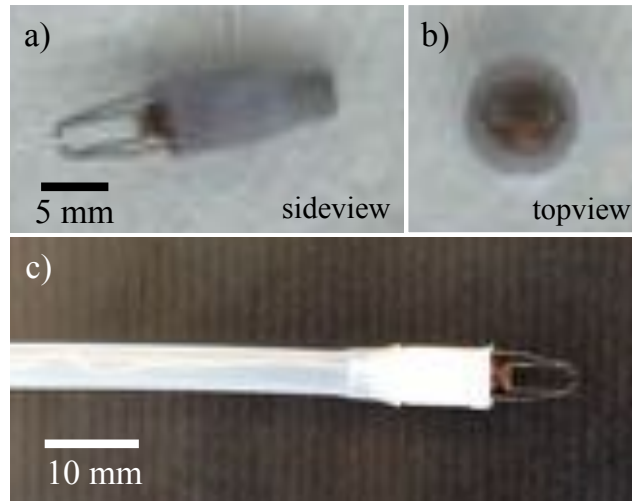
Figure C.9: The modular device with integrated gripper in a) sideview and b) topview. It is moved in an externally applied magnetic field. c) The device can be attached to the distal tip of a flexible catheter (diameter 5 mm) for tethered magnetic manipulation.

C.4   Magnetic Manipulation of the Milli-Gripper

Figure C.9 shows the assembled device with integrated gripper and NdFeB magnet from the side (a) and the top (b). The milli-gripper is moved in an external magnetic field. First, it is immersed in silicone oil with viscosity of $5000\,\mathrm{mPa\cdot s}$ (Silitech AG, Gümligen, Switzerland) and placed inside the workspace of an electromagnetic manipulation system. The workspace is observed with a CCD camera (Point Grey, Richmond, Canada) with frame rate 15 Hz. A customised computer vision algorithm tracks the two dimensional position of the device utilising a simple blob tracker. The visual information is used as sensor feedback by a proportional-derivative controller that controls the device along a predefined trajectory. Figure C.10 shows the milli-gripper following a predefined square trajectory with side length of 25 mm. The applied field has a magnitude of 15 mT and is oriented along the normal of the xy-plane causing the device to stand upright.
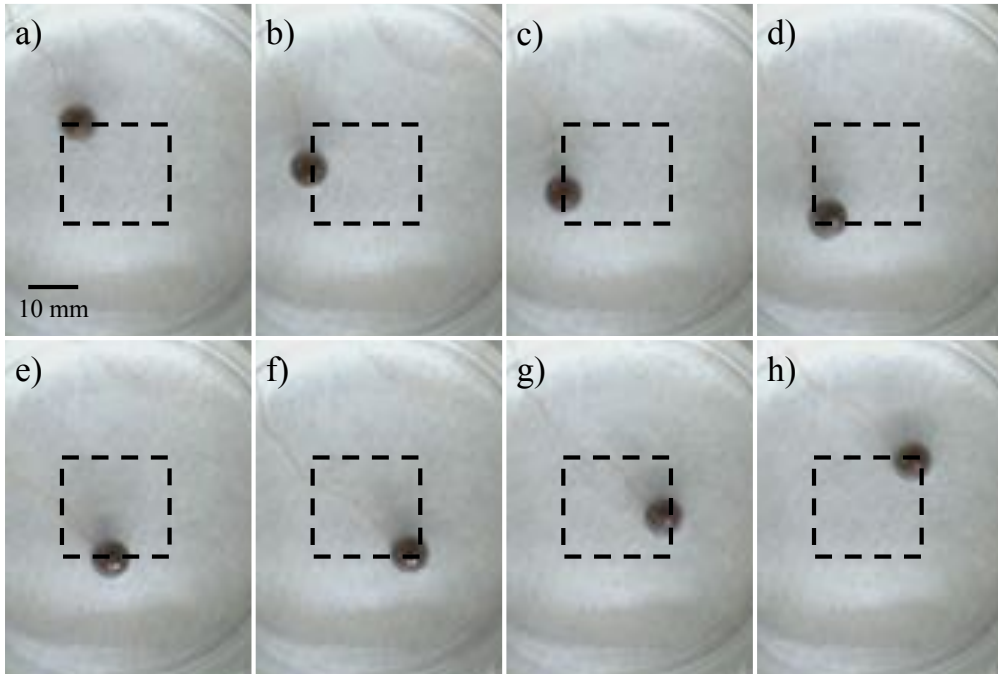
Figure C.10: The milli-gripper is steered magnetically along a predefined square (side length 25 mm) path with an externally applied magnetic field with magnitude 15 mT.

C.5   Manipulation of a Milli-Gripper tipped Catheter

The modular milli-gripper is connected to a flexible silicone catheter with inner and outer diameter of 4 and 5 mm, respectively. The tethered device is shown in Fig. C.9(c). By applying external magnetic fields the device can be manipulated magnetically. A two dimensional maze with several bifurcations was built from plexiglas and placed in the workspace of the electromagnetic actuation system. The longitudinal motion of the catheter is governed manually while the lateral motion of the catheter is controlled by the electromagnetic manipulation system. The externally applied field, generated by the electromagnetic manipulation system, has a magnitude of 40 mT. When the magnetic field orientation is changed, the NdFeB magnet at the distal tip of the catheter aligns with it, and, thus, the catheter tip orientation is controlled. The workspace is observed with a CCD camera (Basler AG, Ahrensburg, Germany) with frame
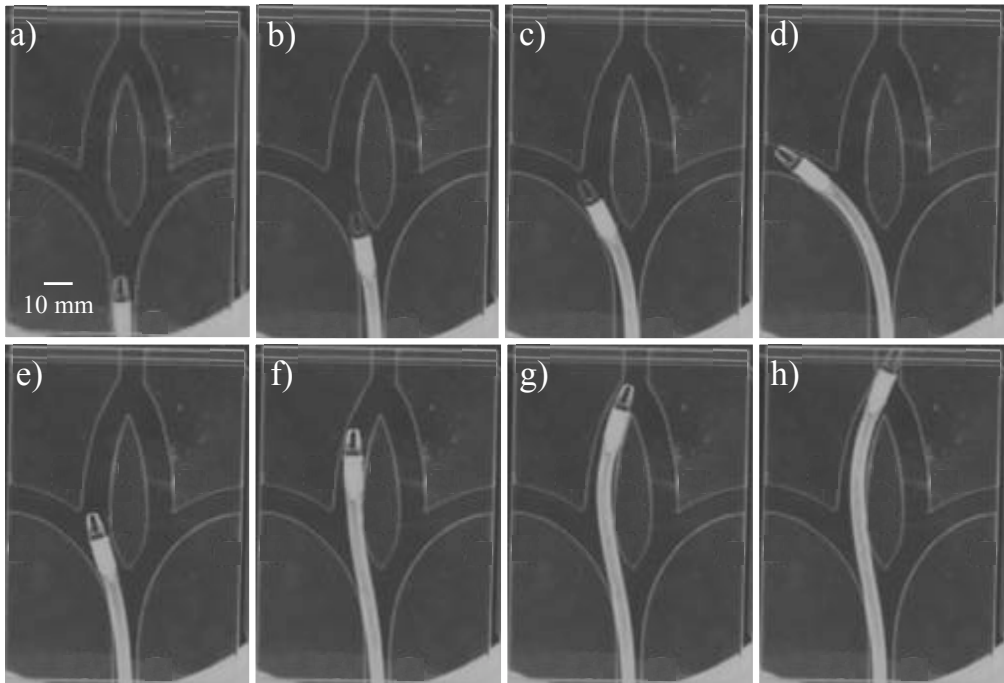
Figure C.11: The tethered device with integrated gripper is successfully steered through a maze by an externally applied magnetic field with magnitude 40 mT.

rate of 30 Hz. The images are transferred to the computer and allow the user to steer the catheter open loop with a three dimensional joystick. Figure C.11 shows magnetic catheter steering in the electromagnetic manipulation system. The gripper capsule on a catheter is successfully steered through the two dimensional maze. Images a-d show motion into the left channel of a bifurcation, followed by a retraction of the device and subsequent motion along the right channel in images e-h.

C.6   Discussion and Conclusion

The milli-gripper is designed to fit into a capsule with maximum diameter of 8 mm while offering a stroke of 600 μm. The gripper kinematics are tuned to allow for the largest stroke while restricting the gripper width to the maximum diameter of the capsule. The design of the compliant gripper makes full use

of the elasticity of the material through the optimization of the flexure hinges where the entire structure adds to the gripper's compliance. The choice of material (Nitinol) is suitable for medical applications due to its high flexibility and biocompatibility. The gripper design does not exhibit sharp edges or corners that might injure tissue. It can be fabricated with a monolithic laser ablation process, a quick process allowing for high throughput. Experimental validation shows a linear trend for closing the gripper jaws with displacement and current input. The standard deviation of measurements ranges between 3.5 μm and 46.6 μm. When actuating the gripper by displacing the effector bar, a slight motion hysteresis is observed which is presumably due to relaxation of the material. The gripping stroke can be varied with input current and exhibits a maximum of 300 μm for each jaw.

An advantage of this milli-gripper design is the integration of a permanent magnet that allows for steering the device in an externally applied magnetic field. The modularity of the system allows for both tethered and contactless manipulation of the gripper. The advantages of a minimally tethered device include the high agility of motion. Guided by external magnetic fields, the gripping device can be maneuvered inside narrow spaces and through bifurcations or around corners. After attaching the milli-gripper to a flexible silicone catheter, the gripper becomes a tethered device. Advantages of a tethered system include the possible integration of more tools, such as irrigation or aspiration tubes, light and a camera. A tethered device can also exert higher forces on tissue in longitudinal direction of the catheter. The tethered system is easily removable by pulling the catheter while an contactless system has to be steered magnetically out of an opening. The magnetization of the device is calculated as 93.6 mNm/T and gives a measure for the torque per unit of the applied magnetic field and the force per unit of the field gradient. Therefore, the maximum torque and force that can be applied to the milli-gripper in an external magnetic field with magnitude 100 mT and magnetic gradient of 500 mT/m are derived as 9.36 mNm and 46.8 mN, respectively.